EDMS # 459195

Markus Brugger

The Radiological Situation in the Beam-Cleaning Sections of the CERN Large Hadron Collider (LHC)

DISSERTATION

zur Erlangung des akademischen Grades eines
Doktors der Technischen Wissenschaften

eingereicht an der
Technischen Universität Graz
Rechbauerstraße 12
A - 8010 Graz

Begutachter: Ao.Univ.-Prof. Dr.techn. Ewald Schachinger

Institut fur Theoretische Physik der TU Graz

Graz, November 2003

CERN-THESIS-2003-039
//2003

Kurzfassung

Diese Dissertation beschäftigt sich mit radiologischen Aspekten am "Large Hadron Collider", welcher momentan am CERN gebaut wird. Im Detail handelt es sich dabei um die beiden so genannten "Beam Cleaning Insertions", jene Bereiche in welchen man versucht möglichst alle Teilchen zu absorbieren, welche ansonsten in anderen Teilen des Beschleunigers zu Schäden führen könnten. Es werden zwei kritische Aspekte des Strahlenschutzes behandelt: Dosisleistung durch induzierte Radioaktivität und die Aktivierung von Luft. Die Anpassung des Designs dieser Regionen in Verbindung mit einer detaillierten Abschätzung der jeweiligen Dosisleistungen ist von großer Wichtigkeit für spätere Wartungsarbeiten. Bisher standen lediglich sehr eingeschränkte Studien über die in jenen Regionen zu erwartenden Strahlenniveaus zur Verfügung, welche diese Dissertation nun zu erweitern und vervollständigen sucht. Dabei wird eine neue Methode angewendet um Dosisleistungen zu bestimmen, welche, da sie zum ersten Mal zu deren Berechnung verwendet wird, sorgfältig im Rahmen eines Experimentes überprüft wird. Zusätzlich stellt die Aktivierung der Luft einen wichtigen Aspekt für die Inbetriebnahme des Beschleunigers dar. Jüngste Änderungen im Konzept des Beschleunigers, machen eine Revision vorhandener Ergebnisse und eine umfassende neue Studie notwendig. Die Ergebnisse von beiden Studien sind von großer Wichtigkeit für die weiteren Entscheidungen bezüglich des endgültigen Entwurfs der "Beam Cleaning Insertions".

Abstract

This thesis contributes to radiological assessments of the design and operation of the Large Hadron Collider currently under construction at CERN. In particular, the scope of this thesis is to examine the beam cleaning insertions - two of the main loss regions of the LHC where beam particles which would otherwise cause unwanted losses at different places of the machine are purposely intercepted. Two critical issues with regard to the protection of personnel and environment are studied: remanent dose rates due to induced radioactivity and airborne radioactivity. Although a detailed estimate of remanent dose rates is important for an optimization of later maintenance interventions only very limited information on remanent dose rates to be expected around the collimators was available so far. This thesis is an attempt to extend the knowledge considerably, especially by applying a new calculational method. Since this new approach is used for the first time in the design of the LHC a careful benchmarking with experimental data is performed as part of this work. In addition, a revision of existing assessments of airborne radioactivity became necessary after various design changes of the collimation system and due to modifications in the ventilation scheme of the LHC. Therefore, an extensive parametric study is presented covering all possible design scenarious. The results of both studies will give important input to the design of the collimators and the beam cleaning insertions.

Table of Contents

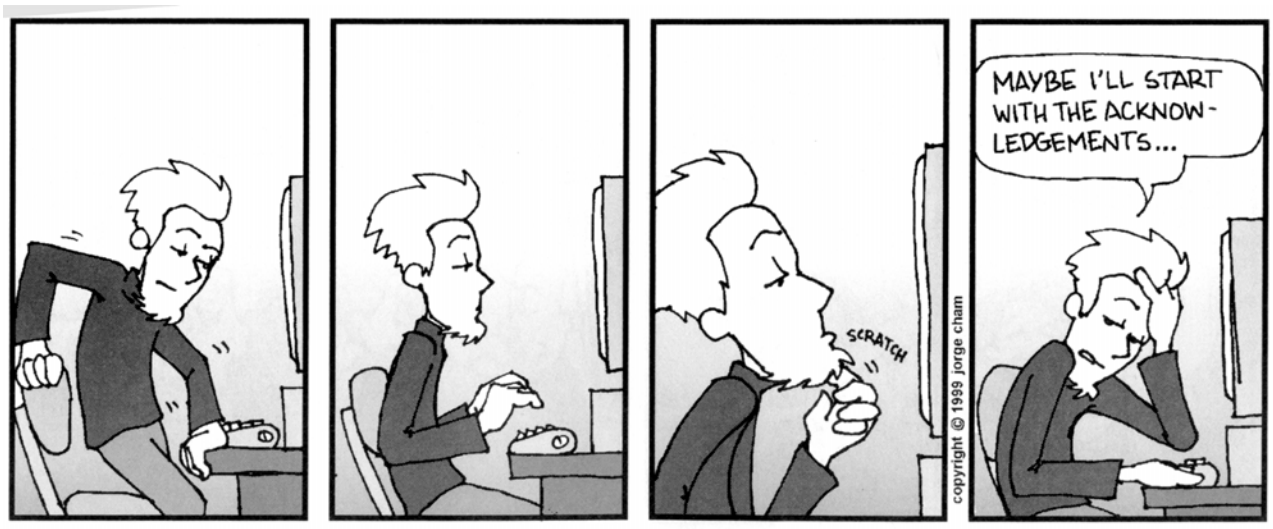
SCRATCH
MAYBE I'LL START WITH THE ACKNOW-LEDGEMENTS...
copyright © 1999 jorge cham

1 Introduction

Particle physics is the branch of physics exploring the innermost basic constituents of matter and their interactions. CERN, the European Laboratory for Particle Physics, was founded in 1954 in Geneva (Switzerland) as a joint European project to provide a major scientific facility for particle physicists. Today it is one of the world's largest laboratories, as well as an outstanding example of international collaboration with its 20 member states.
The challenge in modern particle physics research is to probe at higher and higher collision energies, because the basic constituents of matter can only be studied at those energies. Thereby, the accelerator itself can be understood as a microscope, with the energy of accelerated particles defining the wavelength used for the analysis and, as a consequence, the resolution of the apparatus. Thus, the higher the collision energy, the larger the spectrum of observable physical phenomena, and the smaller their scale.

In the past, numerous experiments were performed at different generations of accelerators, successfully expanding the knowledge in particle physics. Down to the de Broglie scale of 10^{-18} m, corresponding up to the several hundred GeV energy, nature seems to be described by the so-called Standard Model. This theoretical model describes matter as being built up of combinations of three families of fermions of different types (quarks, electrons, neutrinos). Their interaction are described by several forces mediated by bosons (photons, “weak” bosons, gluons). In spite of its remarkable success as a descriptive and predictive theory (with a precision of 10^{-3} or better), the Standard Model still shows several shortcomings.

As such the origin of the particle masses and their distribution, which spans more than twelve orders of magnitude, are neither predicted nor explained. A possible process to endow particles with masses is their coupling with a particular field permeating space, the so-called Higgs field, which would be mediated by the Higgs boson. Theoretical considerations and experimental searches for the Higgs boson indicate that its mass range would fall between 115 GeV and about 1 TeV.

However, the Standard Model including the Higgs mechanism may well not be the ultimate theory. The concept of Grand Unified Theories, which predict the unification of the strengths of electromagnetic, weak and strong interactions at very high-energy, would require to expand the Standard Model in order to include other particles (*e.g.,* “supersymmetric”) to the known ones. Although this unification would only occur at very high energies, some of its consequences could also appear as new physics in the TeV range.

Modern accelerators, in addition to their capability to discover possible new physics and scrutinise proposed models, will also permit precision

measurements that, *e.g.,* will either confirm the Standard Model or require its modification. Moreover, they will explore through dedicated experiments the origin of matter-antimatter asymmetry, as well as the deconfinement of quarks and gluons in a so-called “quarkgluon plasma”. Finally, by providing high resolution powers they may reveal totally unexpected physical phenomena.

One of the currently most advanced projects of particle physics in the TeV energy domain is the Large Hadron Collider (LHC). It is presently under construction at CERN through a global collaboration involving all regions of the world active in the field. Upon its completion in 2007, the LHC will accelerate and bring into collision intense beams of protons and ions at unprecedented energy and luminosity (14 TeV and 10^{34} $cm^{-2}s^{-1}$, respectively for protons). The collision products will be analysed in four large experiments located in underground caverns around the LHC machine.

An integral part of the design of a new accelerator is the protection of personnel and environment against prompt and remanent radiation. Sources of prompt radiation have to be well shielded so that the dose received by people working in accessible areas close to the machine is kept at the absolute minimum. In addition, radioactivity created in interactions of the beam particles with installations lead to remanent dose rates, thus affecting personnel during maintenance interventions. It is therefore required to optimize the design of the accelerator with respect to radiation protection, so that the doses to personnel during the operational phase of the accelerator is kept as low as reasonable achievable (ALARA).

The accelerator operation may also have direct impact on the environment through the creation of radioactive waste and the activation of rock, groundwater and air. For example, air will reach public areas through the installed ventilation system and strict radiation limits have to be obeyed.

Studies have to be performed from the start of the planning of an accelerator, evolving in precision with the design of the accelerator. Apart from the task to control the operation of an existing accelerator and to assure that radiological impacts remain within legal boundaries, an important mission of radioprotection is also to assure the optimization of the layout of the accelerator with respect to radiological issues. Modern Monte-Carlo codes are applied in order to calculate the relevant quantities and account for the specific design of the machine. This ensures a flexible adaptation of the simulations and fully includes radioprotection already in the design of an accelerator.

In general radiological quantities scale with the number of interacting particles. Therefore, regions with high loss rates, such as the physics experiments, the beam dumps or special dedicated loss regions are of particular concern for radioprotection. This work examines the two main loss regions of the LHC, the so-called collimation or beam cleaning regions, where accelerated beam particles purposely are intercepted which would otherwise cause unwanted losses at other places in the machine. For example, already a few per mille of the scattered particle flux interacting with a superconducting magnet would cause it to quench. Therefore, an efficient collimation system is required in order to ensure a stable operation of the accelerator, which is provided at the LHC by two cleaning insertions. It is estimated that about 30% of all stored LHC protons will be lost in the cleaning insertions, thus making them to one of the most activated sections at the LHC. It is therefore essential to study carefully the radiological impact and to consider provisions.

In this work two aspects critical with regard to the protection of personnel and environment are discussed: remanent dose rates due to induced radioactivity and airborne radioactivity. The former, being important during later repair or maintenance interventions must be considered as

accurately as possible already in the design phase. In case of high dose rates the access time will have to be severely limited and certain means of remote handling may become essential. In case of air activation accurate estimates are of particular importance as at the locations of both cleaning insertions air is released into the environment, moreover, at one of them into a densely populated area. For induced activities as well as air activation estimates existed only for old designs of the accelerator, hence recent fundamental changes of the layout made it necessary to review these studies.

Although many quantities essential in the design and operational phase of a high-energy accelerator (*e.g.,* dose to components and dose equivalent to personnel by prompt radiation) can be predicted with rather good accuracy using modern Monte-Carlo codes, still, estimates of specific activities and resulting residual dose rates - although equally important - are usually far less reliable. Methods used so far to estimate the remanent dose rate in the collimation region imply general shortcomings. For example, they provide a fairly good approximation of the dose rate in contact with a large object, but can lead to a significant overestimation when the activated object is rather small and cannot predict dose rates at arbitrary locations. Although these methods are considered to be conservative they are not always practical for the finalisation of a design of the cleaning insertions. Therefore, a new method to calculate remanent dose rates was used for the calculations presented in this work. This method is more rigorous and general and can be applied to arbitrary irradiation configurations and geometries. It is a two-step Monte-Carlo approach based on an explicit calculation of isotope production followed by the transport of photons, positrons, and electrons from the radioactive decay to the point of interest.

In order to evaluate this new method, a benchmark experiment was performed and results for remanent dose rates were compared to detailed simulations. The experiment included the evaluation of induced radioactivity produced in various materials, typically used at high-energy accelerators. The activation of accelerator components is an important radiation safety concern not only during the operation of the machine and possible maintenance but also later for de-commissioning and final disposal of the activated materials. In all cases accurate calculations of the radionuclide inventory and remanent dose rates are of utmost importance.

Several similar experiments have already been performed, however, most of these studies concentrate either on induced activity or on remanent dose rates although both are closely linked to each other. Due to the complexity of the involved physical processes and analysis methods it is often difficult to attribute disagreements between calculated and measured results to their respective source of uncertainty. Therefore, the study described in this thesis is an attempt to overcome some of the shortcomings of earlier studies by benchmarking at the same time Monte-Carlo predictions for isotope production and remanent dose rates with detailed measurements.

Finally, the completion of the collimation design and fundamental changes with respect to previous layouts required detailed studies of airborne radiation. In particular isotope production based on the design configurations were intercompared with each other, as well as with results of previous calculations.

The thesis is organized as follows.

Chapter 2 gives a short description of the LHC design. Due to its complexity, only those parts of the accelerator are sketched which are essential for the studies discussed in this thesis.

CHAPTER 1 Introduction

Since this work delivers a part to the required radiation safety studies for the LHC, the applicable safety regulations have to be incorporated into a discussion of results. Therefore, legal aspects most relevant to this work are summarized in Chapter 3.

At CERN, the FLUKA Monte Carlo code and its predecessors have been successfully used for decades in radiation protection studies. In fact, the code has its roots in this field and is thus the most appropriate choice for the studies presented in this thesis. Thus, Chapter 4 gives a short summary about the code with particular emphasis on models and techniques used in this study.

Chapter 5 describes the above mentioned attempt to overcome some of the shortcomings of earlier studies related to induced radioactivity by benchmarking at the same time FLUKA predictions for isotope production and remanent dose rates with detailed measurements.

After a discussion of loss assumptions for the collimation regions and a summary of previous calculations, Chapter 6 describes in detail the studies related to remanent dose rates and airborne radioactivity. Various calculation approaches were used and their results are compared with each other as well as with predictions of previous calculations.

Finally, in Chapter 7 results are summarized and discussed.

2 The LHC Beam Cleaning Insertions

Until recently, CERN had two main accelerators and several smaller machines, each serving as injection systems for the respective next, larger accelerator (see Figure 2.1). The Large Electron Positron collider (LEP), which reached its end of operation in November 2000, had a circumference of 26.7 km and was installed 100 metres underground. Leptonic beams were accelerated and collided at a centre-of-mass energy of more than 200 GeV. In addition, the Super Proton Synchrotron (SPS), a 7 km long ring used in the past for studies of antiproton-proton collisions, serves now a number of fixed target experiments.

However, the challenge in modern particle physics research is to probe at higher and higher collision energies. Therefore, the Large Hadron Collider (LHC) project was approved by the CERN Council in December 1994. The machine will provide proton-proton as well as heavy ion collisions with a centre-of-mass energy and a luminosity significantly exceeding those reached by existing accelerator facilities.

The LHC and its experiments are certainly one of the most amazing projects in the current world of particle physics. The design of the machine, as well as its actual manufacturing is of unprecedented complexity, hard to describe within a view pages. Therefore, in the following only those parts of the accelerator are sketched which are essential for the studies discussed in this thesis. A complete description of the LHC accelerator can be found in the published design report [1] and references therein.

2.1 The Large Hadron Collider

The LHC will be a synchrotron-collider which accelerates and stores two intense beams of particles circulating in opposite directions. The layout of the LHC is shown together with other accelerators in Figure 2.1. Its size and structure was given by the former LEP ring which consisted of eight so-called arcs with a bending radius close to 3.5 km linked together by eight 528 m long straight sections. The two beams of the LHC will be accelerated in two separate vacuum chambers side by side in the horizontal plane through the arcs and will cross over at dedicated interaction points (IP) in the centre of those straight sections dedicated to experiments.

Two of these regions, IP1 and IP5, will house large general purpose detectors, called ATLAS and CMS. Two smaller and more specialised experiments, ALICE and LHCb will be installed at IP2 and IP8, respectively. The remaining straight sections will be used for LHC machine installations: to provide the beam dump extraction (IP6), for the accelerating system consisting of Radio Frequency (RF) cavities and for the beam cleaning system (IP3&7), which will be necessary to ensure a stable functioning of the accelerator.

Several pre-accelerators are needed to inject beam into the LHC. The existing CERN accelerator chain consists of Linacs (50 MeV), the Booster (1.4 GeV), the Proton Synchrotron PS (26 GeV) and the SPS (450 GeV). Most of these injectors are able to accelerate heavy ions, thus enabling heavy ion physics also at the LHC.

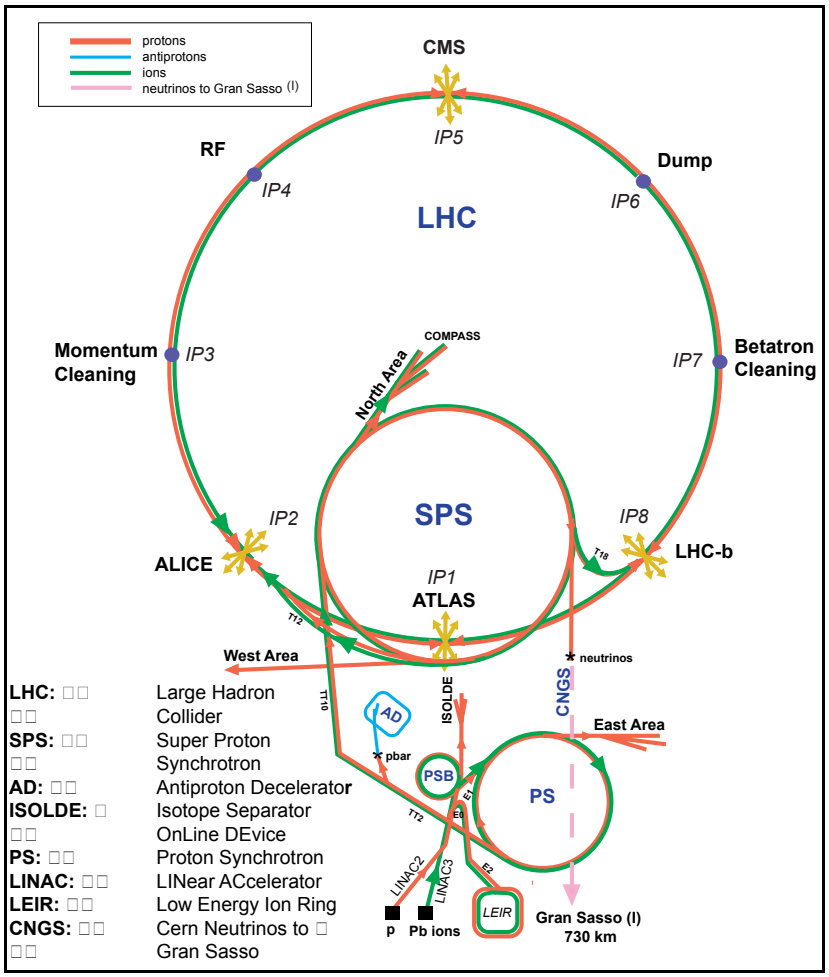

Figure 2.1: Schematic layout showing the different accelerators as well as the assignment of the eight long straight sections of the LHC to experiments and accelerator installations.

The diameter of the LHC tunnel and the highest possible magnetic field determine the maximum possible beam energy, leading with a nominal field strength of 8.4 Tesla and a circumference of 26.7 km to a beam energy of 7 TeV. In the machine protons are not accelerated and stored continuously but the particle beams are subdivided into separate bunches. The beam-beam collisions induce a pertubation in the accelerated beam which is proportional to the ratio of the bunch population and the so-called emittance. The latter reaches a maximum acceptable value imposed by the aperture of the magnets, therefore limiting the number of particles per bunch to about 1.1×10^{11}.

Taking into account that the desired LHC luminosity is 10^{34} $cm^{-2}.s^{-1}$ and given the fact that the so-called beta function at the collision point cannot be reduced arbitrarily (in particular should at least remain larger than the bunch length [2]), the only free parameter in the machine remains the number of bunches. Thus, in to reach the LHC luminosity design value, the number of bunches is given as 2808 and is therefore defining the remaining LHC main parameters as summarized in Table 2.1.

Table 2.1: Parameters of the LHC as a proton collider for both the nominal and the ultimate operation phase of the machine [3].

Parameter	Nominal	Ultimate
Injection Energy / GeV	450.0	450.0
Collision Energy / TeV	7.0	7.0
Number of Bunches	2808	2808
Protons per Bunch	1.1×10^{11}	1.7×10^{11}
Bunch Spacing / ns	25	25
Average beam Current / A	0.56	0.86

Two sets of parameters are given. “Nominal” refers to the design values of the accelerator to be reached within the first years of operation corresponding to 1.1×10^{11} protons per bunch. However, after the accelerator is in stable operation and its capacity can be fully exploited it is expected that without hardware changes the so-called “Ultimate” limits (1.7×10^{11} protons per bunch) can be reached.

The high stored total energy and total beam current make the LHC not only a challenging project with respect to its construction, but also to the operation and protection of the accelerator itself. A large number of especially designed equipment is required for its construction and the existing LEP tunnel will be used for the installation of the LHC. Therefore, together with magnets, the cryogenic system as well as possible shielding also the planning of the installation of the machine becomes an important task, not being facilitated by the space constraints in the tunnel. A typical section of the LHC including a superconducting magnet is shown in Figure 2.2.

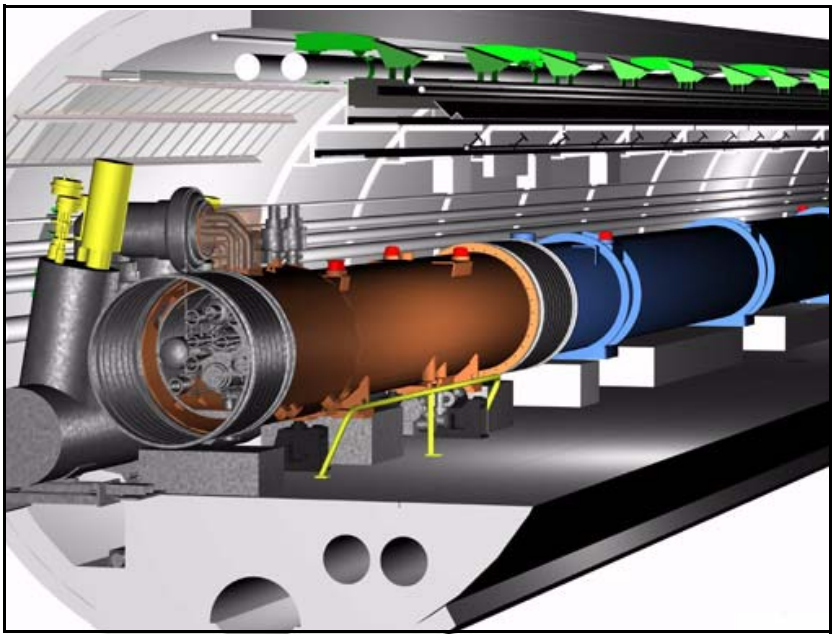

Figure 2.2: Artist’s view of the LHC in its tunnel.

2.2 Collimation

The LHC requires numerous different elements in order to assure its stable operation, one of them being the beam cleaning or collimation system. During the high-energy collisions in the

physics experiments, particles scattered elastically are emitted in the primary beam direction with the same momentum and a slight increase in transverse angle. The same effect occurs along the whole machine due to elastic interactions between the protons and the residual gas nuclei in the vacuum chamber. Furthermore, beam instabilities (non-linear beam dynamics) also contribute to an amplitude increase of the transverse and longitudinal beam distribution. All these effects will progressively push particles outside of the stable region, creating a so-called beam halo.

One of the most challenging tasks in the design of the LHC is the need to ensure this halo to be intercepted at dedicated elements before it hits other parts of the accelerator, *e.g.,* the cold inner part of a super-conducting magnet. Already a few per mille of the scattered particle flux interacting with a superconducting magnet would cause it to quench. Therefore, an efficient collimation system is required in order to ensure stable operation of the machine. For this purpose, the LHC includes two cleaning insertions, defined as those parts of the accelerator ring where particle losses are concentrated. One of which is dedicated to clean off momentum particles, whereas the other captures particles outside a defined transverse boundary, requested to be smaller than the aperture of the remaining accelerator components.

In order to function correctly the LHC requires efficient collimation during all phases of the beam cycle. For both the stability and the protection of the accelerator, collimation plays important roles in preventing magnet quenches from regular beam diffusion, detecting abnormal beam loss and triggering subsequent beam abort. In addition, it enables the passive protection of the super-conducting magnets in case of failures as well as collects most of the particle losses to two specially dedicated regions of the accelerator. The different roles of collimation and the high beam power in the LHC impose many challenges for the design of the collimation system.

2.2.1 Functional Specifications

In detail, each of the two LHC rings will handle a stored beam energy of up to 350 MJ (3×10^{14} protons at 7 TeV), two orders of magnitude beyond the achievements in the Tevatron or HERA [4]. Comparing transverse energy densities, the LHC advances the state of the art by even three orders of magnitude, from 1 MJ/mm^2 to 1 GJ/mm^2 (see Figure 2.3). This makes the LHC beams highly destructive. At the same time the superconducting magnets in the LHC would quench at 7 TeV if small amounts of energy (on the level of 30 mJ/cm^{-3}, induced by a local transient loss of 4×10^7 protons) are deposited into the superconducting magnet coils [5]. Any significant beam loss into the cold aperture must therefore be avoided.

However, beam losses cannot be completely prevented. A so-called ”primary beam halo” will continuously be filled by various beam dynamics processes and the beam current lifetime will be finite [6]. Therefore, the handling of the high intensity LHC beams and the associated high loss rates of protons require a powerful collimation system, fulfilling efficient cleaning of the beam halo during the full LHC beam cycle, such that beam-induced quenches of the super-conducting magnets are avoided in routine operation. In addition, the collimation system must assure the minimization of halo-induced backgrounds in the particle physics experiments, as well as passive protection of the machine aperture against irregular beam losses. For the stability of the machine scraping of beam tails and diagnostics of halo population form an important issue and after regular beam dumps the abort gap must be cleaned in order to avoid spurious quenches.

The difficulty in cleaning a 7 TeV beam halo results from the fact that at those energies most particles will hit a collimator at a small distance from its edge, of the order of one micrometer. Therefore, a large fraction of the traversing particles will leave the collimator with only a small increase in transverse distribution due to scattering. Thus, a so-called multi-stage collimation

system is foreseen, consisting of primary and secondary collimators. The primary collimators define the aperture at which the cleaning system will suppress the halo, whereby the secondary collimators are then used to stop escaping particles.

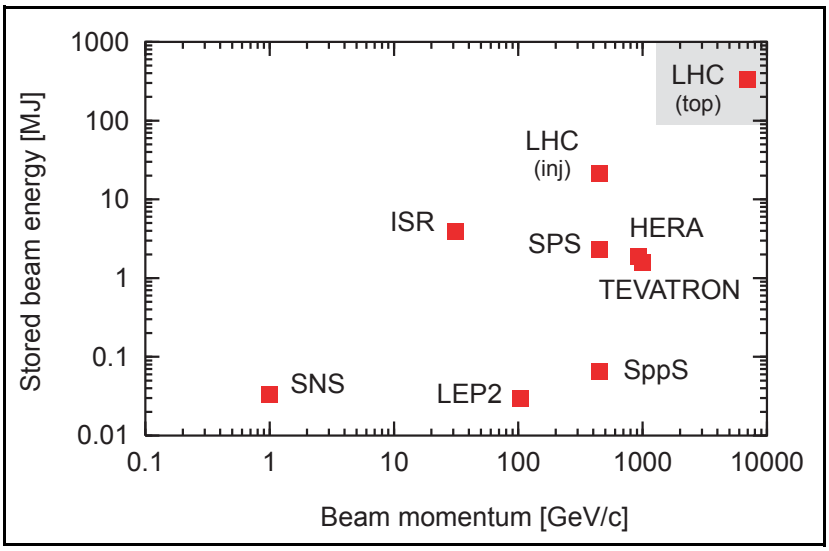

Figure 2.3: Transverse energy density at the collimators versus beam energy for different proton storage rings [4].

Above all, the collimators must have sufficient robustness to fulfil these tasks without being damaged during regular and irregular operational conditions. Design work on an appropriate LHC collimation system started in 1990 [7]. The design evolved significantly over the years [8, 9, 10], reflecting on one side the difficulties to meet the LHC requirements and on the other side the challenge to advance the state of the art in beam cleaning and collimation into a new regime. The latest critical revision of the LHC collimation system started in 2002 [11] leading to a finalization of the collimation design with a possible solution briefly described in the following.

2.2.2 A Potential Final Design

A detailed analysis of possible collimator materials and concepts did not produce any single collimator solution that fulfils all the design goals for the LHC [12]. In particular it was found that a trade-off exists between collimator robustness and collimator induced beam impedance. For example, a collimation system with sufficient robustness (based on graphite like material) would introduce peak performance limitations for the LHC (reduced intensity, increased beta function). A system with sufficiently low impedance (copper based) would likely experience regular damage to the collimator jaws with a resulting loss in cleaning efficiency - thus limiting the peak intensity - and efficiency of LHC operation. On the other hand, a beryllium based system would not resist the specified one turn beam loads and in addition would introduce concerns about toxic materials. Nevertheless, in order to meet the LHC design goals in the present design a number of sub-systems are defined. These sub-systems have specific tasks and can conveniently be fitted into different installation phases. Therefore, the system for beam cleaning and collimation in the LHC will be constructed and installed in three phases [13]. This phased approach relies on the fact that difficulties and performance goals for the LHC are distributed in time, following the natural evolvement of the LHC performance. It is noted that inefficiencies at injection seem adequate, while the situation at top energy cannot be guaranteed to be adequate. Tertiary collimators have therefore been introduced. The phased approach allows to initially operate a collimation system with fewer components than previously foreseen. Further details of the most recent collimation layout and its conceptual design can be found in [14].

Due to the still evolving design of the cleaning insertion, during this work only certain aspects of the new layout could have been taken into account. However, independent of the final design changes, the cleaning insertions will become one of the most radioactive sections at the LHC (*e.g.,* for radiation studies it is estimated that about 30% of all stored LHC protons will be lost in the cleaning insertions at Points 3 and 7). Therefore, the latest officially approved layout for the cleaning insertions is described in the following, as it has also been used in this work.

2.2.3 The Cleaning Layout for IP 3 and 7

The transverse extent of the beam halo is limited by absorbing laterally displaced protons in collimators, called jaws. Those jaws inserted closest to the beam are called primary collimators and define the primary aperture which is normally chosen to be larger or equal to the dynamic aperture of the beam in order not to intercept stable particles. Protons traversing the collimators but not being absorbed are scattered, thus forming a secondary halo which propagates downstream together with the beam. In order to protect the machine from possible damage, secondary jaws are thus necessary to limit the extension of the secondary halo to a value smaller than the geometrical apertures of other accelerator modules.

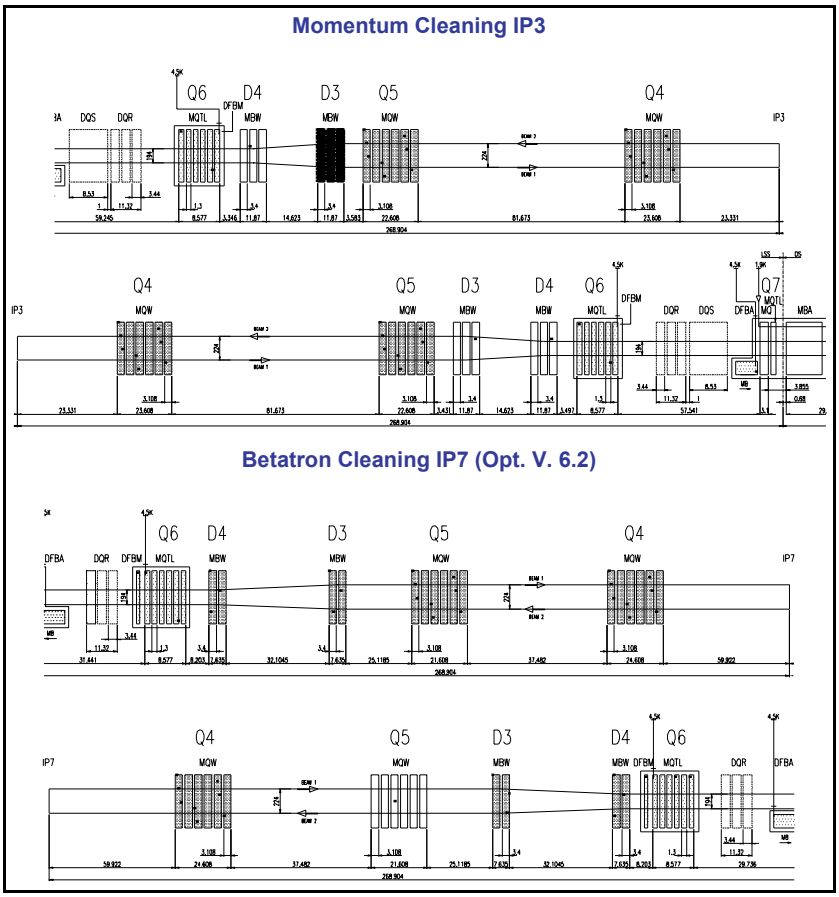

Figure 2.4: Layout of the two cleaning insertions as described in the latest released optics version 6.2.

Two beam cleaning insertions are foreseen, one for momentum (Point 3) the second for betatron cleaning (Point 7), as shown for one half of the straight section in Figure 2.4. Each insertion consists of a 538 m long straight section, with two dispersion suppressors at each end. The cold section of the insertion, *i.e.,* the main cryostat extending from the middle of the adjacent arcs, ends with the Q6 quadrupole. Due to the high-energy deposition at and in the vicinity of the collimators superconducting magnets have from then onwards to be replaced by warm magnets. Just after the cold/warm transition, the two “dogleg” dipoles, D3 and D4, increase the beam separation from 194 mm to 224 mm, which was found to be optimal to

sweep across the secondaries [1]. The optical anti-symmetry and nominal beam separation of 194 mm are preserved by installing an identical arrangement at the exit of the straight section. The quadrupoles Q4 and Q5 are built of 6 modules of 3.1 m, 37 T/m quadrupoles each.

The latest officially released design foresees one primary (TCP) and six secondary (TCS) collimators for the momentum cleaning (Point 3). Similarly four primary and 16 secondary collimators are implemented in the design for the betatron cleaning (Point 7). For both insertions the primary collimators are located between D3 and D4 as well as the secondary collimators are located downstream of D3 between Q5 and Q4, but also amidst single modules of the quadrupoles. Each collimator consists of a pair of jaws inside a vacuum vessel, for cleaning purposes being oriented in different angles with respect to the horizontal axis.

2.3 Ventilation

An important part of the installation that has already been used for LEP is recovered for the LHC design [15]. Air will be supplied at the even-numbered tunnel points (IP2, IP4, IP6, IP8) and extracted via the odd-numbered points (IP1, IP3, IP5, IP7). A summary of the operational principle is shown in Figure 2.5 [16].

Whereas the technical concepts for the tunnels are the same as for the LEP (100% fresh air), the ventilation of the new experimental caverns at the experimental points 1 (ATLAS) and 5 (CMS) uses a different layout. During periods when the accelerator is in operation, the main air volume stream is mainly recycled. Only a fraction of fresh air is provided through the technical cavern. In comparison, the LEP caverns worked with 100% fresh air [15]. The change of concept is justified by a more energy economic solution and a concept that limits the risk of release of radioactive air. Therefore, two mainly different ventilation types are involved, one for the accelerator tunnel and a second for the experimental areas.

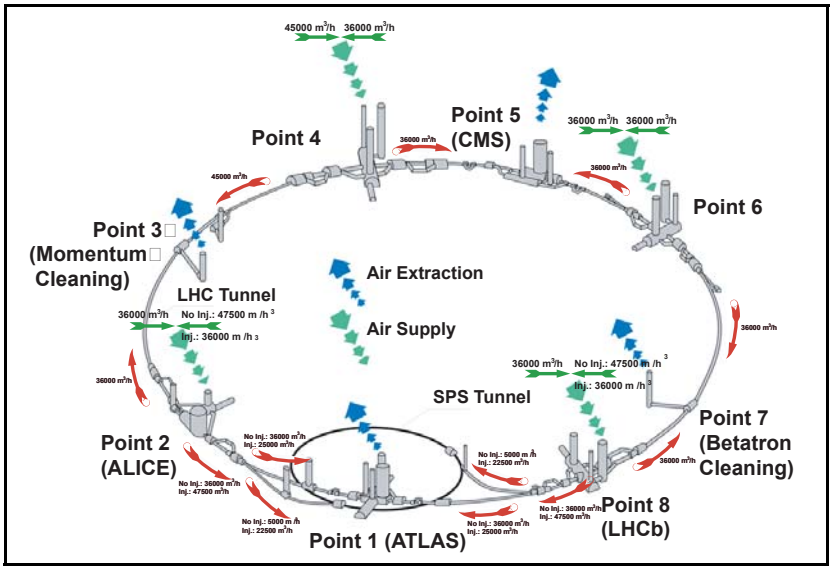

Figure 2.5: LHC ventilation layout.

For the ventilation of the accelerator tunnel areas two normal modes of operation are foreseen: low speed where there is possible access and high speed with no access to the tunnel. In the case of an emergency, a third mode will be realized, which will provide a maximum airflow rate. Please note that all technical areas (*e.g.,* labyrinths and technical caverns) will be ventilated in a different way, as well as all experimental areas will be completely separated because of the use of various gases in the experimental installations. A summary of the current design airflow

rates for the LHC tunnel sections is presented in Table 2.2. Please note that these values only refer to periods of operation, when there is no access to the tunnel.

Table 2.2: Ventilation speeds in m^3/h for the various LHC tunnel sections.

Supply -> Extraction	Injection	Normal	Supply -> Extraction	Injection	Normal
Point 2 -> Point 1	47500	36000	Point 6 -> Point 5	36000	36000
Point 2 -> Point 3	36000	36000	Point 6 -> Point 7	36000	36000
Point 4 -> Point 3	45000	45000	Point 8 -> Point 7	36000	36000
Point 4 -> Point 5	36000	36000	Point 8 -> Point 1	47500	36000

3 Radiological Considerations and Constraints

An integral part of the design of a new accelerator is the protection of personnel and environment against prompt and remanent radiation. The framework of radiation protection is given by legal limits defined in the national legislation of each country which are usually based on recommendations of international expert commissions. CERN, as international organization, has authority and control over the whole of its site with competence to establish its own safety policy and regulations for its staff and property, independently of the Host States [17]. However, as a general rule, CERN must ensure a level of safety which may not fall below the standard of the most advance regulations of the Host States. In case CERN regulations are lacking or incomplete, the regulations of the Host State concerned are applicable on its territory.

Furthermore, CERN and the French government have signed an agreement in which all safety aspects (including radiation protection) of accelerator installations on French territory are put under the control of the French authorities and require approval prior to operation of new or modified facilities [18]. As this agreement includes the LHC, CERN is obliged to demonstrate the compliance of design and operation with its own safety regulations and standards. With regard to radiation protection, a wide range of aspects have to be covered including shielding of work-places against prompt radiation, activation of the accelerator and environment, releases of radioactive air, gases and fluids as well as the protection of personnel during repair and maintenance against residual radiation from induced radioactivity.

This thesis forms part of the required radiation safety studies for the LHC. Thus, the applicable safety regulations have to be incorporated into a discussion of results and the aspects most relevant to this work are summarized in the following.

3.1 The Radiological Protection System

The International Commission on Radiological Protection (ICRP) in 1990 [19] recommended that radiological protection should be based on three principles: Justification, Optimization and Limitation. Justification involves showing that a practice produces a sufficient benefit to individuals or society to offset the radiation detriment it causes. Optimization is the balancing of constraints on individual doses, risks, number of persons involved, cost of protection measures, *etc.* Limitation is the keeping of actual exposures below specified limits. The ICRP recommendation was adopted by the European Directive 96/29 and integrated verbatim into most of the European countries' national radiation protection legislation. The following section examines these three principles in defining policies (see [20] for more details) which will be used later for assessments of maintenance scenarios in the LHC cleaning insertions.

3.1.1 Justification

The Swiss “Ordonnance sur la Radioprotection” [21] gives guidance on how to justify a practice[1]. It suggests that a practice is justified when the advantages clearly outweigh the disadvantages and that no alternative solution exists which would not involve radiation exposure. Clearly particle physics cannot proceed in a way other than giving rise to certain means of radiation exposure and society has deemed it as important. With regard to small exposures the guideline states that any activity which gives rise to an effective dose of less than 10 µSv per year can automatically be considered justified.

3.1.2 Optimization

Having justified the activity, the Swiss Ordonnance defines that radiation protection is optimized when:

1. different appropriate solutions have been evaluated and judged against each other from the radiation protection point of view,
2. the decisional process leading to the chosen solution can be reconstructed at any time, and
3. the risk of failure and the elimination of radioactive sources have been taken into account.

The “small-exposure” guideline in this case states that optimization can be considered as respected if the activity never gives rise to an annual dose of more than 100 µSv for persons exposed because of their own professional activity or 10 µSv for circumstances not linked with their own professional activity.

3.1.3 Annual Dose Limits

Dose limits, expressed in terms of the effective dose received by a person, can be classified as follows [20]:

Legal Limits

The fundamental constraint, derived from the legislation of most European countries, is that the dose received by individually monitored personnel during any consecutive 12-month period must not exceed 20 mSv. However, further special restrictions apply to women of child-bearing age. Contractors' personnel are also subject to this dose limit, but in addition CERN imposes a limit [22] which is proportional to the time spent on the site of the Organisation. This limit is set at 1 mSv per week, averaged over the time spent at CERN, but must not exceed 20 mSv over 12 consecutive months, taking into account doses received elsewhere. The effective dose received by persons who are not individually monitored shall not exceed 1 mSv per year.

Design Limits

The optimization of doses which could be received by personnel starts already during the design phase of a new installation. In this case legal limits should not be applied due to possible uncertainties in the estimations. Hence, for the LHC it is sensible to plan maintenance operations with a Design Limit for the annual dose of 5 mSv. Obviously, the dose objective must stay below this limit.

1. Similar texts can be found in other national legislation or guide lines.

3.2 Maintenance

Designated areas at CERN are subdivided into Supervised and Controlled Areas [22]. Working conditions in Supervised areas are constantly kept under review, however working personnel - in the course of their normal work - shall not receive effective doses exceeding 1 mSv per year. Controlled areas are designated areas where normal working conditions require persons to follow well-established procedures and to have been given specific information concerning radiation exposures. The annual dose limits combined with remanent dose rates in respective working ares lead to the following constraints.

3.2.1 Derived Constraints

Based on the optimization principle all work in Controlled Areas must be planned and expected doses estimated. If this estimate exceeds 100 µSv an optimization must be made balancing the doses against the cost of protection measures (time, shielding, distance and remote handling).

In this respect long-term experience at high-energy accelerators has proved the usefulness of the following dose rate reference values [20]:

1. 100 µSv/h (Limited-stay areas): Above this value all work must be planned and optimized and wearing of additional, active dosimeters is obligatory.
2. 2 mSv/h (High-radiation areas): Above this value the intervention time in the zone must be severely limited. Workers from firms outside CERN who only have a temporary contract with the firm are not allowed to work in these zones. When dose rates exceed this value, remote handling of the components concerned should be seriously envisaged.
3. 20 mSv/h: In regions where dose rates are above this value, no work is allowed since dose limits would be too easily exceeded and the annual design dose would be received in less than 15 minutes. Remote handling of objects is essential.

3.2.2 Work and Dose Planning

Legal Requirements

As mentioned above, the radiation protection principles as recommended by the ICRP and adopted by the European Directive 96/29 are based on three components: justification, optimization and limitation of any personnel and collective dose. Consequently, the national European radiation protection legislation force the operators of installations where there is a risk from ionising radiation to comply with the optimization principle and to keep the personnel and collective dose as low as reasonably achievable (ALARA). The corresponding legal bodies regularly control the compliance of work habits with regard to the ALARA principle.

One essential part of the optimization principle is work and dose planning [20]. The question when work planning will be needed is answered by the Swiss and French legislation in a slightly different manner: According to the Swiss law, work has to be optimized (*i.e.,* job and dose planning are necessary) as soon as a radiation worker could receive more than 100 µSv within a year due to this activity. In France any intervention in Controlled Radiation Areas[1] has to be planned in advance and dose estimates have to be performed.

1. The definition of a Controlled Radiation Area in France corresponds to the one for a Limited-stay area at CERN

At CERN, intervention and dose planning for work in Limited-stay areas is not yet fully implemented. However, it is already common practice in areas with special risks such as target areas, from which the following main guidelines are extracted.

Basic Principles

Effective and realistic work planning should comprise the following aspects - depending on collective dose and special risks (*e.g.,* contamination):

- specification of radiological training and monitoring requirements,
- establishment of intervention plans, procedures or work packages (preparatory meeting, *etc.*),
- prior estimation of individual and collective dose,
- evaluation of contamination risks,
- consideration of the use of work processes and special tooling to reduce the time spent in the work area (*e.g.,* staging and preparation of necessary materials and special tools; prefabrication and work shop preparation outside the active areas),
- the use of mock-ups for complex tasks,
- the use of “dry-runs” for the activities using applicable procedures,
- engineering, design and use of temporary shielding,
- provision for waste minimisation and disposal,
- a review of emergency procedures and plans,
- establishment of success or completion criteria, with contingency plans to anticipate difficulties,
- in case the total accumulated dose exceeds the established estimate by 25% or more, a periodical review regarding work methods becomes necessary.

During the work, the operational dosimetry system is used to control the doses received by the persons involved. The measured values must be regularly compared to the estimated ones, thus enabling an early warning of dose over-runs and a possible correction in the work methods applied. At the end of a job, a post-mortem analysis has to be performed in order to improve future interventions by profiting from the experience of the past.

3.3 Activation of Air

In an assessment of air activation two groups of persons have to be considered: personnel entering a tunnel or experimental area which has not been vented with fresh air prior to the access and the general population outside the CERN boundary. With regard to the latter group estimates for different exposure pathways have to be taken into account, radioactive air being only one of them. According to the CERN regulations [22] radioactive air emissions must be limited in such a way that the annual effective dose from these releases for persons living outside the CERN boundary does not exceed 0.2 mSv per year. In addition, the sum of the exposure to radioactive air emissions and liquid effluents shall not exceed 0.3 mSv per year.

3.3.1 Radiation Workers

Official restrictions for the concentrations of radioactive isotopes produced in air only exist for persons who are considered as professionally exposed to radiation. Respective values can be found in both the Swiss [21] and the French [24] legislation. The French limits are in fact identical to those published in 1966 based on very early ICRP recommendations. The Swiss limits refer to the same assumptions as used for the ICRP Publication 30 [25] based on the

dose limits of ICRP Publication 26 [26]. New intake limits have been published by ICRP in their Publication 61 [27] based on the dose limits given in Publication 60 [18]. Since these intake limits are about a factor of three lower than earlier values it is to be expected that concentration limits will also be reduced by this same factor in the near future. Unfortunately, the French and Swiss laws do not give limits for all isotopes produced in air, hence values for the missing isotopes have to be deducted from those isotopes with similar decay and chemical characteristics (*e.g.*, ^{13}N from ^{11}C or ^{27}Mg from ^{28}Mg).

If a mixture of radionuclides is present an additive rule has to be applied, weighting the various nuclides with the inverse of limits or guideline values

$$\sum_{i=1}^{n} \frac{Q_i}{L_i} < 1 \qquad \text{(i)}$$

where Q_i is the specific activity of species i and L_i is the corresponding limit or guideline value, whereby the sum extends over all radioactive species contained in the air.

As all the above limits are valid for professionally exposed workers they are only applicable in corresponding cases, *e.g.,* when access to tunnels or experimental installations is required which are not vented and the waiting-time after beam-off has to be estimated.

3.3.2 Reference Values for Air Releases

For assessing the effect of air releases from accelerator tunnels, calculations have been made of the doses to so-called critical groups for each isotope that could be created in interactions of prompt radiation with air [28,29]. Based on these studies release reference values were derived. These values are calculated with the premise that the contribution to the off-site dose from radioactive emissions to the atmosphere cannot be greater than 0.2 mSv/year. The calculated values refer to the Swiss Customs Officers outside CERN, who form the critical group for releases from the ISOLDE accelerator, and are partially based on specific isotopes.

These reference values have been used in the past for the evaluation of radioactive air releases from the LHC. However, they might not inherently be conservative as they were computed for the rather specific conditions of a certain release point. Therefore, a detailed radio-ecological calculation, as sketched in the following, is now considered to be the more appropriate approach and less emphasis is put on the old reference values.

3.3.3 Doses to the Population

For off-site doses the regulatory limits are based on the effective dose to the population. However, the effective dose is a theoretical concept and cannot be measured directly but only estimated by measuring operational radiation protection quantities or calculated by using appropriate models. This holds in particular true in the case of environmental exposure to the population due to radioactive releases, where radio-ecological models, which describe the transport, dispersion and accumulation of radioactivity in various environmental matrices, have to be combined with radiological models transforming an external exposure or an intake of radioactivity into the effective dose.

The environmental impact of accelerator facilities or other activities, which are likely to release radioactivity into the environment, must therefore be assessed in terms of activity densities found in the environment and in terms of the effective dose to the critical group of the population living in the area of concern [29]. The environment is a very complex system, which is impossible to describe precisely. In addition, the “true” behaviour of the receptor (critical group

of the population) is not known and can be predicted only with some uncertainty. Similarly, the time profile of radioactive releases in experimental installations such as accelerator facilities may vary.

Therefore, usually a so-called screening approach has to be applied [30]. This approach makes use of simplified models concerning release scenarios, behaviour of the released radioactivity in the environment and the habits of the population, all of which are known to overestimate the activity densities and the effective doses. The screening approach is sufficient to prove that there is no exposure of the population above the regulatory limit, however if the limit is exceeded, the calculations have to be refined by entering more accurate site-specific input parameters or by improving the models to be more realistic. The degree into which screening techniques and the site-specific information shall be used depends upon the balance between the expected effects of the radioactive releases and the resources needed to use the models.

A complete description of the program used for the calculation and the models applied for the assessment of the environmental impact of radioactive releases from CERN facilities can be found in [29, 30]. However, a thorough environmental assessment is outside the scope of this work which is focused on the effect design parameter changes on the radioactive releases.

4 Simulation Methods

The importance of particle shower simulations in radiation physics studies has grown considerably during the last years, in parallel to the rapid increase of available computing power. In the past calculations, *e.g.,* for the design of shielding or the estimation of activation, were performed with analytical methods leading often to rather conservative estimates. With the increase in size and complexity of accelerators, together with their financial aspects, as well as with the steady decrease of the limits in radiation protection accurate calculations became an essential part in the design and operation of any new facility. In particular, Monte Carlo codes for the simulation of particle transport and interactions are now quasi-standard in the field of radiation protection.

The application in the design of a facility such as the LHC constitutes an enormous challenge for the code and its underlying models: It should be able to describe in detail the scattering of low-energy neutrons as well as hadronic interactions at energies beyond what can be tested with present accelerators. It should include user-friendly tools to model the often very complex geometry and robust means of scoring a variety of physical quantities, such as fluence, at any point-of-interest. And finally, as CPU-power and need for complexity often increase at the same rate, it is desirable that the code delivers statistically significant results in a reasonably time.

At CERN, the FLUKA Monte Carlo code and its predecessors have been successfully used for decades in radiation protection studies. In fact, the code has its roots in this field and is thus the most appropriate choice for the studies presented in this thesis. In the following, a short summary is given about code with particular emphasis on models and techniques used in this study.

4.1 The FLUKA Code

The development of the particle interaction and transport Monte Carlo (MC) code FLUKA began in the early sixties and was used in radiation shielding studies for the design of the Super Proton Synchrotron (SPS) at CERN (see [31, 32]). The first versions of FLUKA were based on data from shielding experiments as well as on phenomenological parameterizations and the Thermodynamic Model [33] for hadron production in high-energy hadron-hadron collisions. “FLUKA” stands for FLUktuierende KAskade which reflects the necessity to describe fluctuations of the energy deposition in calorimeters with purely analog MC methods.

Since that time FLUKA has been continuously improved (see [34, 35] and references therein) and extended by an international collaboration of physicists and appears now as a multi-purpose MC code which is capable of simulating all

components of particle cascades in matter from TeV-energies down to that of thermal neutrons. Its predictive power is based on a large number of studies benchmarking FLUKA results against experimental data (see [36] and references therein).

In its present design FLUKA is both a fully analog code - capable of treating all physical processes as closely as possible to their natural way of occurrence - and offers in addition a long list of biasing techniques which can be activated on request but obviously implies the loss of the analog description. It is capable of simulating the whole high-energy hadronic and electromagnetic cascade from TeV to thermal neutron energies in a single simulation run since the various components are consistently integrated. Several other code systems, such as CALOR, HERMES, LAHET or MCNPX (see [37, 38, 39, 40, 41]) are available, but most of them differ from FLUKA by being essentially built as assemblies of different specialized codes. It is perhaps worth noticing that all these codes use a version of the FLUKA high-energy hadron generator, and all of them - including FLUKA - are based on a version of the HETC nuclear evaporation model [42, 43]. In addition, it should be noted that in MCNPX low-energy neutrons are treated in a more accurate way due to improved cross-section libraries (available below 150 MeV). However, in this study low-energy neutron processes are only of minor importance, thus the FLUKA code was chosen for all simulations.

Please note that the pure analog MC technique would have the disadvantage of being slow relative to other computational techniques and providing only a statistical estimate of the correct answer rather than a precise result. An obvious way to reduce the statistical error in an analog calculation is to increase the number of histories. However, the error decreases as the inverse of the square root of the number of histories, thus the computer time required may become very large in order to reach small statistical uncertainties. Fortunately, as already mentioned dedicated techniques exist in order to reduce the error without unduly increasing the computational effort, as well as there are techniques to decrease the computer effort without appreciably increasing the error, or even for making a reasonable reduction in both error and computational effort.

The central concept for improving the efficiency of MC processes is to attach to each particle a weight (a numerical value of its importance to the desired tally response). In the actual physical situation or in the direct analog simulation, the weight of each particle is unity and the analog model works well when a significant fraction of the particles contribute to the final estimate and can be compared to detecting a significant fraction of the particles in the physical situation. On the other hand, a nonanalog Monte Carlo model attempts to follow "interesting" particles more often than "un-interesting" ones. An "interesting" particle is one that contributes a large amount to the quantity that needs to be estimated. If each particle is given some arbitrary weight, or importance, and if the detector response is defined in terms of the sum of all weights of the particles contributing to the response, the transport description of particles is unchanged. Thus, for all estimates not the sum of the particles but the sum of the particle weights has to be considered.

Particle interactions are described in FLUKA as a multi-step process involving various models, each of which acting in a different energy range and describing a different process. For example, the inelastic scattering of a 7 TeV proton on a nucleus initially proceeds through a realization of the Dual Parton Model. Particles created in these high-energy primary interactions are followed as they move through the remaining nuclear matter based on a Generalized Intranuclear Cascade Model. Finally, the nuclear pre-fragments de-excite according to models for evaporation, fission and nuclear fragmentation. In the following, a more detailed account is given on these various steps of a high-energy hadronic interaction as they determine predictions for activation and remanent dose rates, both of which being integral parts of this study.

4.1.1 The Dual Parton Model

One of the most successful models in the field of high-energy inelastic nuclear interactions is the so-called Dual Parton Model (DPM) [44]. It provides the theoretical framework in FLUKA for the description of hadron-nucleus interactions above a few GeV. In the following, a general overview is given whereby a more complete description can be found in a recent review [45].

Most particles produced in high-energy hadronic interactions have small transverse momenta with respect to the collision axis. The underlying interaction mechanisms are frequently called *soft processes* and cannot be described by Quantum Chromodynamics (QCD). The hadron dynamics involves length scales of about 1 fm corresponding to a strong coupling constant of the order of unity.

The DPM is based on the Dual Topological Unitarization (DTU) scheme [46, 47, 48] and on the perturbative Reggeon Field Theory (RFT) [49, 50], where high-energy interactions are described by the exchange of *Reggeons* and *Pomerons*. In addition, the DPM incorporates the partonic structure of hadrons. A baryon is assumed to consist of a valence quark, a valence diquark and a certain number of so-called *sea*-quark-antiquark pairs. Correspondingly, a meson is assumed to consist of a valence quark, a valence antiquark and also a certain number of sea-quark-antiquark pairs.

Given these assumptions, an inelastic hadron-hadron (nucleon) interaction is then treated in two steps: *(i)* each colliding hadron splits into coloured systems (valence and sea quarks) and *(ii)* each coloured system of one of the colliding hadron combines with the system of complementary colour of the other colliding hadron which finally fragments into colour neutral *chains* of hadrons.

In order to describe inelastic interactions involving nuclei the DPM uses the Gribov-Glauber approximation [51, 52, 53] which relates the inelastic hadron-nucleus interaction to inelastic scattering processes of the incoming hadron with individual nucleons.

The MC realization of the DPM which is implemented in FLUKA [36] describes each hadron-nucleon interaction by the exchange of only one Pomeron or Reggeon and is, therefore, limited to laboratory energies below about 20 TeV. Furthermore, this realization does not provide a description of nucleus-nucleus interactions. In FLUKA the DPM is applied to hadronic interactions with laboratory energies down to 4 GeV. So far, scattering processes in the energy range between 3.5 GeV and 4-5 GeV are treated by a specific resonance production and decay model [54].

4.1.2 The Generalized Intranuclear Cascade Model

During the first step of a high-energy hadronic collision new hadrons are produced which may re-interact with the remaining nuclear matter. These processes are most successfully described in the framework of the Intranuclear Cascade (INC) model [55, 56, 57]. This model was developed at the very beginning of the history of energetic nuclear interaction modelling and has undergone tremendous improvements since then. It is intrinsically a Monte Carlo model, well suited for numerical applications, where no closed analytical expression can be derived without severe approximations. In the energy range between pion production threshold (several hundreds of MeV) and a few GeV, INC models are practically the only available tools to describe hadron-nucleus interactions. At lower energies, a variety of preequilibrium models with more robust physics foundations than those of the INC ones are available.

Classical INC codes are based on a more or less accurate treatment of hadron multiple collision processes in the nuclei, with the target assumed to be a cold Fermi gas of nucleons. The hadron-nucleon cross-sections used in the calculations are free hadron-nucleon cross-sections. Usually, the only quantum mechanical concept incorporated is the Pauli principle. Possible hadrons are often limited to pions and nucleons, pions being also produced or absorbed via isobar formation, decay and capture. The Fermi motion is taken into account when considering elementary collisions, both for the purpose of computing the interaction cross-section and to produce the final state particles.

In addition to these features Generalized Intranuclear Cascade (GINC) models include extensions for high and low energies. At high-energy, hadrons re-interact with reduced probabilities which is taken into account by assigning a formation time to the produced hadron: the higher the energy of the secondary hadron the lower is its probability for re-interactions. At very low energies GINC typically consider quantum nuclear effects and multibody interactions.

FLUKA contains a very detailed implementation of the GINC [36]. Hadrons propagate in the nuclear medium like free particles, however, on curved trajectories determined by a nuclear mean field and with kinetic energies which take into account the average nuclear potential. Re-interactions are based on free-space cross-sections considering the Fermi motion of nucleons in the determination of the total collision energy. All interactions occur in a completely incoherent and uncorrelated way, disregarding coherence or diffractive effects. No multibody or cluster processes are included, with the exception of pion absorption. Furthermore, quantum effects are limited to Pauli blocking. The transition between the intranuclear cascade and the final thermalization of the spectator nucleus is described by a preequilibrium model [58], based on an exciton formalism called Geometry Dependent Hybrid Model (GDH) which will be sketched in the following.

4.1.3 The PEANUT Model

The low-medium energy implementation of the INC model in FLUKA (up to a few GeV) is called PEANUT (for PreEquilibrium Approach to NUclear Thermalization). Presently, PEANUT handles interactions of nucleons, pions, kaons, γ rays and the stopping of negative muons with nuclei from about 3.5 GeV down to the reaction threshold (or 20 MeV for neutrons). In PEANUT, the reaction mechanism is modelled by the explicit intranuclear cascade smoothly joined to a statistical (exciton) preequilibrium emission with a smooth transition around 50 MeV for secondary nucleons, and 30 MeV for primary ones.

At the end of the INC stage a few particles may have been emitted and the input configuration for the preequilibrium stage is characterized by the total number of protons and neutrons, by the number of particle-like excitons (nucleons excited above the Fermi level) and hole-like excitons (holes created in the Fermi sea by the INC interactions) as well as by the “compound” nucleus excitation energy and its momentum. In both stages, INC and exciton, the nucleus is modelled as a sphere with a density given by a symmetrized Woods-Saxon distribution [59]. The preequilibrium process in the exciton model is described as chain of steps, each step corresponding to a certain number of excitons, where an exciton can be either a particle above the Fermi surface or below, as a hole. The nucleus proceeds in this chain through nucleon-nucleon collisions which increase the exciton number by two units. The chain stops, and equilibrium is reached, when either the exciton number is sufficiently high or the excitation energy is below any emission threshold [36].

At the end of the preequilibrium stage a compound nucleus is left in equilibrium. This nucleus is characterized by its charge, mass number and momentum and carries a certain excitation energy shared by the nucleons.

4.1.4 Evaporation, Fragmentation and Nuclear De-excitation

The excitation energy of the compound nucleus can be higher than the separation energy, thus, nucleons and light fragments can still be emitted. In FLUKA the emission process is described as an evaporation of nucleons, deuterium, tritium, ^{3}He and of α-particles from a “hot” system using excitation energy dependent level densities [60].

In case of heavy nuclei a fraction of the excitation energy might also be spent to induce collective deformations, *i.e.*, to cause fission processes. In FLUKA the calculation of the fission probability is based on a statisctical method [60, 61, 62]. The masses of the two fragments obey charge and excitation energy dependent distributions [36]. After the fission process both fragments are treated independently, being possibly able to emit further particles.

For light prefragments the statistical assumptions and the sequential emission scheme which underlie classical evaporation models may become invalid. This can be due to the fact that a moderate excitation energy can already represent a substantial fraction of the total energy of the prefragment. Therefore, in FLUKA the so-called Fermi Break-up model [60, 63, 64] is applied to prefragments with mass numbers below 18. It is assumed that the excited prefragment disassembles in one step into two or more fragments. All combinations formed by up to six fragments are considered.

A similar process of nuclear fragmentation, frequently called *multi-fragmentation*, may occur in medium and heavy nuclei and is characterized by the “emisson” of low-energy complex fragments. So far, this process is not implemented in FLUKA.

Evaporation processes become energetically impossible when the nuclear excitation energy of a prefragment is lower than any energy necessary for nucleon or fragment emission. The residual excitation energy is then dissipated through the emission of photons. In FLUKA the prefragment proceeds through consecutive photon emissions until the ground state of an isotope (*residual nucleus*) corresponding to the mass and charge of the prefragment is reached [60].

4.2 Induced Radioactivity

When a high-energy hadron interacts with a nucleus, neutrons, protons and other fragments may be emitted, converting the struck nucleus to that of a different isotope, most probably of a different element, which has a high chance of being radioactive. Some of the secondary particles emitted in an interaction may have sufficient energy to go on and cause further activation by fragmentation reactions or capture. Hence, although the overall quantity of radioactivity induced in an accelerator will depend on the primary beam loss, the probability of producing a particular isotope will depend on the composition of the material struck, the spectrum of secondaries produced and the production cross-section of the isotope concerned. The amount of a radioactive isotope present at any given time will also depend on the isotope half-life, the time that the accelerator has been in operation as well as the time that the activity has had to decay since operation stopped. Due to the complexity of the processes governing the amount of radioactivity in an accelerator at any one time makes it very difficult to quantify the activity in any detail. Therefore, several - partly simplified - methods have been established.

4.2.1 Calculation from Star Densities

This method used to determine specific and total activities requires knowledge of the so-called *star density* in the region of interest. A *star* stands for any inelastic hadronic interaction (*e.g.*, spallation) above a certain energy threshold, typically set to 50 MeV. Based on the assumption

that the high-energy cross-section for the production of specific isotope, σ_p, is roughly constant with energy, the use of experimental values for these cross-sections combined with the inelastic cross-section, σ_i, computed by FLUKA for a particular bulk material allows one to calculate the specific activity.

Hence, multiplying the number of isotopes per interaction (star), ξ

$$\xi = \frac{\sigma_p}{\sigma_i} \qquad \text{(ii)}$$

with the star density *s* (in units of stars per second, cm^2 and primary particle) and with the primary interaction rate *N* yields the production rate density Θ (in units of isotopes per second and cm^2). The specific activity as a function of irradiation t_i and cooling time t_c can then be expressed as

$$a(t_i, t_c) = \Theta \cdot (1 - \exp(-\lambda t_i)) \cdot \exp(-\lambda t_c). \qquad \text{(iii)}$$

This method allows fast first estimates of radionuclide production. However, it cannot take into account any energy dependence of the isotope production cross-section (*e.g.,* the correct threshold behaviour) and depends to some extend on the lower energy threshold for the definition of a star (here 50 MeV). Furthermore, activation by low-energy neutron scattering and thermal neutron capture is not taken into account.

4.2.2 Calculation from Hadron Track-length Distributions

The total track-lengths of hadrons, Λ, in any region of interest as a function of particle type and energy results - after division by the volume - in particle fluence spectra. If the track-length spectra are folded with energy-dependent partial cross-sections for a certain isotope production channel and summed over all target nuclei and hadron components in the cascade one obtains the yield Y_i of a radionuclide *i*:

$$Y_i = \sum_{j,k} n_j \cdot \int \sigma_{ijk}(E) \Lambda_k(E) dE. \qquad \text{(iv)}$$

Here, n_j is the atomic concentration (per cm^3) of element *j* in the material and σ_{ijk} is the cross-section for the production of radionuclide *i* in the reaction of a particle of type *k* and energy *E* with the nucleus *j*. The quantity Λ_k is the sum of track-lengths (in cm) of the hadrons of type *k* and energy *E*. This yield multiplied with the primary interaction rate *N* gives again the production rate density Θ to be inserted into Equation *(iii)* for the calculation of the specific activity.

The quality of predictions of isotope production based on this method depends strongly on the cross-sections used. If reliable experimental or calculated values are available, this method is considered to be the most accurate approach to calculate isotope yields. Furthermore, it avoids statistical uncertainties inherent to an explicit simulation of isotope production (see below). However, it is less universal than the latter as it requires the availability of cross-sections and an additional post-processing step after the simulation which can be quite cumbersome in complex geometries with many different regions and materials.

The approach of folding track-length spectra with cross-sections is typically used in applications where activation has to be calculated for materials with low density, *e.g.*, gases, in which other methods would fail for statistical reasons due to the low inelastic interaction

probability in the medium. In this study is has been used to calculate air activation in the tunnel of the LHC beam cleaning insertions.

In particular, for LHC-applications a data base with evaluated cross-sections for isotope production in air is available [65] and was used in a post-processing step together with track-length distributions from the FLUKA simulation. To be consistent, the upper energy limit for scoring has to be set to 10 TeV, as well as the lower limit for charged hadrons to 10 MeV. The low-energy neutrons have to be scored in the 72-group structure of FLUKA. Due to the low-energy neutron implementation in FLUKA and the format of the partial cross-section tables these spectra have to be scored on a logarithmic basis in energy, *i.e.*, in ten energy intervals per decade above 19.6 MeV and according to the multi-group energy structure below this energy.

4.2.3 Direct Simulation of Residual Nuclei Production

As already discussed, a wide range of models in FLUKA describes isotope production, each acting at different energies: the Glauber-Gribov approach together with the Dual Parton Model describes the high-energy (above several GeV) primary interactions with target nucleons, a Generalized Intranuclear Cascade model (including preequilibrium emission) treats interactions below a few GeV, and various mechanisms are implemented for nuclear de-excitation and fragmentation (evaporation, fission, Fermi-breakup, γ de-excitation). Multi-fragmentation is not taken into account in FLUKA which might pose limitations in the predictions of intermediate and small-mass isotopes from heavy elements. Low-energy neutrons ($E <$ 20 MeV) may also produce radioactive isotopes, whereby in this case their yield is directly calculated from tabulated data.

FLUKA allows one to score the total yield of radionuclides and the yield produced by low-energy neutron interactions separately. These results are then post-processed [66] taking into account the decay chains and buildup of isotopes, as well as the correct irradiation profile of the experiment. Based on these results the specific activities of the produced isotopes, as well as their statistical error can be calculated.

This approach is the most universal one of those discussed in this Chapter as it allows the computation of activation in arbitrary geometries and materials. Of course, it strongly depends on the predictive power of the models for isotope production. For example, if descriptions are missing for certain aspects of the fragmentation process (*e.g.,* a model for multi-fragmentation in FLUKA) predictions can be wrong by large factors. In addition, it can be only used when statistically significant results can be reached within a meaningful time, therefore not in case of low-density regions such as for example air.

4.3 Remanent Dose Rates

In an inelastic reaction of a high-energy hadron with a nucleus, many individual nucleons and some clusters of nucleons will be ejected from the struck nucleus during the various phases of the interaction. Depending on the mass of the remaining fragment(s) with respect to the mass of the original target nucleus the interactions are classified as spallation, deep spallation/fission or multifragmentation [67]. The residual nucleus will be left in a highly excited state and will most probably be unstable against radioactive decay. It will attempt to reach a stable configuration by a succession of decays, of gradually increasing lifetime (possible exceptions might be metastable states). Low-energy neutrons and protons interact with nuclei via resonance interactions, but these processes generally result in the removal of only a few nucleons from the struck nucleus which is left in a near-stable configuration.

Not all of the radioactive daughter nuclei from these interactions will contribute directly to the dose rate from an object struck by high-energy hadrons, measured some time after the irradiation: those isotopes having very short half-lives may have decayed already, while those with long half-lives may not decay at a rate high enough to contribute significantly to the dose rate. Moreover, the remanent dose rate cannot be related to the charge and mass of the target nucleus in a simple way. It strongly depends on the cross-sections of reaction channels leading to radioactive isotopes and their radioactive decay properties.

4.3.1 Simplified Formulas

Corresponding to their half-lives, different isotopes contribute at different cooling times. For small radioactive objects these contributions can be estimated assuming a point source of photons and neglecting attenuation:

$$\frac{dD}{dt}\left[\frac{Sv}{h}\right] = \frac{10^{-8}}{7} \cdot \frac{A(t_c)\sum I_\gamma E_\gamma}{r^2} \qquad \text{(v)}$$

where $A(t_c)$ denotes the activity (in Bq) of a certain isotope at cooling time t_c. The different gamma lines are taken into account in the weighted sum over their intensities I_γ and energies E_γ (in MeV), and r (in cm) is the distance to the point source. The leading factor contains conversion factors for energy and time, 4π from the point source approximation as well as the tissue energy absorption coefficient μ_{en}/ρ which is about 0.031 cm^2/g for an average photon energy of 800 keV (see Fig. 4.1 as taken from [68]).

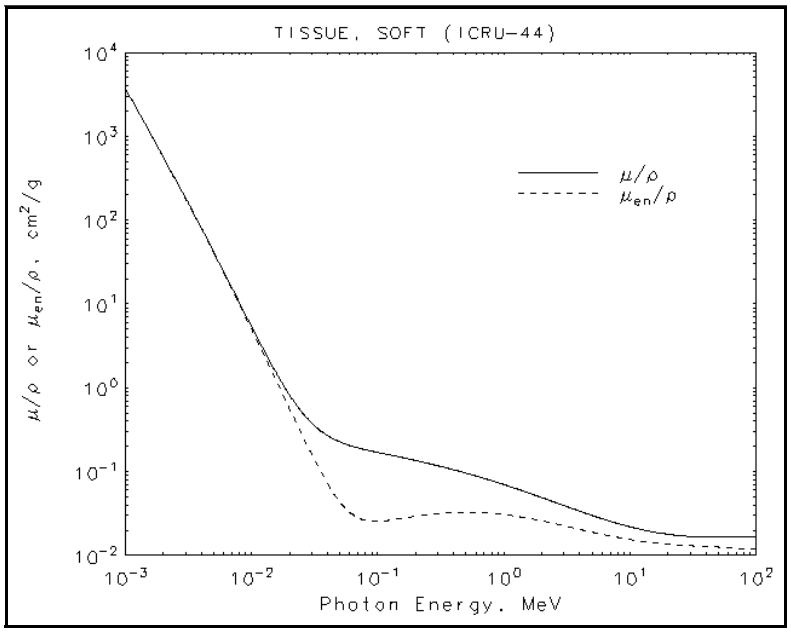

Figure 4.1: Mass energy absorption coefficient for tissue.

In case of a line source the dose rate can be estimated using its total gamma-activity. The estimation further requires knowledge of the source energy, the flux density and the rate of absorption per unit path length at the point of interest. In general, the flux density at a given point around a line source can be calculated as:

$$\Phi = \frac{S_L}{4\pi r} \cdot (|\Theta_1| + |\Theta_2|) \qquad \text{(vi)}$$

where S_L is the line source strength, r is the distance perpendicular to the line source and Θ_1 and Θ_2 are the angles from the point of interest to the two ends of the line source (measured perpendicularly to the line source). In case that the length of the source is large as compared

to the distance *r*, both angles, Θ_1 and Θ_2, can be approximated by $\pi/2$. In this case Equation *(vi)* simplifies to:

$$\Phi = \frac{S_L}{4r}. \qquad \text{(vii)}$$

This photon flux density has to be multiplied by the average energy of the emitted photons in order to obtain the energy flux density, as well as by the mass energy absorption coefficient of tissue (μ_{en}/ρ) in order to determine how much of the energy is actually deposited at the point-of-interest. The dose rate then reads:

$$\frac{dD}{dt}\left[\frac{Sv}{h}\right] = 5.76x10^{-4} \cdot \Phi \cdot E_\gamma \cdot \frac{\mu_{en}}{\rho} \qquad \text{(viii)}$$

where the flux density is in units of $cm^{-1}s^{-1}$, the energy is in MeV and the energy absorption coefficient is in units of cm^2/g.

Finally, if the source is uniformly activated and extended, the dose rate from a semi-infinite planar source is given by the following equation:

$$\frac{dD}{dt}\left[\frac{Sv}{h}\right] = 2.9x10^{-7} \cdot A \cdot E_\gamma \qquad \text{(ix)}$$

where *A* refers to the specific activity in Bq/g and E_γ to the relevant gamma energy in MeV.

4.3.2 Classical ω-Factor Approach

The specific activity *A* in Equation *(ix)* can be estimated from the star density (with a lower threshold of 50 MeV) using the following assumptions [69]

- half of the radionuclides produced in irradiated materials have decay constants between 10 and 10^{-6} min,
- 25% of the radionuclides produced have radioactive daughter products,
- the average number of photons emitted per radioactive decay is 1.5 and
- a hadron “star” is identical to an interaction that produces a radionuclide.

Based on these assumptions the specific activity for iron corresponding to unit star density is 0.12 Bq/g. Assuming furthermore an average photon energy of 800 MeV the dose rate on contact to a semi-infinite uniformly activated plane (per unit star density) according to Equation *(ix)* is $2.8x10^{-8}$ Sv/h. HETC calculations have shown the surface dose rate for an irradiation of 30 days and a decay time of 1 day (a situation often encountered at accelerators) is reduced as compared to infinite irradiation and no cooling by a factor of about 2.8 [69]. This gives a contact dose rate per unit star density of 10^{-8} Sv/h, commonly referred to as ω–factor ω(30,1).

Dose rates at different irradiation and cooling times can be estimated using a formula suggested by Sullivan and Overton [70] which is based on an analytical method for predicting the variation of radioactive buildup and decay. It assumes a continuum of decay constants and is therefore only valid for heavy materials (*e.g.*, iron). According to this approach the dose rate varies with irradiation time *T* and cooling time *t as*

$$\frac{dD}{dt} \sim \ln\left(\frac{T+t}{t}\right). \qquad \text{(x)}$$

Omega factors, ω(30,1), for materials other than iron have been determined by Höfert in [71]. Table 4.1 lists values for a number of different materials.

Table 4.1: Conversion factors ω(30,1) from star density to remanent dose-rate.

Material	ω(30,1) / Sv.h^{-1}/ star.cm^{-3}.s^{-1}
Iron	1.0 x 10^{-8}
Copper	1.0 x 10^{-8}
Stainless steel	1.3 x 10^{-8}
Aluminium	2.0 x 10^{-9}
Lead	1.5 x 10^{-8}
Tungsten	1.1 x 10^{-8}
Normal concrete	3.0 x 10^{-9}
Marble	6.0 x 10^{-10}

4.3.3 Modern ω-Factor Approach

It should be noted that the classical ω-factors do not consider activation by low-energy neutron scattering or thermal neutron capture and the assumptions given in the previous section depend strongly on the shape of the hadron spectra. Furthermore, a threshold of 50 MeV in the definition of star density might not always be the best choice. Instead, a 20 MeV threshold has been shown to be more reasonable [72] as it covers better the whole energy range of spallation reactions and is supported by the fact that it coincides with the upper limit of the energy range for low-energy neutron activation. Finally, as discussed above, the classical ω-factors give the dose after a fixed time of continuous and uniform irradiation and subsequent cooling. Since they do not include any information about the individual radionuclides, the time dependence of the dose is not known. Parameterizations have been proposed [70], but these work only for certain materials and a limited range of irradiation and cooling times.

Thus, a re-evaluation of ω-factors which overcomes most of these deficiencies has been published recently [73]. In particular, ω-factors were calculated with FLUKA for a threshold of 20 MeV and the 19, most common materials at accelerators. The values cover irradiation times between 12 hours and several years as well as cooling times from zero up to 30 years and are also given for a number of typical particle spectra. In addition, ω-factors are not only given for isotope production from high-energy interactions (*i.e.*, those based on star density) but also for low-energy (1-20 MeV) neutron scattering and thermal neutron capture by relating the dose rate to the fluence of the respective particles.

However, some of the general shortcomings of the ω-factor definition are still present in the modern approach, that is, dose rates are given in contact to an uniformly irradiated (and activated) semi-infinite block [74]. This gives a fairly good approximation of the dose rate in contact with a large object, but can lead to a significant overestimation when the activated object is rather small. Thus, the ω-factors can be expected to produce an upper limit in many practical cases. In addition, it is important to note that, by definition, the ω-factors only include the dose due to photons. In particular, the dose due to positrons which annihilate in the material and emit two 511 keV photons is not taken into account. Furthermore, β-emitters are neglected which can be important for the dose in contact with thin objects. Another consequence of this definition is that the ω-factors are not really related to specific activity (Bq/g), but only to the energy emission rate in form of photons (*e.g.*, MeV s^{-1} g^{-1}).

4.3.4 Detailed Simulation

Despite the above explained revisions of the classical approaches, and in view of the rapidly increasing predictive power of models for isotope production the method discussed in the following is more rigorous and general and can be applied to arbitrary irradiation configurations and geometries. It is a two-step approach and has been linked to FLUKA as follows [75]:

In a first step, as soon as a radioactive, residual nucleus is produced by FLUKA its buildup and decay is calculated (taking into account radioactive daughter isotopes) for a certain, irradiation pattern and different requested cooling times [65]. In case of radioactive isomers the relative production rates of these states cannot be predicted by FLUKA. Thus, as a first approximation, equal sharing is assumed between all states. If the isotope or any of its daughters contribute at a given cooling time their properties (mass, charge, position in the geometry, activity, weight) are stored in an external file. In order to limit the file size (especially in case of large geometries) so-called biasing techniques can be used to suppress excessive storing of frequently produced isotopes. In addition, the activities at the various cooling times are only saved once, at the first appearance of the isotope.

In a second, pure electromagnetic FLUKA simulation the information on the produced isotopes is read from the file and decay photons, electrons, or positrons are generated. For this purpose detailed information on gamma energies, electron and positron energy spectra as well as on branching ratios is obtained from a data base [76, 77]. Particles are assumed to be emitted isotropically, with their energies sampled according to their corresponding intensities and/or energy spectra. The electromagnetic cascade is calculated and the dose equivalent rate can be scored at any point-of-interest or in a three-dimensional mesh covering the geometry.

CHAPTER 4 Simulation Methods

5 Benchmark Measurements

Estimates of the activation of materials in stray radiation fields at high-energy accelerators and of the resulting residual dose rates are an important input to the material selection and design of beam-line components and detectors. Beamline components at high-energy hadron colliders, such as the Large Hadron Collider, can become highly activated due to various beam loss mechanisms: beam-beam interactions at the collision points, interactions of the beam halo with small apertures or interactions of the beam with residual gas molecules in the vacuum pipe. The activation of components is an important radiation safety concern not only during the operation of the machine and possible maintenance but also later for de-commissioning and final disposal of the activated materials. In all cases accurate calculations of the radionuclide inventory and remanent dose rates are required in order to avoid either excessive costs (*e.g.,* for waste disposal) caused by overly conservative estimates or an unjustified exposure of personnel and environment during operation due to underestimates in the design phase.

Many quantities essential in the design and operational phase of a high-energy accelerator (*e.g.,* dose to components and dose equivalent to personnel by prompt radiation) can be predicted with rather good accuracy using modern Monte-Carlo codes. However, estimates of specific activities and resulting residual dose rates - although equally important - are usually far less reliable and therefore of particular interest for benchmark studies.

Several experiments have already been performed for both, electron (see [79, 80]) and hadron accelerators (see, *e.g.*, [81-87]). However, most of these studies concentrate either on induced activity or on remanent dose rates although both are closely linked to each other. Due to the complexity of the involved physical processes and analysis methods it is often difficult to attribute disagreements between calculated and measured results to their respective source of uncertainty.

The study described in this chapter is an attempt to overcome some of the shortcomings of earlier studies by benchmarking at the same time FLUKA predictions for isotope production and remanent dose rates with detailed measurements. In particular, remanent dose rates are calculated by an explicit simulation of the transport of the radiation from the radioactive decay (two-step approach, see Section 4.3.4) [88, 75].

5.1 The Irradiation Experiment

The experiment was carried out at the CERN-EU High-Energy Reference Field (CERF) facility [89] which is installed in one of the secondary beam lines (H6) from the Super Proton Synchrotron (SPS) at CERN (see also Figure 2.1). At this

facility a cylindrical copper target (7 cm in diameter, 50 cm in length) is intercepting a positively charged hadron beam with a momentum of 120 GeV/*c* consisting of protons (34.8%), pions (60.7%) and kaons (4.5%). The copper target is surrounded by a concrete enclosure of 80 cm thickness (see Figure 5.1). The CERF facility serves mainly for detector test and calibration

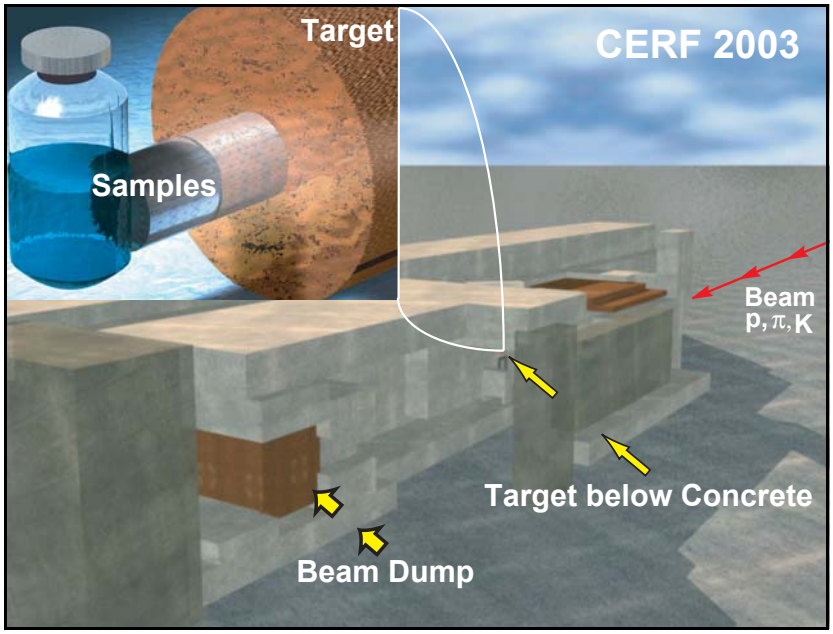

Figure 5.1: Axonometric view of the CERF facility. In the graphical representation the side shield is removed to show the inside of the irradiation cave with the copper target set-up.

purposes and thus provides instrumentation for accurately recording the beam properties (intensity and profile). As the latter is essential for benchmark experiments the facility is well-suited for the present study of induced radioactivity. An air-filled Precision Ionisation Chamber (PIC) at atmospheric pressure, placed in the beam just upstream of the copper target, monitors the intensity of the beam. One PIC-count corresponds to 2.3×10^4 ±10% particles impinging on the target [89].

Table 5.1: Density and chemical composition (in percent by weight) of the metallic samples: copper (Cu), stainless steel (SS) and iron (Fe). The materials carry the CERN catalogue identification numbers 44.09.47.520.1 (Cu), 44.57.10.420.4 (SS) and 44.50.60.120.0 (Fe).

Sample	Cu		SS		Fe	
Composition (% weight)	Cu	99.9919	Fe	66.895	Fe	99.91
	P	0.003	Cr	19.0	Mn	0.06
	S	0.0018	Ni	11.0	C	0.01
	O	0.001	Mn	2.0	P	0.01
	Pb	0.001	Si	1.0	S	0.01
	Bi	0.001	P	0.045		
	Zn	10^{-4}	C	0.03		
	Cd	10^{-4}	S	0.03		
	Hg	10^{-4}				
Density (g/cm^3)	8.9		7.8		7.86	

For the activation and dose rate studies, cylindrical samples of iron, stainless steel, copper, aluminium, boron nitride and carbon composite, as well as a bottle with demineralized water were attached to the centre of the downstream face of the copper target (see Figure 5.1) and irradiated by the secondary radiation field created in the target. The solid materials were

obtained from the CERN internal store and machined to a cylindrical shape of 2 cm diameter and 2 cm height. The demineralized water probe had a volume of 15 ml and was irradiated in a glass bottle. The elemental composition and densities of the samples were taken into account in this study as accurately as possible and are given in Tables 5.1 and 5.2. The former were obtained from the corresponding material specifications.

Table 5.2: Density and chemical composition (in percent by weight) of the aluminium (Al), boron nitride (BN) and carbon composite (CC) samples. The aluminium sample carries the CERN catalogue identification number 44.02.07.020.8.

Sample	Al		BN		CC	
Composition (% weight)	Al	95.95	BN	99.34	C	99.999752
	Si	1.1	O	0.4	Ca	8.10×10^{-5}
	Mg	0.9	B_2O_3	0.2	P	6.75×10^{-5}
	Mn	0.7	Ca	0.04	Na	4.50×10^{-5}
	Fe	0.5	C	0.02	Si	2.70×10^{-5}
	Cr	0.35			Fe	2.20×10^{-5}
	Ti	0.2			Al	4.50×10^{-6}
	Zn	0.2				
	Cu	0.1				
Density (g/cm^3)	2.7		1.91		1.46	

In general, the samples were exposed parasitically to the experiments of the main users of the facility with exposure times of typically 8 hours and a total number of beam particles ranging from 1.8×10^{11} to 2.5×10^{11}.

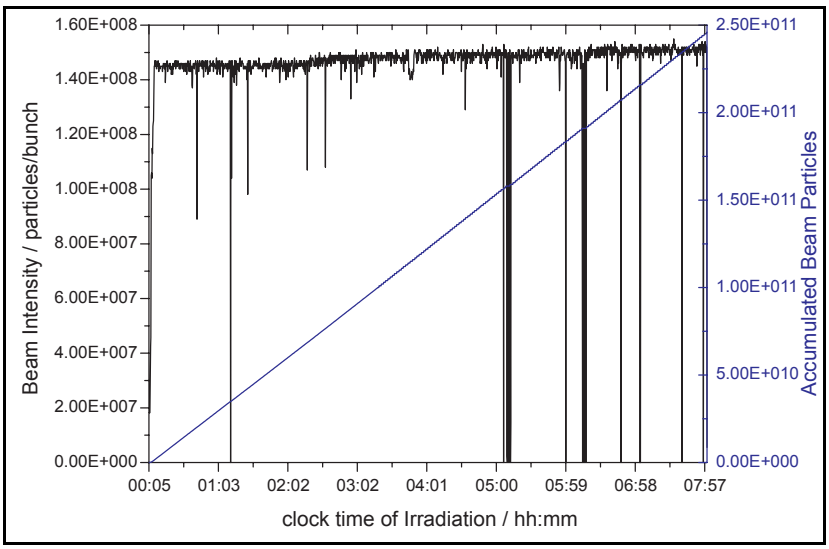

Figure 5.2: Example of a beam intensity profile (left scale) and accumulated number of beam particles (right scale) as function of the irradiation time.

Figure 5.2 shows a typical beam intensity profile recorded during eight hours of irradiation. The lateral beam profile was measured with a multi-wire proportional chamber (see example shown in Figure 5.3).

After the irradiation two gamma-spectrometry measurements were performed for each sample: a short analysis immediately after the sample had been taken out and a longer analysis several days later (several hours later for CC, BN and water). A summary of the irradiation and cooling times for the various samples is given in Table 5.3. It should be noted that the listed cooling times comprise the duration of the measurement and thus refer to the end of the respective spectrometry analysis. In case of the short cooling time, the time between the end of the

irradiation and the start of the measurement was usually of the order of 30 to 45 minutes, hence also measurements of rather short-lived isotopes were possible.

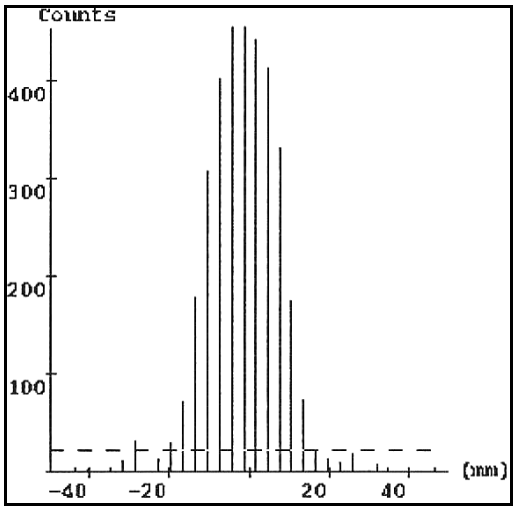

Figure 5.3: Example of a beam profile as measured during one of the irradiations.

Table 5.3: Summary of irradiation times (t_{irr}), cooling times (t_{cool}) and spectrometry analysis durations ($t_{analysis}$) for the various samples.

Sample	t_{irr}	t_{cool1}	$t_{analysis1}$	t_{cool2}	$t_{analysis2}$
Cu	2h34’	3h45’	2h47’	29d21h31’	24h00’
SS	6h52’	3h28’	2h48’	9d09h30’	5h52’
Fe	1h52’	3h18’	2h47’	13d13h15’	19h29’
Al	3h19’	3h26’	2h47’	10d22h50’	21h11’
BN	6h57’	2h20’	1h30’	1d09h41’	23h20’
CC	6h52’	4h14’	3h00’	15h17’	8h19’
H_2O	7h18’			1d00h16’	22h50’

5.2 Induced Activity Benchmark

As already mentioned, the samples were attached to the downstream end of a 50 cm long copper target, centred with the beam axis. At this location, particle energy spectra are characterized by a significant high-energy component of the order of several GeV and are typical for particle-loss regions at accelerators (collimators, dumps, *etc.*)

The specific activity induced in the samples was measured by gamma-spectrometry and simulated with detailed Monte-Carlo calculations using the FLUKA code. Emphasis was put on reducing uncertainties in both measurements and simulations in order to allow for an accurate benchmark of the FLUKA code. This included low-level measurements of gamma lines, appropriate treatment of the decay chains of isotopes in the gamma-spectrometry and in the simulations, various efficiency corrections in the spectrometry, as well as detailed simulations of residual nuclei production with low statistical uncertainties.

5.2.1 Data Analysis

Gamma-spectrometry

The gamma rays from the radioisotopes in the different samples were measured with a very low background coaxial High-Precision Germanium (HPGe) detector by Canberra (90 cm^3 sensitive volume, 20 % relative efficiency at 1.33 MeV). Data acquisition and analysis were carried out using the Genie-2000 (Ver. 2.0) spectrometry software and the PROcount-2000

counting procedure software[1] which are a comprehensive environment for data acquisition, display and analysis. These software packages include a set of advanced spectrum analysis algorithms, providing, *e.g.,* nuclide identification, interference correction, weighted mean activity, background subtraction and efficiency correction. High accuracy of the measurements is assured by precise energy and efficiency calibration combined with regular quality assurance in order to maintain the traceability of the qualitative and the quantitative analysis. This is performed by monitoring various parameters, *e.g.,* peak energy location and shape for the qualitative case, or efficiency and background for the quantitative case. The software package also comprises well-developed methods for peak identification and allows one to use standard or user-generated nuclide libraries. In addition, the software is capable of resolving overlapping peaks into individual components.

For this study (see also [88, 75]), an isotope library was created based on the chemical composition of the different samples and containing all isotopes, which could possibly be produced by the irradiation. It should be noted that in case certain isotopes were missing in the library, the analysis would have listed them as “unidentified peaks” which were then cross-checked for each measurement. Despite the complexity and quality, but due to integration, fitting or library ambiguities of the analysis package, for some isotopes certain means of manual analysis, combined with the automatic procedures of the package, turned out to be the best method to determine the correct specific activity.

In order to achieve most accurate results two additional analysis techniques were applied. The first one includes the correction for the decay of isotopes with gamma-emitting daughters, frequently referred to as “Parent-Daughter Correction”. This correction is important, *e.g.,* for those isotopes for which the buildup from metastable isotopes plays a significant role. The second technique is an efficiency calibration taking into account geometrical effects and self-absorption in the sample. It includes a detailed modelling of the dimensions and materials of the sample[2] and is especially important for isotopes that emit low-energy gamma lines.

The final step in the analysis was to calculate the specific activity of each isotope for the end of the corresponding measurement time, which was then compared to the simulation results.

Tritium Measurements

After re-filling the activated demineralized water into new vials the tritium activity was determined using a liquid scintillation counter (Packard TRI-CARB 3170TR/SL[3]), measuring a mixture consisting of 8 ml of water to be analysed and 12 ml of a so-called liquid scintillation cocktail (Packard Ultima Gold LLT[3]). In general, for high precision measurements distillation is recommended as other radionuclides present in the sample (*e.g.,* ^{22}Na) may significantly influence the result for tritium. However, since possible impurities were kept at a minimum and the experiment was performed in well-controlled conditions the sample was not distilled. In particular, possible interference from other radionuclides to the tritium pulse-height window, of which the liquid scintillation counter would have alerted the user, turned out to be negligible.

5.2.2 The FLUKA Calculations

The concentration of the different radionuclides in the samples was calculated with FLUKA (see Section 4.2.3) based on a detailed description of the experimental setup. It contained the copper target, the samples as well as the concrete roof, floor and side walls of the beam-line

1. CANBERRA/EURISYS S.A., 4 Avenue des Frenes, F-78067 St Quentin en Yvelines Cedex, France.
2. LabSOCS, Canberra software package V 4.1.
3. PerkinElmer Life Science, Imperiastraat 8, B-1930 Zaventem, Belgium.

shielding at lateral distances to the beam axis of 113 cm, 127 cm, 61 cm and 102 cm, respectively. Only 30 cm thick slices were considered for the concrete enclosures in order to account for particle back-scattering. In addition, a 80 × 80 × 40 cm^3 concrete block standing on the beam-line floor just downstream of the target was included. The beam was assumed to hit the centre of the target with a Gaussian profile of 2.1 cm and 2.6 cm full width at half maximum (FWHM) in lateral directions.

The origin of the coordinate frame of the FLUKA geometry was chosen to be in the centre of the front face of the copper target, the *z*-axis coinciding with the beam axis and the *x*-axis pointing up. The elemental compositions of the samples were defined in the simulations as given in Tables 5.1 and 5.2. The full hadronic cascade was simulated in the target, the samples and in the concrete block, including particles back-scattered from the walls. Neutrons were transported down to thermal energies; for all other hadrons a threshold of 1 keV was used. The simulation of the electromagnetic cascade was not taken into account.

In order to increase the statistical significance of the results for the samples importance biasing was applied to the regions containing the samples. Separate simulations were performed for proton and pion beams and their results were combined according to the actual beam composition. At the location of the samples, particle energy spectra were obtained for neutrons, protons and pions and are shown - for the case of the proton beam - in Figure 5.4.

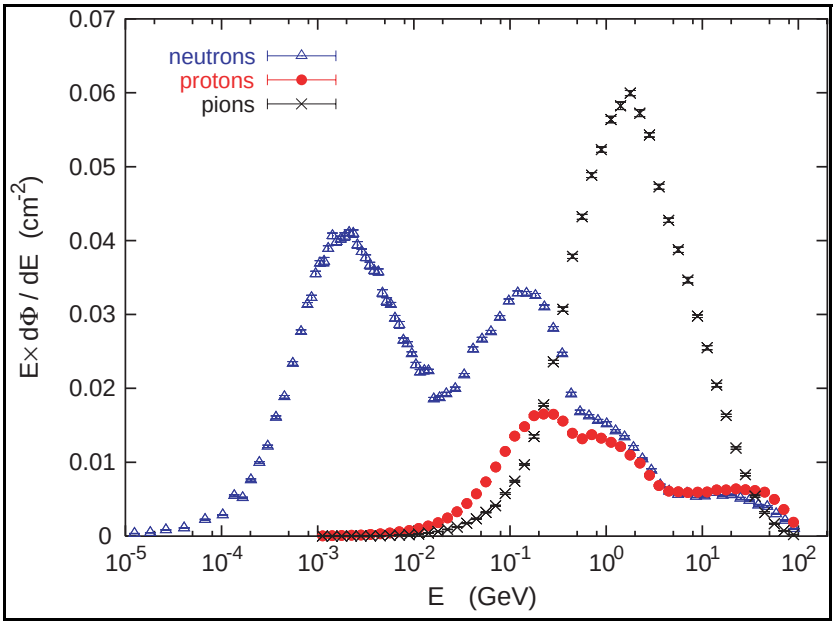

Figure 5.4: Energy spectra of neutron, protons and charged pions in the samples (normalized per primary beam particle).

The total yield of radionuclides and the yield produced by low-energy neutrons (*i.e.*, below the threshold for the multi-group treatment, $E < 19.6$ MeV) were scored separately for all samples and the results were written into output files. These data files were then post-processed [67], taking into account the decay chains and buildup of isotopes, as well as the correct intensity profile of the experiment (*e.g.,* Figure 5.2), and specific activities were calculated.

5.2.3 Results

In the following the calculated and measured specific activities are compared for each sample, whereby the results for the two cooling times are presented in separate tables. As mentioned above, listed cooling times refer to the end of the respective measurement. Thus, the time between the end of the irradiation and the beginning of the first measurement was much shorter so that isotopes with half-lives of less than one hour could be identified. In addition, the tables

give the ratio between simulated and measured activities, as well as the contribution of low-energy neutron interactions to the total isotope production yield. The isotopes listed are only those, which were identified by the experiment. In the simulation usually more isotopes are retrieved, which, however, cannot be detected by the measurement. Reasons for the latter are:

- The activities are below the "Minimal Detectable Activity" (MDA).[1]
- The yield of gamma lines in the detectable range is not significant.
- Gamma lines only contribute to the 511 keV peak, which cannot be separated for the different isotopes.
- Many isotopes exist with the same energy lines and comparable half-lives.

The stated experimental errors contain both the statistical and the systematic uncertainties of the spectrometry analysis. In case of the simulations the errors represent statistical uncertainties only. Uncertainties in the half-lives used to follow the radioactive decay chains were found to have a negligible influence on the results.

Aluminium

Table 5.4 shows results for the isotopes detected in the aluminium sample after the short cooling time. The two isotopes ^{27}Mg and ^{56}Mn are relatively well reproduced by FLUKA. On the other hand, ^{44}Sc is most likely underestimated by the experiment since the measured activity is close to the MDA and a possible contribution of ^{44m}Sc could not be resolved in the analysis of the spectrum.

Table 5.4: Comparison of calculated and measured specific activities in the aluminium sample for a cooling time of 3h26'. Furthermore, their ratio as well as the contribution of low-energy neutron interactions to the total isotope production, flow, is given. Note that errors are quoted in percent.

Isotope	$t_{1/2}$	FLUKA (Bq/g) (%)	Experiment (Bq/g) (%)	Ratio	f_{low}
^{24}Na	15.0 h	98.8 ± 0.9	144.0 ± 4.0	0.69	0.45
^{27}Mg	9.5 m	0.000142 ± 1.6	0.000111 ± 14.8	1.28	0.76
^{44}Sc	3.9 h	1.59 ± 12.2	0.723 ± 25.6	2.20	-
^{56}Mn	2.6 h	2.54 ± 32.0	2.07 ± 9.0	1.22	0.82

The specific activity of ^{24}Na seems to be underestimated by FLUKA, which is supported by the result of folding energy spectra in the sample with experimental cross-sections (see Figure 5.5). The latter results in a specific activity of 147 Bq/g, which is in good agreement with the measurement (144 Bq/g). Figure 5.5 also shows the partial cross-section for the production of ^{24}Na in proton-aluminium interactions as calculated by FLUKA, which clearly explains the too low value of 98.8 Bq/g obtained in the simulation.

1. The MDA is computed by the analysis software following the Currie method [92] using a 95% confidence level for the detection limits.

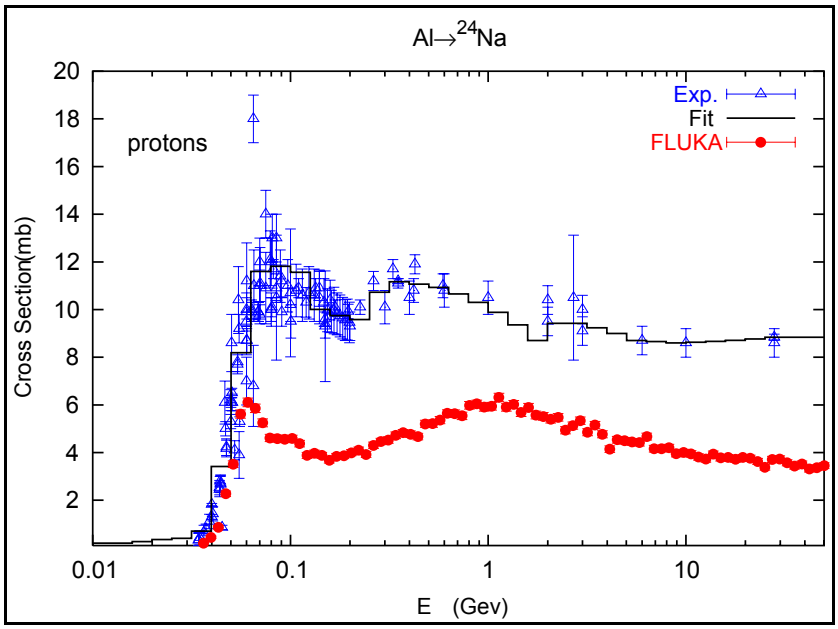

Figure 5.5: Cross-section for the production of ^{24}Na in interactions of protons with aluminium nuclei. Experimental data (see [93] and references therein) are shown together with a fit and with the predictions by the FLUKA code.

Nine isotopes could be identified for the longer cooling time (10d22h50') and the results are shown in Table 5.5. Uncertainties in the elemental composition of the sample (taken from the CERN specifications) might contribute to the overestimation of the measured activity by a factor of about 1.6 as compared to the simulations.

Table 5.5: As in Table 5.4, here for a cooling time of 10d22h50'.

Isotope	$t_{1/2}$	FLUKA (Bq/g) (%)	Experiment (Bq/g) (%)	Ratio	f_{low}
^{7}Be	53.3 d	0.334 ± 2.7	0.712 ± 20.0	0.48	-
^{22}Na	2.6 y	0.0707 ± 1.3	0.0892 ± 10.2	0.79	-
^{44}Sc	3.9 h	0.0114 ± 12.1	0.0069 ± 80.9	1.65	-
^{44m}Sc	58.6 h	0.0107 ± 12.1	0.00727 ± 80.9	1.48	-
^{47}Sc	80.3 h	0.0214 ± 13.7	0.0131 ± 43.8	1.64	0.03
^{48}V	16.0 d	0.0448 ± 10.8	0.0269 ± 12.2	1.66	-
^{51}Cr	27.7 d	0.0780 ± 9.1	0.0472 ± 40.9	1.65	0.03
^{52}Mn	5.6 d	0.0234 ± 11.9	0.0204 ± 13.5	1.15	-
^{54}Mn	312.1 d	0.0112 ± 7.5	0.0178 ± 21.7	0.63	0.13

Stainless Steel and Iron

The results for stainless steel are given in Tables 5.6 and 5.7. The activities of most of the heavier isotopes (A > 43) are remarkably well reproduced by FLUKA. Except for a few cases, the agreement of calculated and measured values is within the uncertainties of the measurements. Isotopes for which differences seem to be systematic are ^{51}Cr (see also discussion below), ^{52m}Mn (large experimental error and assumption concerning metastable states in post-processing of FLUKA results) and ^{54}Mn (in particular the measurement at the

large cooling time). The activities of light isotopes are underestimated as expected from the deficiencies in the treatment of fragmentation in FLUKA (see Section 4.1.4).

Table 5.6: Comparison of calculated and measured specific activity in the stainless steel sample for a cooling time of 3h28'. Furthermore, their ratio as well as the contribution of low-energy neutron interactions to the total isotope production, f_{low}, is given. Note that errors are quoted in percent.

Isotope	$t_{1/2}$	FLUKA (Bq/g) (%)	Experiment (Bq/g) (%)	Ratio	f_{low}
^{24}Na	15.0 h	5.25 ± 6.0	19.8 ± 4.7	0.27	-
^{28}Mg	20.9 h	0.0968 ± 47.5	2.04 ± 35.0	0.05	-
^{28}Al	2.2 m	0.097 ± 47.5	2.04 ± 35.5	0.05	-
^{38}S	2.8 h	0.0848 ± 69.4	0.439 ± 41.9	0.19	-
^{34m}Cl	32.0 m	0.227 ± 7.8	0.239 ± 42.2	0.95	-
^{38}Cl	37.2 m	0.583 ± 14.0	1.86 ± 13.4	0.31	-
^{39}Cl	55.6 m	0.43 ± 18.3	0.979 ± 16.7	0.44	-
^{41}Ar	1.8 h	1.87 ± 13.4	6.22 ± 7.3	0.30	-
^{42}K	12.4 h	23.9 ± 4.9	35.1 ± 8.6	0.68	-
^{43}K	22.3 h	4.84 ± 6.5	9.56 ± 8.8	0.51	-
^{43}Sc	3.9 h	55.0 ± 2.2	61.5 ± 15.3	0.89	-
^{44}Sc	3.9 h	120.0 ± 1.4	122. ± 5.9	0.98	-
^{44m}Sc	58.6 h	20.7 ± 1.6	19.6 ± 13.4	1.05	-
^{47}Sc	80.3 h	7.86 ± 2.4	10.7 ± 26.5	0.74	-
^{48}Sc	43.7 h	3.46 ± 7.1	3.89 ± 38.7	0.89	-
^{48}V	16.0 d	10.4 ± 1.6	10.4 ± 23.4	1.00	-
^{48}Cr	21.6 h	3.95 ± 7.4	5.15 ± 10.6	0.77	-
^{49}Cr	42.3 m	8.3 ± 2.3	8.88 ± 13.1	0.94	-
^{51}Cr	27.7 d	15.9 ± 0.7	24.1 ± 20.8	0.66	0.05
^{52}Mn	5.6 d	13.5 ± 1.6	15.6 ± 9.0	0.87	-
^{52m}Mn	21.1 m	0.401 ± 1.7	7.35 ± 58.4	0.06	-
^{54}Mn	312.1 d	1.15 ± 0.9	1.25 ± 92.5	0.92	0.07
^{56}Mn	2.6 h	99.0 ± 2.9	99.9 ± 4.5	0.99	0.64
^{52}Fe	8.3 h	5.55 ± 8.0	6.66 ± 63.2	0.83	-
^{55}Co	17.5 h	11.8 ± 5.1	12.6 ± 11.0	0.93	-
^{57}Ni	35.6 h	21.8 ± 2.6	19.4 ± 7.1	1.12	0.02

Table 5.7: As in Table 5.6, here for a cooling time of 9d9h30'.

Isotope	$t_{1/2}$	FLUKA (Bq/g) (%)	Experiment (Bq/g) (%)	Ratio	f_{low}
^{7}Be	53.3 d	0.0411 ± 9.7	0.468 ± 29.7	0.09	-
^{44}Sc	3.9 h	1.58 ± 1.6	1.35 ± 6.3	1.17	-
^{44m}Sc	58.6 h	1.49 ± 1.6	1.44 ± 11.1	1.04	-
^{46}Sc	83.8 d	0.557 ± 1.5	0.771 ± 5.9	0.72	-
^{47}Sc	80.3 h	1.18 ± 2.5	1.63 ± 13.7	0.72	-
^{48}Sc	43.7 h	0.102 ± 7.1	0.0891 ± 34.0	1.14	-
^{48}V	16.0 d	7.14 ± 1.6	5.88 ± 4.0	1.21	-
^{51}Cr	27.7 d	12.6 ± 0.7	16.7 ± 9.8	0.75	0.046
^{52}Mn	5.6 d	4.41 ± 1.6	4.43 ± 3.7	0.99	-
^{54}Mn	312.1 d	1.12 ± 0.9	1.34 ± 6.4	0.84	0.075
^{56}Co	77.3 d	0.656 ± 2.0	0.549 ± 6.0	1.19	-
^{57}Co	271.8 d	0.422 ± 1.6	0.489 ± 15.1	0.86	0.13
^{58}Co	70.8 d	0.837 ± 0.9	0.858 ± 8.2	0.98	0.79
^{57}Ni	35.6 h	0.288 ± 2.6	0.25 ± 19.6	1.15	0.02

Of the identified isotopes only ^{56}Mn and ^{58}Co are produced to a large fraction in low-energy neutron interactions, by (n,p) reactions on ^{56}Fe in case of ^{56}Mn and by (n,d) reactions on ^{59}Ni for the latter isotope.

Tables 5.8 and 5.9 show the results for the iron sample. As for stainless steel, FLUKA predictions and experimental values agree within the statistical uncertainty of the measurement for most of the heavier isotopes. For the longer cooling time, the activity of ^{47}Sc seems to be overestimated by the measurement due to a possible contribution by ^{47}V as predicted by the

FLUKA simulation. However, too few lines were detected in the spectra in order to resolve the contribution of ^{47}V separately.

Table 5.8: Comparison of calculated and measured specific activity in the iron sample for a cooling time of 3h18'. Furthermore, their ratio as well as the contribution of low-energy neutron interactions to the total isotope production, f_{low}, is given. Note that errors are quoted in percent.

Isotope	$t_{1/2}$	FLUKA (Bq/g) (%)	Experiment (Bq/g) (%)	Ratio	f_{low}
^{24}Na	15.0 h	0.941 ± 3.9	3.82 ± 10.2	0.25	-
^{34m}Cl	32.0 m	0.168 ± 5.4	0.187 ± 40.9	0.90	-
^{38}Cl	37.2 m	0.397 ± 6.6	0.574 ± 15.4	0.69	-
^{39}Cl	55.6 m	0.235 ± 17.7	0.522 ± 23.4	0.45	-
^{41}Ar	1.8 h	0.603 ± 16.1	2.11 ± 32.9	0.29	-
^{42}K	12.4 h	3.99 ± 3.4	8.85 ± 17.4	0.45	-
^{43}K	22.3 h	0.792 ± 9.3	1.51 ± 74.1	0.53	-
^{43}Sc	3.9 h	14.1 ± 2.8	17.9 ± 33.3	0.79	-
^{44}Sc	3.9 h	28.3 ± 1.2	27.8 ± 8.6	1.02	-
^{44m}Sc	58.6 h	3.49 ± 1.3	3.27 ± 14.4	1.07	-
^{47}Sc	80.3 h	1.11 ± 3.0	1.78 ± 28.8	0.63	-
^{48}Sc	43.7 h	0.481 ± 4.8	0.403 ± 51.3	1.19	-
^{48}V	16.0 d	1.68 ± 1.1	2.00 ± 14.7	0.84	-
^{48}Cr	21.6 h	0.79 ± 8.8	0.963 ± 25.7	0.82	-
^{49}Cr	42.3 m	5.23 ± 3.0	4.73 ± 12.1	1.10	-
^{52}Mn	5.6 d	2.87 ± 1.2	3.14 ± 11.3	0.91	-
^{56}Mn	2.6 h	43.1 ± 1.7	40.7 ± 5.0	1.06	0.6
^{52}Fe	8.3 h	1.37 ± 5.0	1.83 ± 55.1	0.75	-
^{55}Co	17.5 h	1.12 ± 7.9	1.42 ± 41.6	0.79	-

Table 5.9: As in Table 5.8, here for a cooling time of 13d13h15'.

Isotope	$t_{1/2}$	FLUKA (Bq/g) (%)	Experiment (Bq/g) (%)	Ratio	f_{low}
^{44}Sc	3.9 h	0.0821 ± 1.3	0.08 ± 20.4	1.03	-
^{46}Sc	83.8 d	0.0789 ± 1.6	0.12 ± 18.1	0.66	-
^{47}Sc	80.3 h	0.0703 ± 3.1	0.091 ± 30.9	0.77	-
^{44m}Sc	58.6 h	0.0774 ± 1.3	0.0774 ± 22.5	1.00	-
^{48}V	16.0 d	0.966 ± 1.1	0.811 ± 17.4	1.19	-
^{51}Cr	27.7 d	1.54 ± 1.0	1.95 ± 23.6	0.79	0.01
^{52}Mn	5.6 d	0.561 ± 1.1	0.567 ± 17.9	0.99	-
^{54}Mn	312.1 d	0.26 ± 0.8	0.299 ± 18.9	0.87	0.07

As already demonstrated for the production of ^{24}Na in aluminium, comparing experimental cross-sections [94] for particular isotopes with those predicted by FLUKA, might help for a more thorough understanding of observed differences. However, it is not conclusive in all cases, especially if experimental cross-section data are inconsistent. For example, the measured and calculated specific activities of ^{48}V are in good agreement whereas Figure 5.6 clearly shows discrepancies in the cross-sections for ^{48}V production in proton-induced interactions on iron. At energies above about 0.4 GeV, an energy range which is characterized by a significant fluence of protons and pions at the location of the sample (see Figure 5.4), measured and simulated values do not agree and seem to be overestimated by FLUKA.

However, data also scatter significantly and are too scarce at higher energies in order to allow to draw definite conclusions on the reliability of the FLUKA predictions. At low energies, *i.e.*, close to the production threshold (E<0.1 GeV), the experimental data seem to be well-reproduced by the simulations. The step in the FLUKA cross-sections at approximately 3.5 GeV indicates the transition between different hadronic interaction models (below 3.5 GeV: PEANUT, above 3.5 GeV: resonance production and decay model and DPM).

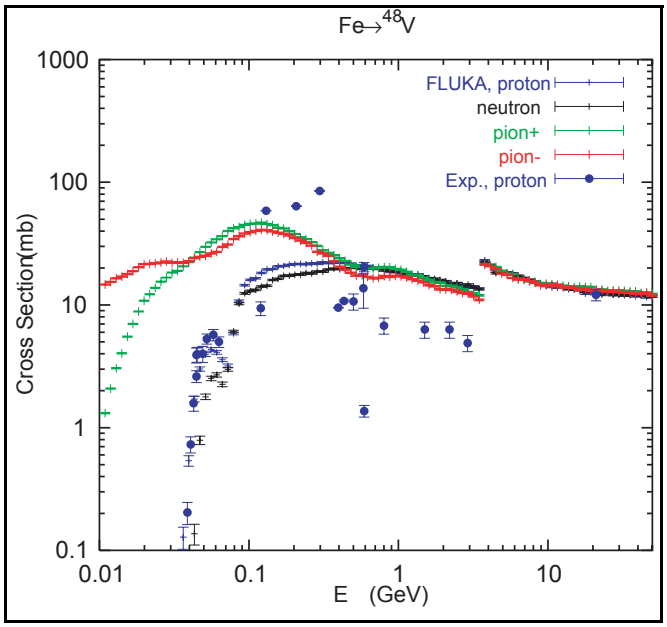

Figure 5.6: Cross-section for the production of ^{48}V in interactions of protons, neutrons and charged pions with iron nuclei. Experimental data (circles) are shown together with the predictions by the FLUKA code (crosses). Experimental data are only available for proton-induced reactions [94].

As an example for an isotope of relatively small mass, Figure 5.7 shows the partial cross-section for the production of ^{24}Na. Indeed, the experimental data are underestimated by the simulations due to the missing multifragmentation model.

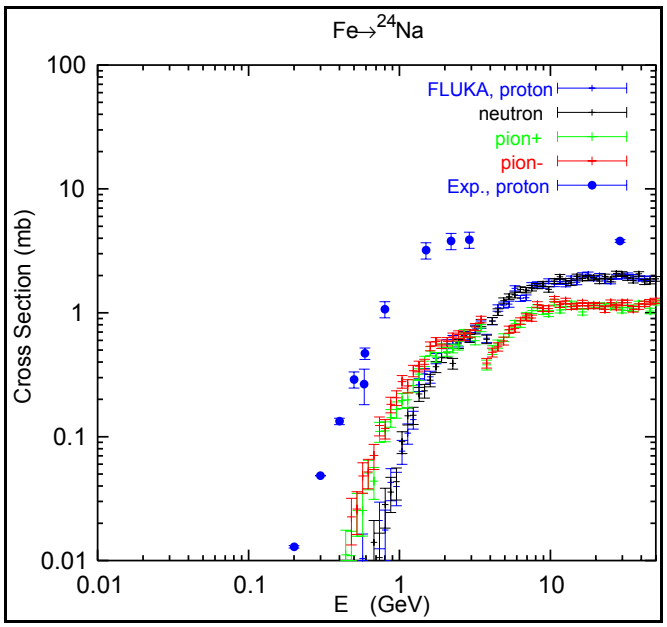

Figure 5.7: Cross-section for the production of ^{24}Na in interactions of protons, neutrons and charged pions with iron nuclei. Experimental data (circles) are shown together with the predictions by the FLUKA code (crosses). Experimental data are only available for proton-induced reactions [94].

In the case of ^{42}K the situation is not less obvious. The specific activities measured for both samples, stainless steel and iron, are underestimated by roughly a factor of two. The cross-

sections shown in Figure 5.8 exhibit a similar trend only at low-energy whereas the data seem to be relatively well-described at high-energy.

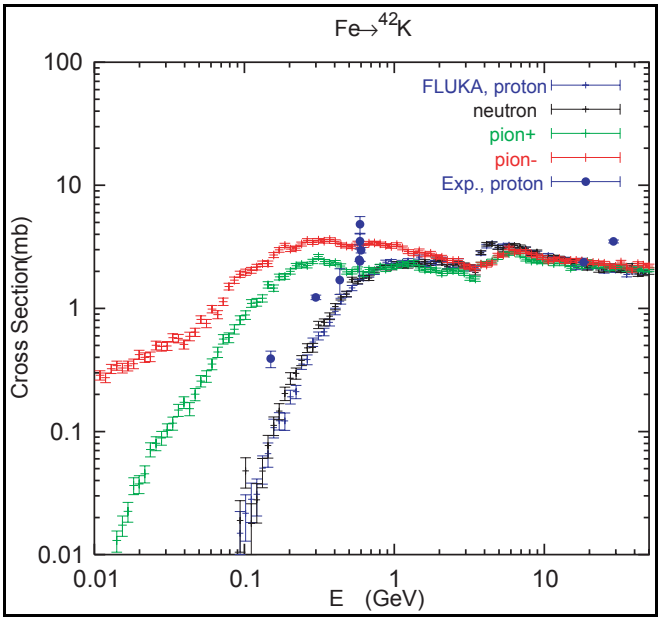

Figure 5.8: Cross-section for the production of ^{42}K in interactions of protons, neutrons and charged pions with iron nuclei. Experimental data (circles) are shown together with the predictions by the FLUKA code (crosses). Experimental data are only available for proton-induced reactions [94].

No experimental data are available in the energy range between 1 and 10 GeV, which is important for this study. Thus, if the differences between measured and calculated specific activities are systematic they most likely originate from this energy region.

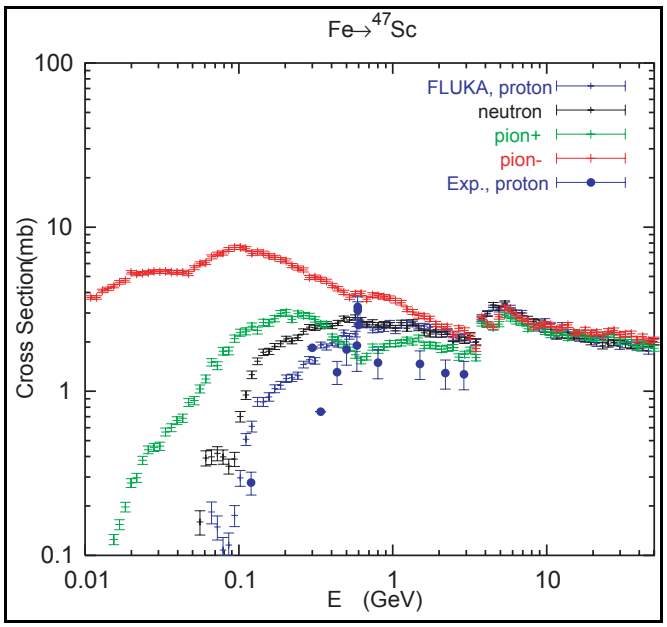

Figure 5.9: Cross-section for the production of ^{47}Sc in interactions of protons, neutrons and charged pions with iron nuclei. Experimental data (circles) are shown together with the predictions by the FLUKA code (crosses). Experimental data are only available for proton-induced reactions [94].

In order to further illustrate the difficulties in confirming the conclusions of the activation measurements with isotope production cross-sections the latter is shown for ^{47}Sc in Figure 5.9. In this case the activation data is underestimated, whereas the cross-sections in fact are overestimated.

Similarly, the measured specific activities for ^{51}Cr are underestimated by FLUKA by about 20-30%. The cross-section for proton-induced reactions, however, is predicted to be larger by FLUKA than indicated by the experimental data above 0.1 GeV. On the other hand, at lower energies the FLUKA results follow nicely the numerous data.

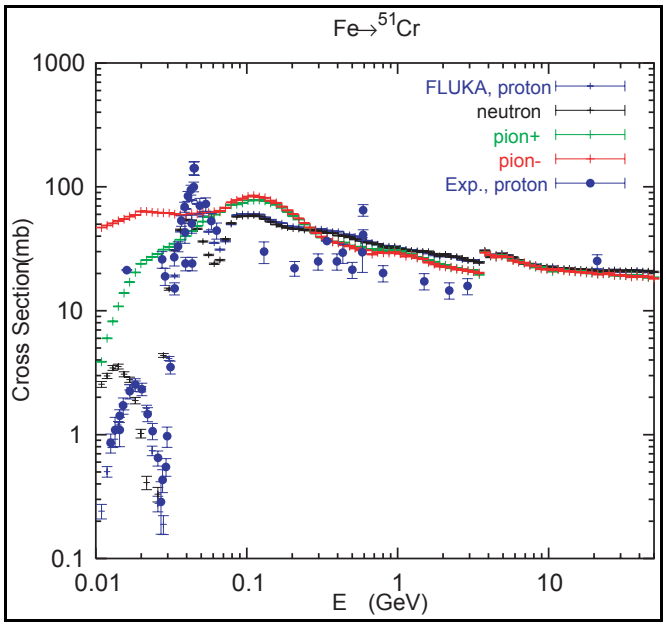

Figure 5.10: Cross-section for the production of ^{51}Cr in interactions of protons, neutrons and charged pions with iron nuclei. Experimental data (circles) are shown together with the predictions by the FLUKA code (crosses). Experimental data are only available for proton-induced reactions [94].

Copper

The specific activities in the copper sample calculated with FLUKA are systematically lower than the measured values. The results together with the ratios of calculated and measured values are given in Tables 5.10 and 5.11. The reason for this discrepancy is still under investigation but it either could be due to uncertainties in the elemental composition of the sample, or due to a possible misplacement of the target with respect to the axis of the beam. In order to resolve the first question a chemical analysis of the sample is foreseen.

The target alignment will be verified during an upcoming CERF-experiment. In any case, it is planned to irradiate copper again which should clarify the situation. Finally, except for ^{64}Cu and ^{60}Co, non of the identified isotopes is produced in interactions of low-energy neutrons.

Table 5.10: Comparison of calculated and measured specific activity in the copper sample for a cooling time of 3h45'. Furthermore, their ratio as well as the contribution of low-energy neutron interactions to the total isotope production, f_{low}, is given. Note that errors are quoted in percent.

Isotope	$t_{1/2}$	FLUKA (Bq/g) (%)	Experiment (Bq/g) (%)	Ratio	f_{low}
^{24}Na	15.0 h	0.268 ± 5.9	2.04 ± 14.5	0.13	-
^{38}Cl	37.2 m	0.0873 ± 9.9	0.269 ± 37.5	0.33	-
^{39}Cl	55.6 m	0.0783 ± 11.4	1.13 ± 32.1	0.07	-
^{41}Ar	1.8 h	0.199 ± 15.2	1.17 ± 22.8	0.17	-
^{42}K	12.4 h	1.57 ± 3.1	3.75 ± 13.6	0.42	-
^{43}K	22.3 h	0.347 ± 5.4	2.66 ± 62.3	0.13	-
^{43}Sc	3.9 h	4.03 ± 2.6	24.3 ± 32.7	0.17	-
^{44}Sc	3.9 h	8.29 ± 1.6	9.98 ± 7.1	0.83	-
^{44m}Sc	58.6 h	1.13 ± 1.7	11.1 ± 10.5	0.10	-
^{47}Sc	80.3 h	0.439 ± 3.5	12.4 ± 17.0	0.04	-
^{48}Sc	43.7 h	0.211 ± 5.5	1.05 ± 19.8	0.20	-
^{49}Cr	42.3 m	0.832 ± 2.3	5.28 ± 10.9	0.16	-
^{52}Mn	5.6 d	0.583 ± 1.4	2.26 ± 12.3	0.26	-
^{52m}Mn	21.1 m	0.0466 ± 1.5	0.0549 ± 25.2	0.85	-
^{56}Mn	2.6 h	6.01 ± 2.5	9.68 ± 6.6	0.62	-
^{58}Co	70.8 d	0.229 ± 0.6	0.196 ± 40.3	1.17	-
^{61}Co	99.0 m	10.6 ± 1.5	29.7 ± 13.5	0.36	0.01
^{57}Ni	35.6 h	0.348 ± 4.7	0.944 ± 60.1	0.37	-
^{60}Cu	23.7 m	0.0838 ± 2.5	0.106 ± 23.5	0.79	-
^{61}Cu	3.3 h	58.7 ± 0.9	79.3 ± 28.2	0.74	-
^{64}Cu	12.7 h	61.0 ± 0.8	119. ± 18.6	0.51	0.4
^{62}Zn	9.2 h	1.71 ± 3.4	6.43 ± 15.8	0.27	-
^{63}Zn	38.5 m	0.593 ± 3.1	0.613 ± 26.4	0.97	-

Table 5.11: As in Table 5.8, here for a cooling time of 29d21h13'.

Isotope	$t_{1/2}$	FLUKA (Bq/g) (%)	Experiment (Bq/g) (%)	Ratio	f_{low}
^{7}Be	53.3 d	0.00117 ± 12.7	0.0529 ± 35.3	0.02	-
^{46}Sc	83.8 d	0.0257 ± 1.3	0.0512 ± 17.8	0.50	-
^{48}V	16.0 d	0.133 ± 1.5	0.121 ± 12.4	1.10	-
^{51}Cr	27.7 d	0.240 ± 0.9	0.586 ± 28.4	0.41	-
^{52}Mn	5.6 d	0.0149 ± 1.4	0.0291 ± 20.7	0.51	-
^{54}Mn	312.1 d	0.0458 ± 1.0	0.0653 ± 19.5	0.70	-
^{59}Fe	44.5 d	0.0205 ± 3.1	0.0498 ± 30.5	0.41	-
^{56}Co	77.3 d	0.0571 ± 1.4	0.0912 ± 13.2	0.63	-
^{57}Co	271.8 d	0.0604 ± 0.9	0.176 ± 18.1	0.34	-
^{58}Co	70.8 d	0.262 ± 0.6	0.383 ± 12.2	0.68	-
^{60}Co	5.3 y	0.00554 ± 0.9	0.00788 ± 19.4	0.70	0.16
^{65}Zn	244.3 d	0.0031 ± 3.6	0.0202 ± 28.9	0.15	-

As already done for stainless steel and iron, partial cross-sections for the production of specific isotopes can be calculated with FLUKA and compared to experimental data. Figure 5.11 demonstrates for ^{42}K that the values obtained from the simulation nicely follow the experimental data at higher energies. However, due to the missing multifragmentation model in FLUKA, the threshold at lower energies is not reproduced.

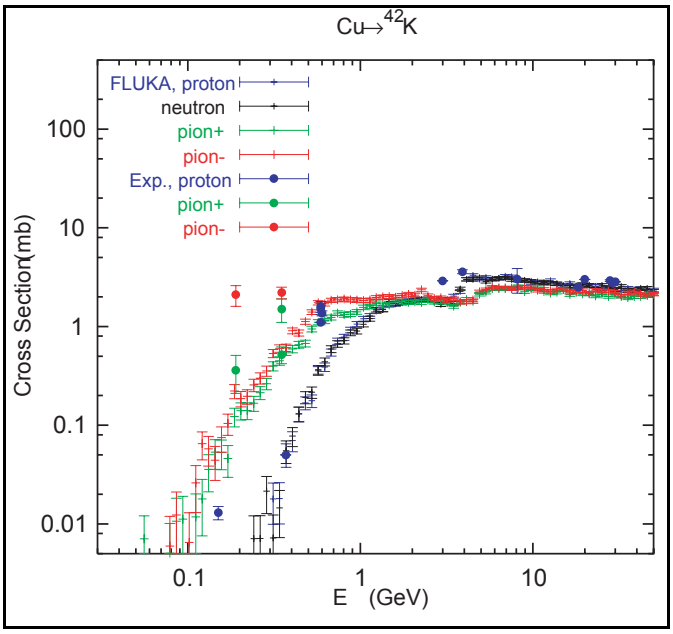

Figure 5.11: Cross-section for the production of ^{42}K in interactions of protons, neutrons and charged pions with copper nuclei. Experimental data (circles) are shown together with the predictions by the FLUKA code (crosses). No experimental data are available from neutron-induced interactions [94].

In case of ^{52}Mn the experimental cross-sections are remarkably well reproduced as shown in Figure 5.12 which is in contrast to the result of the activation benchmark (see Tables 5.10 and 5.11). This fact underlines that the latter have been influenced by a systematic effect, possibly a misalignment of the target or the sample.

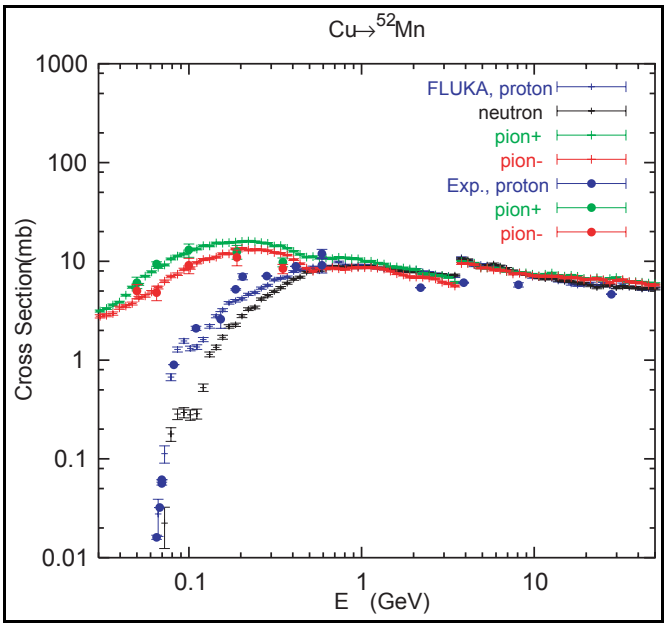

Figure 5.12: Cross-section for the production of ^{52}Mn in interactions of protons, neutrons and charged pions with copper nuclei. Experimental data (circles) are shown together with the predictions by the FLUKA code (crosses). No experimental data are available from neutron-induced interactions [94].

Figure 5.13 shows how well the measured cross-sections for the production ^{60}Cu are reproduced by FLUKA. Unfortunately, no data exist for neutron- or charged pion-induced interactions.

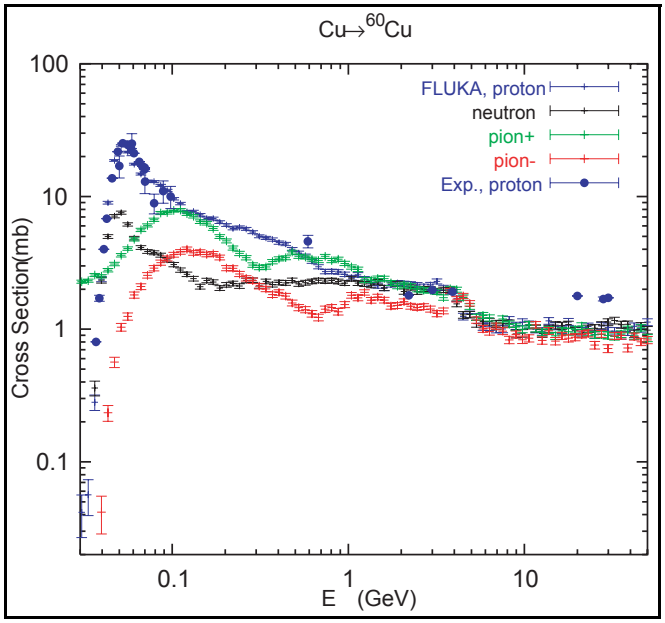

Figure 5.13: Cross-section for the production of ^{60}Cu in interactions of protons, neutrons and charged pions with copper nuclei. Experimental data (circles) are shown together with the predictions by the FLUKA code (crosses). Experimental data are only available for proton-induced reactions [94].

Finally, in the following an example is given where the automatic determination of the specific activity by the analysis software would lead to wrong results. In case of ^{60}Cu the value returned by the software is 41.2 Bq/g giving a ratio of 0.002 between the FLUKA-result and the measured activity (see 5.10). However, gamma-lines of ^{60}Cu are identical to those of other isotopes (see Table 5.12) which has to be taken into account. A manual correction by neglecting the interfering gamma-lines for this particular case results in a measured specific activity of 0.106 or a ratio of 0.79 between the calculated and the measured value. Thus, manual corrections are indispensable in specific cases in order to obtain correct activities.

Table 5.12: Gamma-lines originally used in the activity determination of ^{60}Cu are shown together with interfering isotopes and their respective gamma-lines.

^{60}Cu γ-lines (keV)	Interfering Isotope	γ-lines of Interfering Isotope (keV)	Comments
826.4	^{60}Co	826.3	rejected from analysis
1333.0	^{60}Co	1332.5	rejected from analysis
1333.0	^{52}Mn	1333.0	rejected from analysis
1791.6	^{55}Co	1792.1	accepted for analysis due to the very low yield of this line

Carbon Composite, Boron Nitride and Water

Table 5.13 shows the results for carbon composite, boron nitride and water. The activities for ^{7}Be and ^{11}C were obtained by gamma-spectrometry. The activity of the latter isotope was determined from the 511 keV peak for which it was assumed that no other isotope contribute. Experimental values and FLUKA predictions are in reasonable agreement, in particular for the

boron nitride sample. In case of tritium, the calculated values are lower than the data by about a factor of two.

Table 5.13: Comparison of calculated and measured specific activity in the carbon composite (CC), boron-nitride (BN) and water samples (H_2O). The last column gives ratios between measured and calculated values. The labels refer to the respective measurement time, *e.g.*, CC-1 corresponds to t_{cool1} and CC-2 to t_{cool2}. Errors are quoted in percent.

Id	Isotope	$t_{1/2}$	FLUKA (Bq/g) (%)	Experiment (Bq/g) (%)	Ratio
CC-1	^{7}Be	53.3 d	4.39 ± 3.2	3.07 ± 40.2	1.43
CC-1	^{11}C	20.4 m	0.869 ± 1.5	0.485 ± 2.0	1.79
CC-2	^{7}Be	53.3 d	4.37 ± 3.2	3.55 ± 11.0	1.23
BN-1	^{7}Be	53.3 d	1.71 ± 2.1	1.66 ± 10.1	1.03
BN-1	^{11}C	20.4 m	4.02 ± 2.9	4.13 ± 1.1	0.97
BN-2	^{7}Be	53.3 d	1.68 ± 2.1	1.64 ± 5.3	1.03
H_2O	^{7}Be	12.3 y	49.0 ± 1.5	91.9 ± 4.0	0.53
Id	**Isotope**	**$t_{1/2}$**	**FLUKA (Bq/l) (%)**	**Experiment (Bq/l) (%)**	**Ratio**
H_2O	^{3}H	12.3 y	49.0 ± 1.5	91.9 ± 4.0	0.53

5.3 Remanent Dose Rate Benchmark

During each irradiation two samples of the same material were placed downstream of the copper target, one for later analysis by gamma-spectrometry and a second sample for measurements of dose rate at various cooling times. Both specific activities and dose rates were calculated with detailed FLUKA simulations and compared to the experimental results allowing at the same time two rather independent benchmarks of the code.

In contrast to the predictions of activities for specific isotopes, possible deficiencies in the description of nuclear interactions with FLUKA should have only little influence on integral quantities such dose rates, since over- and underestimates for single elements tend to compensate each other.

5.3.1 Dose Rate Measurements

Dose equivalent rates were measured with a Microspec portable spectrometer by Bubble Technology Industries (BTI)[1]. The built-in detector is a sodium iodide crystal of cylindrical shape and a diameter and height of about 5 cm. The scintillation light is detected by a photomultiplier tube, which converts it into electronic signals and amplifies the response. The sensitivity of the spectrometer ranges from 60 keV to 3 MeV, whereby dose rates can be measured up to 100 µSv/h. Specific characteristics of the electronics are: 8 µs dead time of the Analog-to-Digital Converter, a shaping time of the amplifier of 2 µs in a gain range of 1.6 - 7.3, and 220 channels of the data acquisition system. For quality assurance, before each use, the spectrometer was routinely calibrated with a ^{22}Na source provided by the manufacturer.

Since an absolute comparison of measured and calculated dose rates (especially on contact) requires knowledge of the effective centre of the detector it was determined in the CERN calibration laboratory. The dose rates from three different calibration sources (^{60}Co, ^{137}Cs and ^{22}Na) were measured at distances *R* between the source and the surface of the detector

1. Bubble Technology Industries Inc., HWY. 17, Chalk River, Ontario, Canada K0J 1J0

varying between contact (*R=0*) and 30 cm and the results for each source were fitted using the following $1/R^2$ behaviour:

$$\frac{dD}{dt}\left[\frac{\mu Sv}{h}\right] = \frac{K_0}{(R+R_0)^2} \qquad \text{(xi)}$$

Here R_0 (in cm) denotes the distance from the surface (contact) to the effective centre of the detector and K_0 is a free fit parameter. The largest error to the data is due to positioning uncertainties of the source and was estimated to be about ±3 mm. Data and fit results are shown in Figure 5.14. The fit parameter R_0 varies slightly for the different sources with an average value of 2.44 cm.

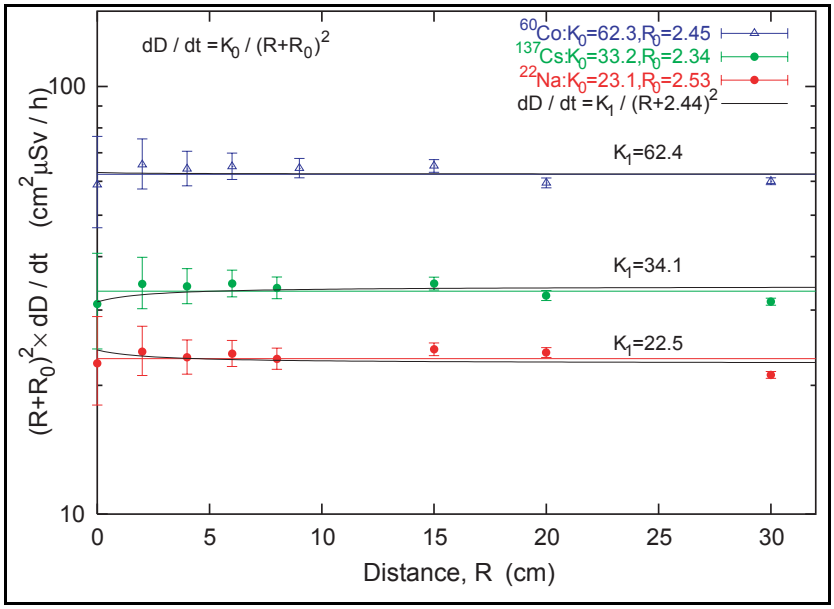

Figure 5.14: Measured dose rates as a function of the distance *R* between the surface of the spectrometer and the respective source. Data are given as symbols with error bars representing a positioning uncertainty of ±3 mm. In addition, the result of a single parameter fit (K_1) is shown. The parameters K_0 and K_1 are in units of cm²µSv/h, and *R* and R_0 and in cm.

Keeping R_0 fixed at 2.44 cm - as done throughout this study - and performing one-parameter fits (K_1) yields dose rates which describe the data still reasonably well (see Figure 5.14). Thus, in the following the effective centre of the detector is assumed to be at 2.4 cm.

Further uncertainties in the measurements with the Microspec spectrometer may result from gain and temperature variations. The former were found to be minor (<0.1%). In order to investigate the temperature effect the spectrometer was put into an oven and the temperature was slowly raised up to 45°7C while the energy spectrum of a ^{22}Na source was measured. The measurements clearly showed that the peak channels decrease linearly with the temperature, but, again, only a minor effect of less than 0.1% was seen.

For the dose rate measurements the irradiated samples were fixed on a holder allowing the adjustment of the distance between the effective centre of the detector and the centre of the sample with an uncertainty of about ±5 mm. Data were taken at three distances: 3.4 cm (contact, *i.e.*, the sample was directly put on the detector surface), 12.4 cm and 32.4 cm. Repetitive measurements without a new alignment of the sample showed a negligible uncertainty of about 0.2%. The measurements were performed in a laboratory with relatively low background radiation (approx. 55 nSv/h).

5.3.2 The FLUKA Calculations

Remanent dose rates were calculated following the two-step approach as discussed in Section 4.3.4. For the first step ("calculation of isotopes"), the implementation of the geometry of the CERF experimental area is identical to the one used for the activation benchmark. In order to increase the statistical significance of the results for the relatively small samples particle transport into the sample region was biased using region importance factors. Isotope information was written into files for a total of 11 cooling times ranging from 12 minutes to 5000 hours (208 days) and for the exact profile of the respective irradiation considering each beam pulse with the actual number of particles. The density of inelastic interactions above 20 MeV ("star density") is shown for a slice through the copper sample in Figure 5.15.

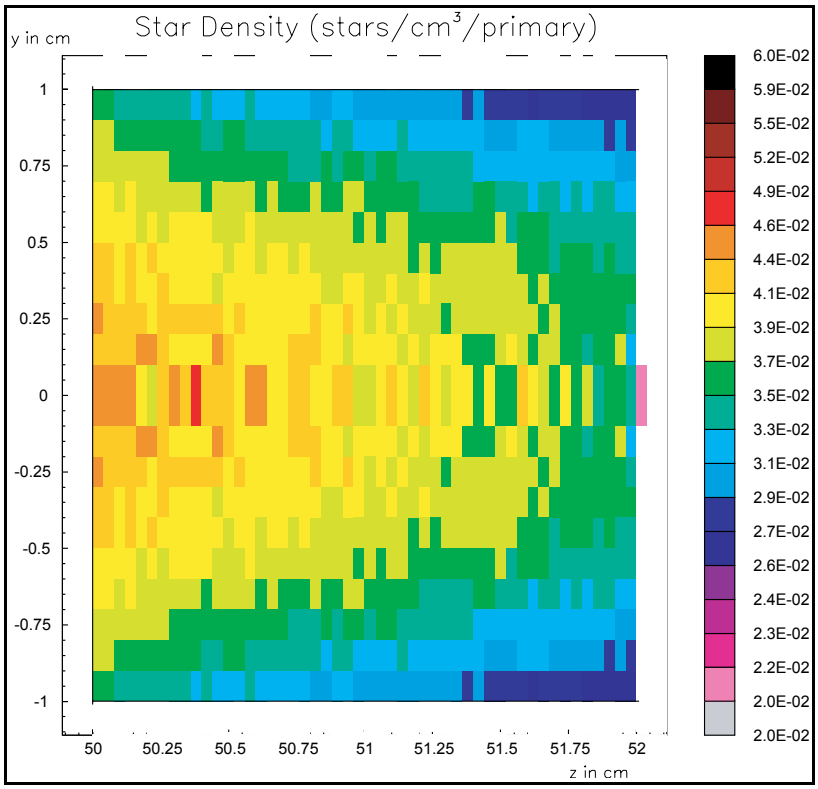

Figure 5.15: Density of inelastic interactions above 20 MeV in the copper sample.

The beam axis coincides with the *z*-axis and the beam points in positive *z*-direction. Thus, the left edge of the contour plot (*z*=50 cm) corresponds to the downstream face of the copper target. It can be seen that the star densities vary only slightly (within a factor of 1.8) within the sample. At the downstream end of the target the beam and the secondary particle cascade has widened sufficiently to provide a rather homogeneous irradiation of the sample.

For the second step of the simulations ("dose rate calculation") the original FLUKA geometry was modified such that all materials other than the one of the sample were set to air. This roughly represents the situation during the dose rate measurements in the laboratory. Backscattering effects of photons from the walls of the laboratory (concrete) were found (by MC simulation) to have only a minor influence on the dose rate results. Therefore, the laboratory walls were neglected in the simulations as was also the sample holder (only small volume for scattering). A dedicated simulation of the electromagnetic cascade was performed for each cooling time and ambient dose equivalent was calculated up to a distance from the sample surface of 50 cm by folding fluence with appropriate fluence-to-ambient dose equivalent conversion factors [95].

As concluded from the star density plot, isotope production in the sample is relatively homogeneous (within a factor of two) and the dependence of the dose rates on the orientation of the sample (*e.g.*, with respect to the detector during the measurements) should be small. This is demonstrated in Figure 5.16 which shows the ratios of the dose rates at the same distance from the respective surfaces of the copper sample. As can be seen, dose rates vary by about 10% depending on the orientation of the sample.

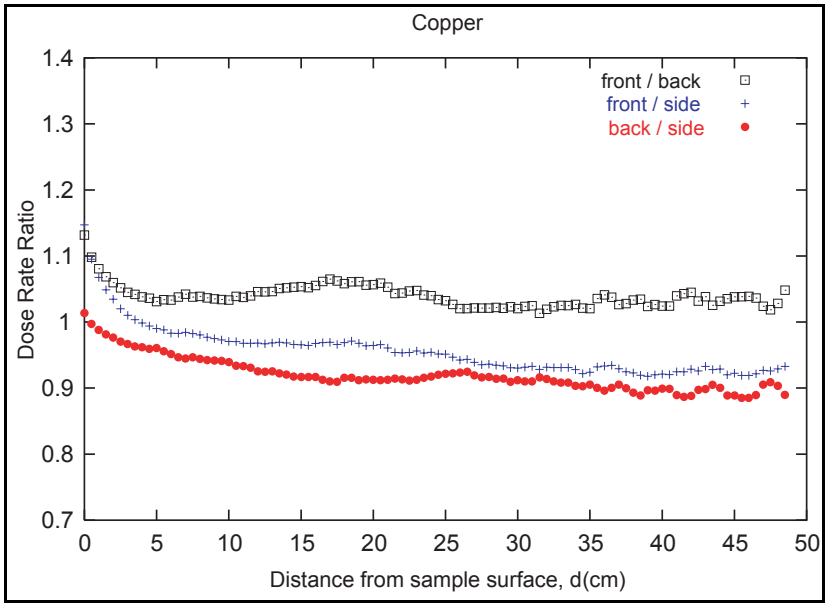

Figure 5.16: Ratio of dose rates in front (the surface facing the target), in the back, and on the side of the copper sample as a function of the distance from the respective sample surface. The fluctuations between the points for each ratio are due to statistical uncertainties.

5.3.3 Comparison of Experimental and Calculated Dose Rates

Dose equivalent rates from photons (including photons from positron annihilation) were calculated for the three distances between the centre of the sample and the effective centre of the detector for which also measurements were performed: 3.4 cm (which corresponds, on contact, to the distance between the centre of the sample and the centre of the detector, R_0), 12.4 cm and 32.4 cm.

Copper

Figure 5.17 shows the results for the copper sample as a function of cooling time. In addition to the total photon dose, the contributions from gamma-ray and positron emitters are given. In the latter case, most positrons are slowed down and annihilate in the sample. The detector then measures the dose rates from the two annihilation photons (511 keV).

As can be seen, positron emitters dominate the total photon dose up to a cooling time of about 20 hours and drop rapidly at larger cooling times. Measured and calculated dose rates agree with each other to within 40% in contact with the detector and to within better than 20% at distances of 12.4 cm and 32.4 cm, respectively. The larger discrepancy in case of contact with the detector is not fully understood yet but could be due, *e.g.,* to geometrical effects. It is certainly not associated with electron emitters as their contribution was found to be negligible. Nevertheless, the overall agreement is remarkable underlining the conclusion that integral

quantities, such as total dose rates caused by many isotopes, are less sensitive to model uncertainties or lack of models (see discussion in Section 4.3).

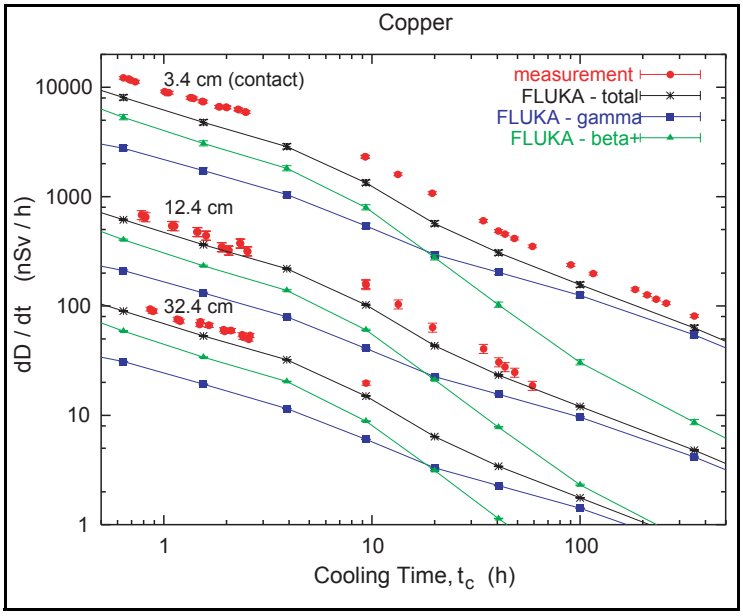

Figure 5.17: Dose equivalent rate as a function of cooling time for the copper sample and the three measurement positions.

For comparison, the dose rate can be estimated by summing over the various contribution of the different isotopes, for a certain cooling time, assuming the source to be point-like and therefore neglecting attenuation as given in Equation *(v)* of Section 4.3.1.

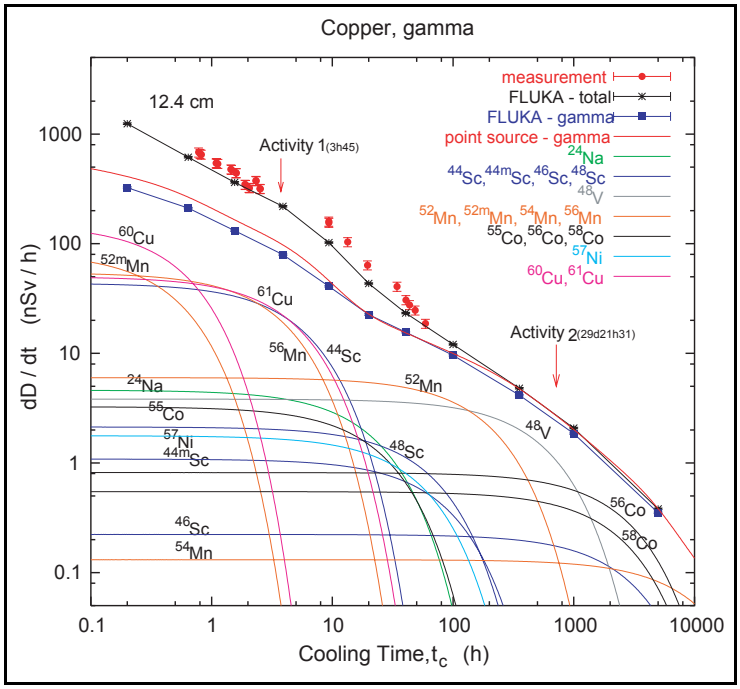

Figure 5.18: Contributions of individual isotopes to the total dose from gamma emitters at a distance to the copper sample of 12.4 cm. The contributions were estimated assuming a point source of photons at the centre of the sample. In addition, the measured and calculated total photon dose rates (from gamma and beta emitters) are shown. Arrows indicate the times of the gamma-spectrometry analysis to determine individual activities (see Table 5.3).

The contributions to the total gamma emitter dose is shown for the copper sample and a distance of 12.4 cm in Figure 5.18. Here, the activities for the individual isotopes are taken as

calculated with FLUKA for a cooling time of 20 minutes and exponential decay is assumed for other cooling times. Of course, this approach cannot take into account self-absorption by the sample and decay chains of radioactive daughter products, *e.g.*, in the case of isomers, but still allows a reasonable approximation to the complete model (*see* curves labelled "point source - gamma" and "FLUKA - gamma"). At small cooling times (t_c<10 hours) copper isotopes (^{60}Cu, ^{61}Cu), as well as ^{56}Mn and ^{44}Sc dominate the dose rate. At larger cooling times (up to one month) ^{52}Mn and ^{48}V clearly contribute most and for cooling times beyond one month various cobalt isotopes become dominant.

Similarly, the contribution of various positron emitting isotopes to the total dose rate can be investigated with the point source approximation. Here, it is assumed that all positrons annihilate at rest in the sample and the dose is exclusively due to the annihilation photons.

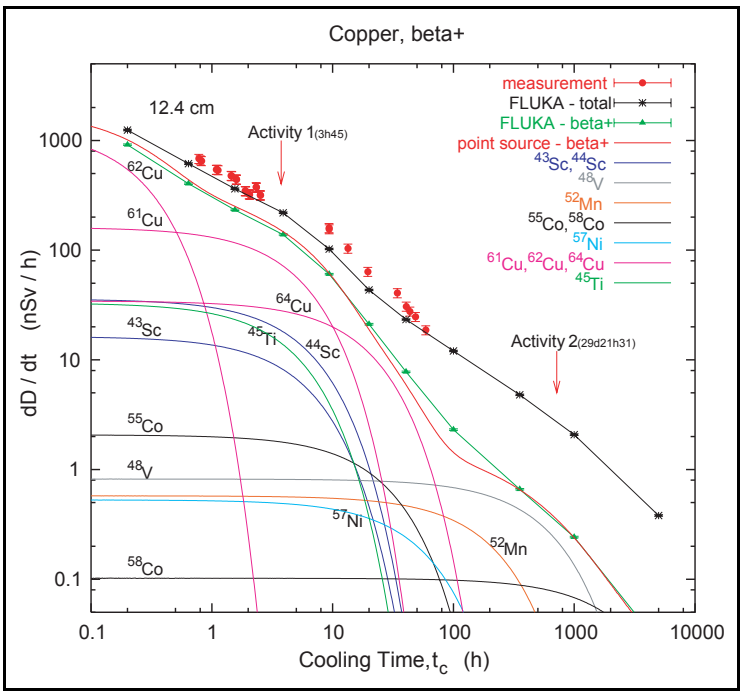

Figure 5.19: Contributions of individual isotopes to the total dose from positron emitters at a distance to the copper sample of 12.4 cm. The contributions were estimated assuming a point source of 511 keV photons at the centre of the sample. In addition, the measured and calculated total photon dose rates (from gamma and beta emitters) are shown. Arrows indicate the times of the gamma-spectrometry analysis to determine individual activities (see Table 5.3).

Figure 5.19 shows that, as for the photon emitters, various copper isotopes dominate the situation at small and intermediate cooling times of up to two days. At larger cooling times, where the dose rate drops rapidly, only ^{48}V and ^{58}Co contribute significantly.

In general, the higher experimental values for copper are consistent with the discrepancies observed in the activation measurements. For short cooling times beta emitters dominate, which are not measured by gamma-spectrometry. Therefore, any direct cross-check with the activation results is not possible up to roughly twenty hours after the end of the irradiation. However, the activities of the gamma emitting isotopes contributing most to the dose rate show the same trend, *i.e.*, are underestimated by the simulation (see Tables 5.10 and 5.11): ^{60}Cu (ratio of 0.79), ^{61}Cu (ratio of 0.74), ^{44}Sc (ratio of 0.83), ^{52}Mn (ratio of 0.26 but most probably due to assumed equal sharing between stable and metastable state), ^{56}Co (ratio of 0.63) and ^{58}Co (ratio of 1.17).

Stainless Steel

For the stainless steel sample, dose rates measurements and simulations agree remarkably well as shown in Figure 5.20.

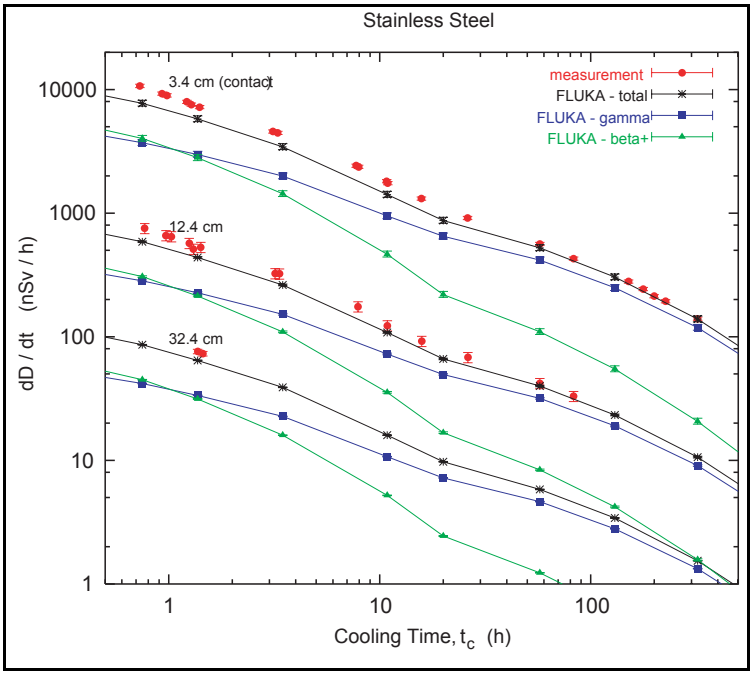

Figure 5.20: Dose equivalent rate as a function of cooling time for the stainless steel sample and the three measurement positions.

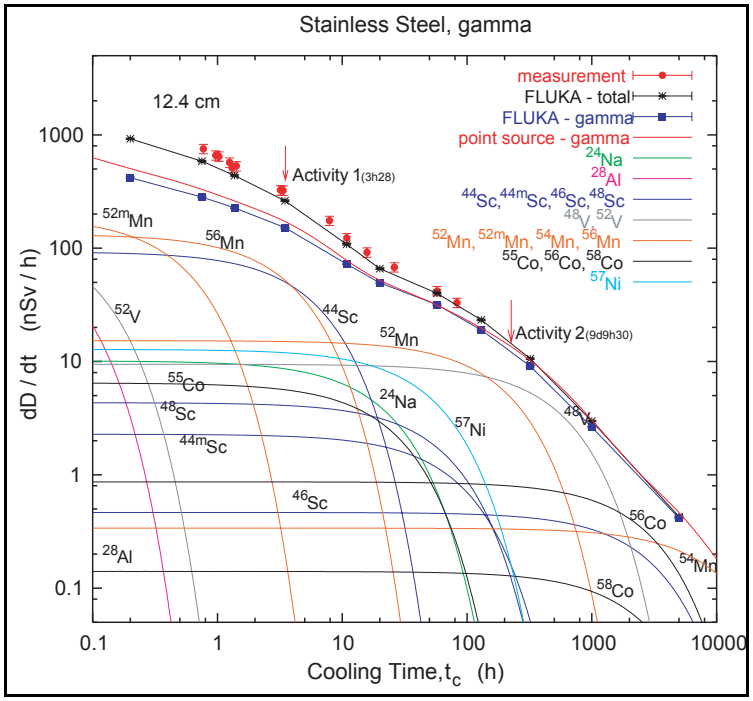

Figure 5.21: As in Figure 5.18, here the contributions of individual isotopes to the total dose from gamma emitters for the stainless steel sample are shown.

In comparison to copper, the dose contribution from positrons is minor at all but very small cooling times (t_c < 1 hour). Obviously, the copper isotopes which, in case of the copper sample, cause most of the dose rate are missing in case of stainless steel.

The contributions of individual isotopes to the dose from photon and positron emitters are shown in Figures 5.21 and 5.22.

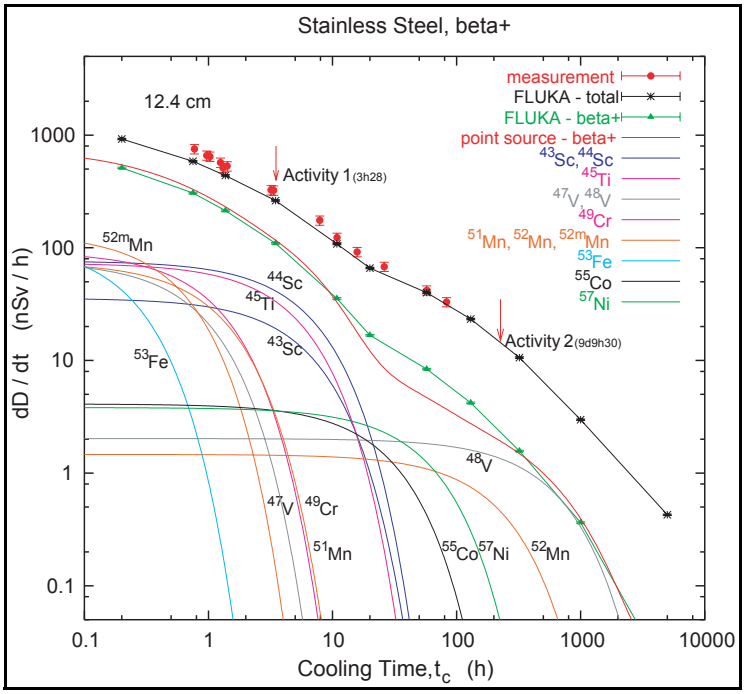

Figure 5.22: As in Figure 5.19, here the contributions of individual isotopes to the total dose from positron emitters for the stainless steel sample are shown.

The existence of nickel in the sample (11% by weight, see Table 5.1) is clearly visible in the contributions from ^{57}Ni and cobalt isotopes. Otherwise the situation is similar to copper: ^{56}Mn and ^{44}Sc contribute at small t_c, ^{52}Mn and ^{48}V dominate at intermediate t_c, and ^{54}Mn and ^{56}Co are dominant at larger cooling times.

Again, the higher experimental dose rates are consistent with the small discrepancies observed in the activation measurements. Some of the gamma emitting isotopes contributing most to the dose rate are slightly underestimated by the simulation (see Tables 5.6 and 5.7): ^{56}Mn (ratio of 0.99), ^{44}Sc (ratio of 0.98), ^{52}Mn (ratio of 0.87) and ^{54}Mn (ratio of 0.84).

Iron

The dose rates calculated for the iron sample are lower than the measured ones by about 35% (see Figure 5.23) although the specific activities of the isotopes contributing to most of the dose rate are well-predicted by FLUKA (see Section 5.2.3). The reasons for this observation are not yet fully understood. The good agreement for stainless steel would have suggested a similar conclusion for iron which is unfortunately not the case. However, even with a 35% underestimation, the approach can be considered to perform reasonably well in describing the dose rates taking into account the various uncertainties. Eventual clarification might be given by an upcoming benchmark experiment, again carried out at the CERF facility.

Similar to stainless steel, emitted positrons are not of importance for the dose rate at cooling times greater than one hour.

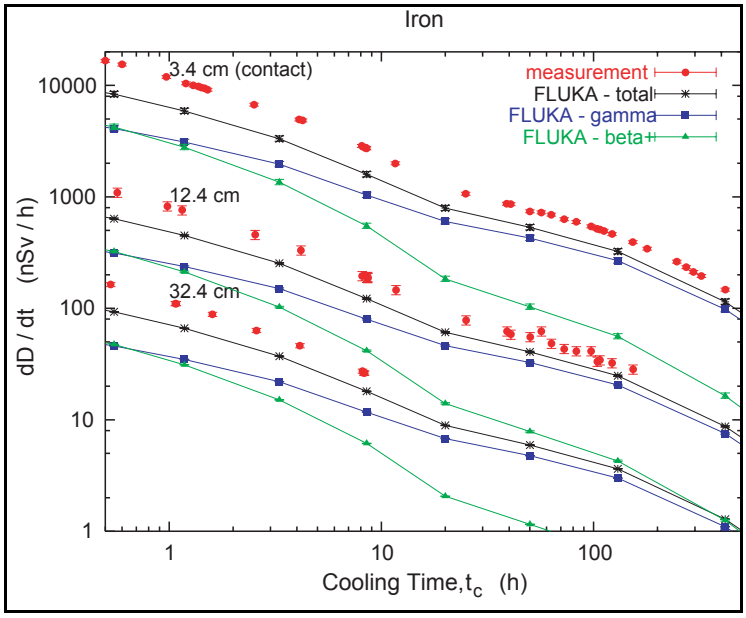

Figure 5.23: Dose equivalent rate as a function of cooling time for the iron sample and the three measurement positions.

Aluminium

The dose rate from the activated aluminium sample is entirely dominated by the sodium isotopes: ^{24}Na for cooling times below about 4 days and ^{22}Na for larger cooling times.

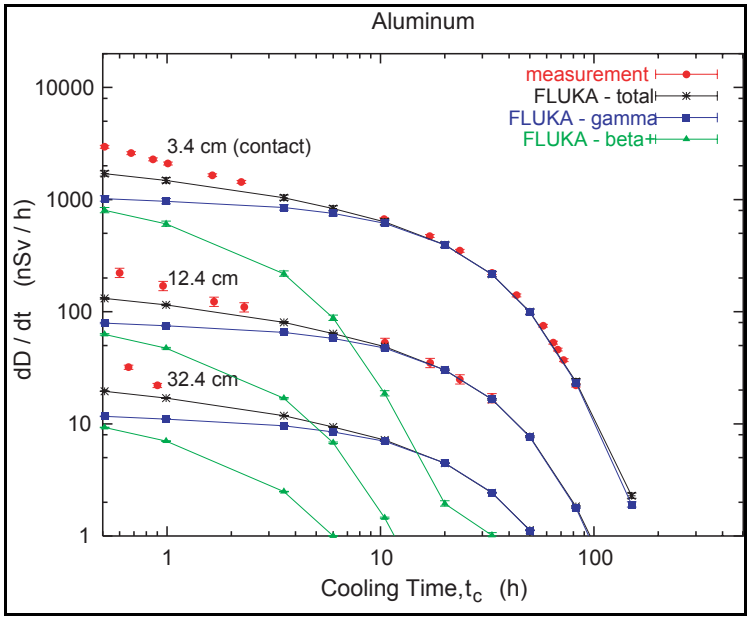

Figure 5.24: Dose equivalent rate as a function of cooling time for the aluminium sample and the three measurement positions.

As the activation study has shown, the ^{24}Na production by high-energy hadrons with FLUKA gives only about 69% of the yield that would be expected from folding hadron fluence with cross-section data and also of what is measured by gamma-spectrometry. It is thus interesting to investigate if the trend is also seen in the dose rates. Therefore, and because it will be only prudent for later predictions for the LHC, a factor of 1.45 is applied to the ^{24}Na activity in the

dose rate calculation step. When applying this factor, the agreement of measured and calculated dose rates is rather good as can be seen in Figure 5.24.

Positron emission does not play a role, apart from very small cooling times below three hours where isotopes such as ^{18}F, ^{11}C, and ^{13}N contribute. For these cooling times the dose rates are slightly underestimated for reasons which are not yet fully understood. It could be due to an underestimation of the production of the respective beta-emitters by FLUKA or due to differences between the actual elemental composition of the sample and the one assumed in the simulation. The contributions of individual isotopes to the dose from emitted photons and positrons is shown in Figures 5.25 and 5.26.

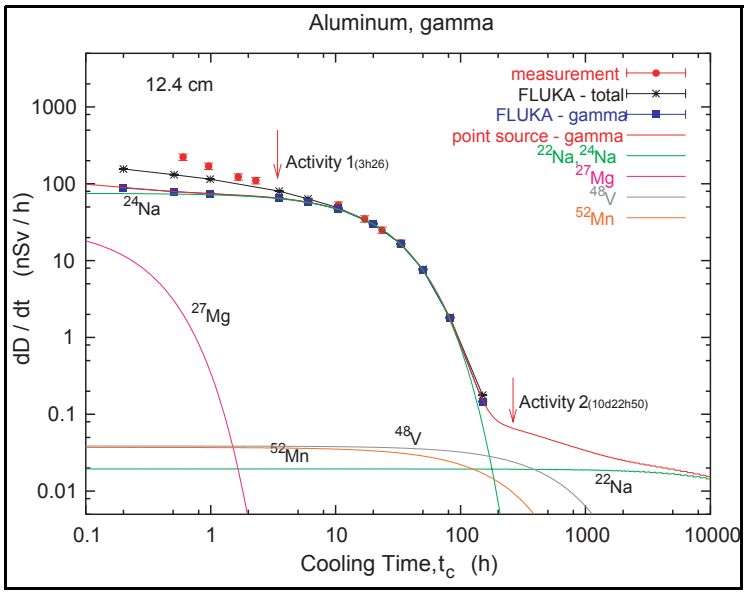

Figure 5.25: As in Figure 5.18, here the contributions of individual isotopes to the total dose from gamma emitters for the aluminium sample are shown.

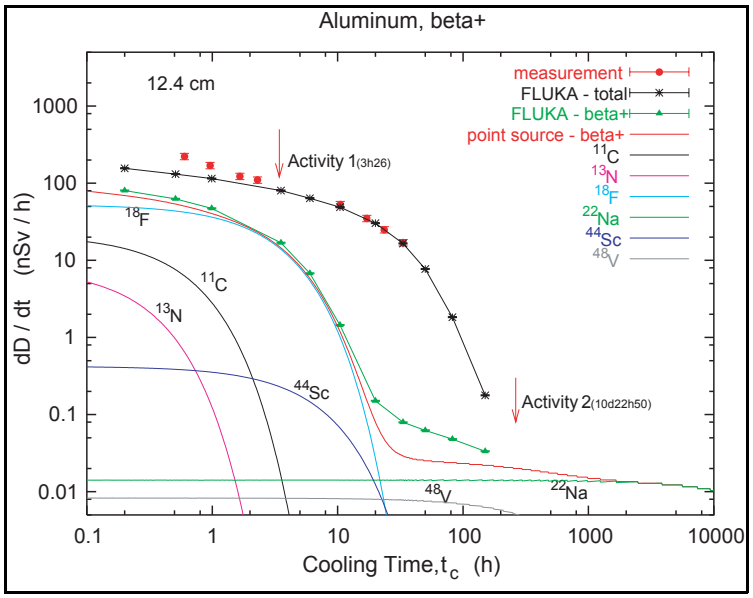

Figure 5.26: As in Figure 5.19, here the contributions of individual isotopes to the total dose from positron emitters for the aluminium sample are shown.

The CERF Target

In order to test the new method also for extended objects, the remanent dose rate of the target was measured as a function of distance from the downstream end and lateral to the target. In

addition to the Microspec spectrometer a second detector[1] (Thermo-Eberline ESM, FH 40 G-10 with an external detector FHZ 672 E) was used for these dose rate measurements. The external detector is a plastic scintillator (90x90 mm), calibrated to give ambient dose equivalent, with a measurement range from a few nSv/h up to several mSv/h. The physical centre of this detector was determined in the CERN calibration laboratory using the same method as for the Microspec spectrometer (see Section 5.3.1). Again, values obtained with the different calibration sources varied only slightly with an average of 7.27 cm.

The dose rates measured with the Microspec and the Eberline instruments are in very good agreement with each other as also with the results of the simulation and are shown in Figure 5.27. Small differences between the results from the two instruments might be explained by their slightly different energy response.

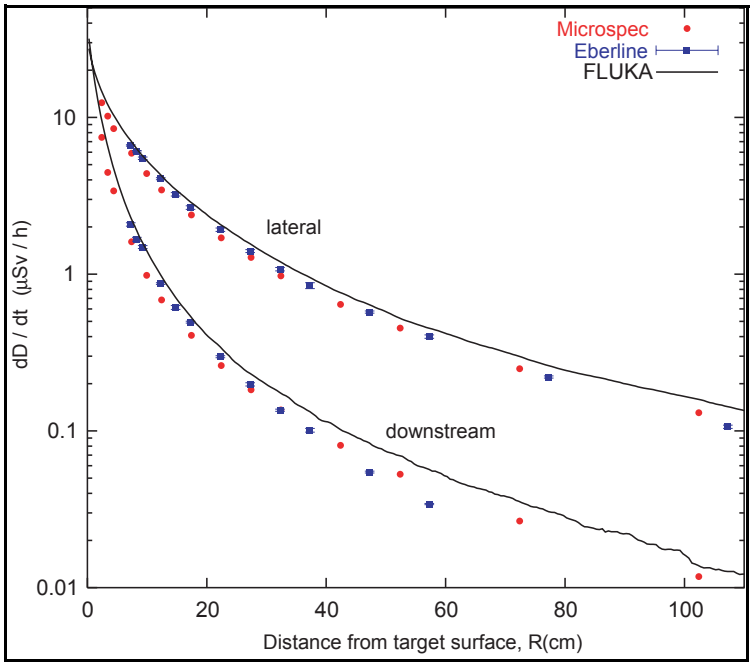

Figure 5.27: Measured (symbols) and simulated remanent dose rates (lines) as a function of distance to the copper target.

For extended objects the calculation of remanent dose rates using star density conversion factors (see Section 4.3.2) is expected to be a reasonable approximation. Therefore, in the following the dose rate as measured at contact and in the longitudinal centre of the target (z=25 cm) is compared to both calculation methods, the explicit method and the ω-factor approach.

As described in Section 4.3.2, ω-factors are related to star density rates assuming a constant irradiation over a given time period. However, during the CERF experiment the beam was not always available, or its intensity was changed. Thus, the intensity was approximated by distributing the total number of beam particles interacting with the CERF target uniformly over the whole period of the CERF experiment of about one week resulting in an average intensity of 1.168×10^6 particles/second.
Since, the dose rate measurement of the target was performed with a cooling time of 8 hours and 6 minutes after an irradiation of approximately 6 days and 19 hours, the available set of ω-

1. APVL, 11 Avenue Marcel Dassault, Quartier des 2 Lions, F-37200 Tours Technopole

factors [73] could not directly be applied, but interpolation was necessary between available values as shown in Table 5.14.

Table 5.14: Available ω-factors for copper for the corresponding irradiation and cooling time as taken from [73].

		Irradiation Time	
		one day	**30 days**
Cooling Time	**6 hours**	7.9×10^{-10}	1.3×10^{-9}
	12 hours	3.6×10^{-10}	8.5×10^{-10}

Two-dimensional interpolation resulted in an ω-factor for the time of the measurement of 8.9×10^{-10} [$Sv.h^{-1}.stars^{-1}.cm^{3}.s$].

In the FLUKA simulations star densities ($stars.cm^{-3}$) were calculated in a three-dimensional mesh covering the whole target. Respective values for star densities at the longitudinal centre of the target were obtained by averaging in *z* between 24.0 - 26.0 cm and in radius *r* over two different ranges: 0.0 - 3.5 cm (*i.e.*, average over all radii) and *r* = 2.5 - 3.5 cm (*i.e.*, average over the outermost centimetre in *r*). For the explicit simulation, the remanent dose rate was calculated for contact with the target (*r* = 3.5 cm) and *z* = 25 cm.

As the measurement with the Microspec spectrometer on “contact” to the target corresponds, in fact, to a distance of 2.4 cm from the surface of the target (physical centre of the detector, see Section 5.3.1) the measured value at this distance was scaled with the calculated behaviour to *r* = 3.5 cm. Resulting dose rates are given in Table 5.15.

Table 5.15: Remanent contact dose rates as obtained with the various methods for the centre of the CERF copper target.

Applied Method	Remanent Dose Rate / μSv/h
ω-factors (R = 0.0 - 3.5 cm)	49.3
ω-factors (R = 2.5 - 3.5 cm)	18.4
Explicit Method	34.3
Measurement	28.1

The results as obtained with the ω-factor approach clearly demonstrate the intrinsic uncertainties in its application to objects which are not uniformly irradiated. In this example it leads to differences of almost a factor of three, overestimating the measured value if star densities are average over all *r* and underestimating the measured value if the star density in the outer layer is used. In the former, conservative case, *i.e.*, averaging over the full lateral range, almost a factor of two difference can be observed with respect to the measurement. In principle, the applied extended method of ω-factors would also include conversion coefficients accounting for neutron activation, in fact, furthermore increasing the calculated result. However, the contribution of neutron activation can be expected to be rather small in this case and was therefore neglected. Finally, comparing the result of the explicit method to the measurement a very good agreement can be observed, especially for the cooling time considered, at which the remanent dose rates are still dominated by positron emitters (see Figure 5.17), thus being an example which can be only accounted for using the full simulation model for dose rate calculations.

5.4 Summary

In this benchmark experiment various samples of different materials typically used at accelerators were irradiated at the CERF facility in the stray radiation field downstream of a copper target. It was shown that at this location particle spectra exhibit a significant high-energy component resembling the situation which can be expected for typical loss regions at high-energy accelerators, *e.g.*, at the LHC. Specific activity as well as remanent dose rates were measured at different cooling times after the irradiation and results were compared to predictions from detailed FLUKA simulations.

For most of the identified isotopes good agreement was found and specific activities were reproduced by FLUKA within the uncertainties of the measurement. However, discrepancies were observed for intermediate and small-mass isotopes which can most likely be attributed to deficiencies in the FLUKA simulation models. In addition, in case of copper the calculated activities are systematically lower than the measured values. Possible reasons for this behaviour, *e.g.,* uncertainties in the elemental composition of the sample assumed in the calculations or a possible misalignment of the sample with respect to the beam axis, are still under investigation. An option to understand the observed discrepancies in a more detailed way is to fold calculated particle fluence with experimental cross-sections for the production of a particular isotope.

However, for the calculation of integral quantities such as total activity or dose rates, observed deficiencies in the production of particular isotopes were assumed to have only small influence, since over- and underestimates for single elements tend to compensate each other as shown with the calculations for remanent dose rates. The simulations were successfully benchmarked with the experimental results and the detailed comparison of measured and calculated dose equivalent rates showed generally good agreement to within 20 - 40 % for the small samples, as well as for extended objects such as the CERF target. In situations where only a few isotopes dominate the dose rate the predictions significantly depend on the accuracy of the models for isotope production. If such deficiencies are known (*e.g.,* from activation studies), it can be compensated for by applying correction factor in the dose rate calculations.

CHAPTER 5 Benchmark Measurements

6 Radiological Studies for the Beam Cleaning Insertions

Radiological studies for the LHC beam cleaning insertions have been performed in the past at various stages of the design of the collimation system. However, since these studies the layout of the insertions has been modified considerably, especially with regard to the collimator material which was recently changed from aluminium/copper to carbon composites. In addition, the air ventilation speed in these insertions was almost doubled as compared to former scenarios due to heat-load considerations. Thus, an update was necessary of the previous radiological studies. In particular, two aspects were selected most critical with regard to the protection of personnel and environment: remanent dose rates due to induced radioactivity and the activation of air.

As about 30 % of the LHC-beam is lost in the cleaning insertions they will become one of the most radioactive locations around the whole LHC ring. Thus, remanent dose rates to be expected during later repair or maintenance interventions must be considered already in the design phase as access time will have to be severely limited. In addition, certain means of remote handling may become essential. As a consequence, the beam cleaning insertions form a unique test bed for the new approach to calculate remanent dose rates which was discussed in detail in Section 4.3.4.

Accurate estimates of air activation is of particular importance for both beam cleaning insertions as at both locations air is released into the environment, moreover, at Point 7 into a densely populated area. Thus, in view of the higher ventilation speed and of modifications in the collimation system and shielding design the safety margin between the estimates and applicable radiological limits will have to be reviewed, the present work forming the calculation foundations.

After a discussion of loss assumptions for the collimation regions and a summary of previous calculations, this chapter describes in detail the studies of both aspects.

6.1 Loss Assumptions

Codes for Monte Carlo simulations in general calculate quantities normalized to the source, *i.e.,* in the case of cascade simulations per primary particle. Therefore, in order to obtain final results the calculated quantities have to be normalized correctly.

For the LHC a summary of design values and interaction rates used in estimating radiological quantities is given in [96]. They are based on the relevant LHC machine parameters as taken from [98], *i.e.,* a total of 2835 proton bunches stored in the machine, each containing 10^{11} protons (see also Table 2.1 in

Section 2.1). This leads to a circulating current per beam of approximately 536 mA. The maximum current considered is 850 mA, which gives a maximum number of protons in one ring of 4.7×10^{14}. The accelerator will operate 180 days per year at high-luminosity (10^{34} $cm^{-2}s^{-1}$) split into three periods of 60 days with two 10-day shut-downs unbeknown, giving a 10-week cycle followed by 15 weeks of annual shutdown.

For proton losses in the beam cleaning insertions it can be shown [99] that interaction rates neither depend strongly on the cleaning efficiency nor on the beam-gas lifetime. The loss rates are also rather independent (variations within only 20 %) of the fill time. These facts allow one to deduce values for the total loss at the collimators which will be valid for most machine conditions. The highest value for the so-called Maximum Machine (maximum values for proton current and luminosity) averaged over 24 hours and based on a 95 % cleaning efficiency is 2.5×10^9 intercepted protons per second and per beam. It is recommended [96] that this value should be used for radiological assessments concerning the environment (*e.g.,* airborne radioactivity). On the assumption of 180 days of operation per year this leads to an annual number of intercepted protons per beam of 4.0×10^{16} eventually increased [97] to 5.0×10^{16}. The latter change is due to the fact that originally only one beam cleaning insertion was foreseen. However, at present, equal sharing is assumed between the two separate cleaning insertion, whereby the total loss figure was slightly adjusted.

However, for the assessment of induced radioactivity, it is more appropriate to use a value based on the expected parameters for the Design Machine (design values for both current and luminosity) which lies close to 1.0×10^9 intercepted protons per second and per beam. To account for the fact of equal sharing of the total loss between the two cleaning insertion the same scaling is used [97] and leads to an annual number of protons lost per beam in each of the scraping regions of 1.0×10^{16}.

The correct loss distribution among the different collimators is typically obtained with so-called tracking codes which are generally used for the accelerator design, *e.g.,* for the prediction of cleaning efficiencies. Among others, these codes include generation of primary beam halo and interactions (elastic and diffractive) of high-energy protons in arbitrary materials, as well as tracking of beam halos in the storage ring. It should be noted that a full shower calculation is not required for most of the tracking applications, *e.g.,* predicting the cleaning of “primary” beam particles.

Two main tracking codes are currently used for the LHC design:

- K2 developed in the 1990’s by Jeanneret and Trenkler for studies of LHC collimation [100],
- STRUCT developed in the 1980’s by Baichev *et al.*, used as for studies of LHC and SSC collimation [101].

An essential component in the tracking codes is an accurate modelling of elastic and diffractive interactions. Since FLUKA is based on more detailed and sophisticated descriptions of these processes it has been used to verify the results of K2 and STRUCT [102]. In particular, proton momenta and scattering angle distributions were calculated for the downstream end of a collimator in a simplified FLUKA geometry and compared to the distributions obtained with the tracking codes. It could be shown that the results of all three codes are in good agreement with each other [102].

For the studies described in the following loss distributions were obtained with the K2 code [103] and later used for a proper normalization of the results. They are shown, separately for the two cleaning insertions, in Table 6.1.

Table 6.1: Loss distributions for the momentum (IP3, Optics V. 6.2) and the betatron cleaning insertion (IP7, Optics V. 5.0). Values are shown as fractions of total loss in percent for primary (TCP) and secondary (TCS) collimators (see also Figure 6.1) [103].

Momentum Cleaning Insertion IP3		Betatron Cleaning Insertion IP7	
Collimator	**Fraction of Total Loss / %**	**Collimator**	**Fraction of Total Loss / %**
TCP	76.1	TCP V1	19.50
TCS 1	5.9	TCP S1	21.15
TCS 2	7.8	TCP S2	21.71
TCS 3	5.4	TCP H1	20.92
TCS 4	2.2	TCS 01	3.80
TCS 5	2.1	TCS 02	1.32
TCS 6	0.5	TCS 03	1.37
		TCS 04	2.11
		TCS 05	1.66
		TCS 06	1.41
		TCS 07	0.92
		TCS 08	1.11
		TCS 09	0.51
		TCS 10	0.75
		TCS 11	0.35
		TCS 12	0.08
		TCS 13	0.42
		TCS 14	0.43
		TCS 15	0.39
		TCS 16	0.10

6.2 Earlier Studies

Several simulations were already performed for the two beam cleaning insertions. Therefore, in the following a short summary on available calculations is given. In particular those aspects are sketched which are important for this work, such as estimates of remanent dose rates and airborne radioactivity.

6.2.1 Simulation Models

The location of the various beamline elements for the optics versions 6.2 (momentum cleaning at Point 3) and 5.0 (betatron cleaning at Point 7) can be found in [106, 107]. These cleaning sections mostly consist of non-superconducting (so-called warm) magnets in order to avoid quenches and high heat loads to cryogenics. Only two out of six quadrupoles are superconducting, namely the Q6 magnets on either side of the collimation regions.

Most recent results for both cleaning insertions were obtained using the Monte-Carlo code MARS [104]. The extended standard geometry language [105] of the MARS code was used to implement the two cleaning sections as a sequence of accelerator elements corresponding to the respective layout version as shown for an unshielded simulation in Figure 6.1.

The two most recent MARS studies for the beam cleaning insertions follow the same methodology as explained in [106]. First the cleaning process is simulated with the K2 code in order to define a map of primary inelastic interactions in the collimator jaws. Then a series of cascade calculations with the MARS code uses this map as a source term together with a detailed geometrical model of the cleaning section (see Figure 6.1), computing energy

deposition, star densities and fluences in order to estimate possible radiation damage, radiation levels and induced radioactivity.

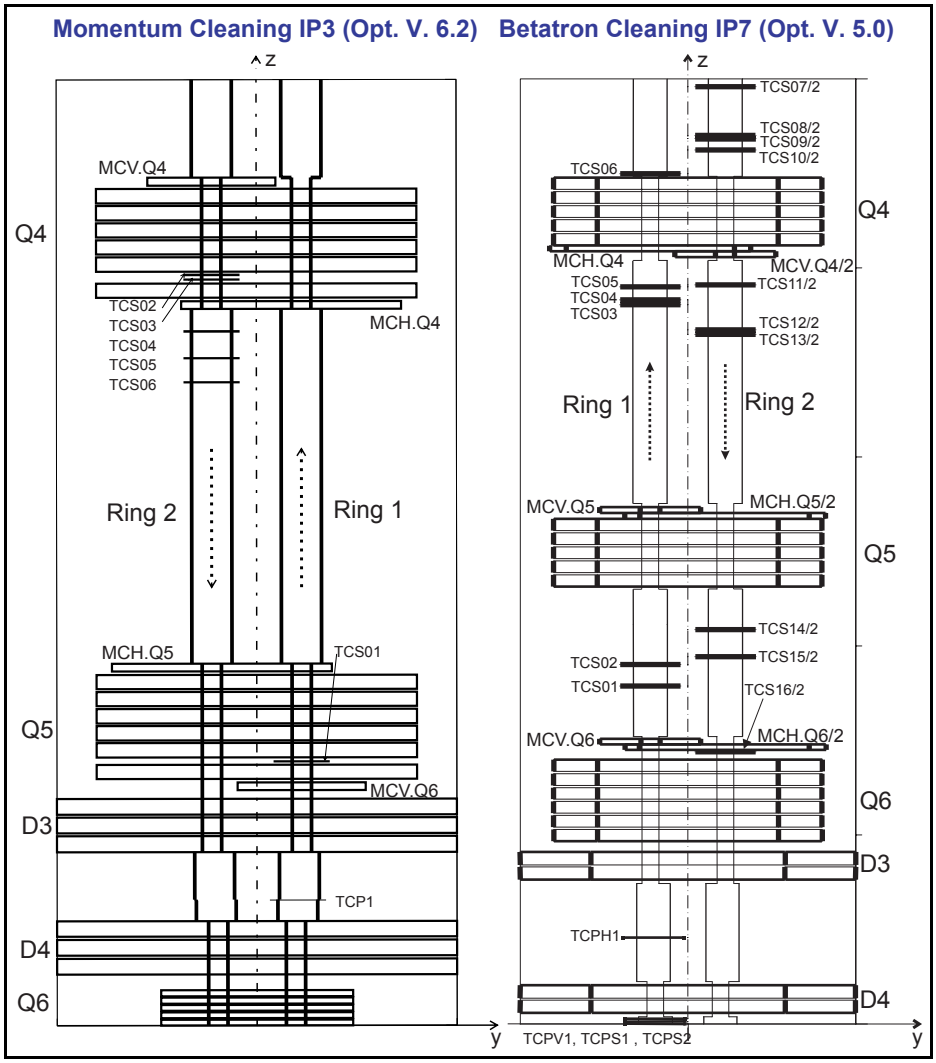

Figure 6.1: Layout of one half of the respective cleaning insertion as implemented in the MARS simulations for IP3 (left) and IP7 (right), respectively [106, 107].

With regard to local iron shielding around the beam pipes in the drift spaces, as well as around the collimators the two simulations are based on different assumptions as shown in Figure 6.2. Please note that the outer shield dimensions are limited by the free space needed for the passage-way in the tunnel.

Especially in case of IP7 a significantly thicker lateral shielding was used below the beam pipes. The shield around the collimators is only slightly different, as well as lateral dimensions in general only show small differences. In addition, it should be noted that a shielding design assuming such a close arrangement around the beam pipes is not practicable. Installations such as flanges, beam position monitors and vacuum pumps make a narrow packing impossible. Furthermore, the requirement for rather fast accessibility in case of maintenance (*e.g.,* leak detection) cannot be ensured.

MARS models for both cleaning insertions are described as a sequence of machine elements according to the respective optical layout. One longitudinal half of the respective geometry is shown schematically in Figure 6.1. Machine elements are primary (20 cm length) and secondary (50 cm length) collimators, warm dipoles, warm quadrupoles and dipole correctors as well as beam pipes in the drift spaces between magnets and collimators. In addition, iron

shielding was added to the geometry with typical transverse cross-sections as shown in Figure 6.2. The geometry is described in a right-handed orthogonal system with its origin defined to be in the centre between the two beam axes pointing parallel to the *z*-axis. Each collimator is implemented as a pair of jaws inside a vacuum vessel.

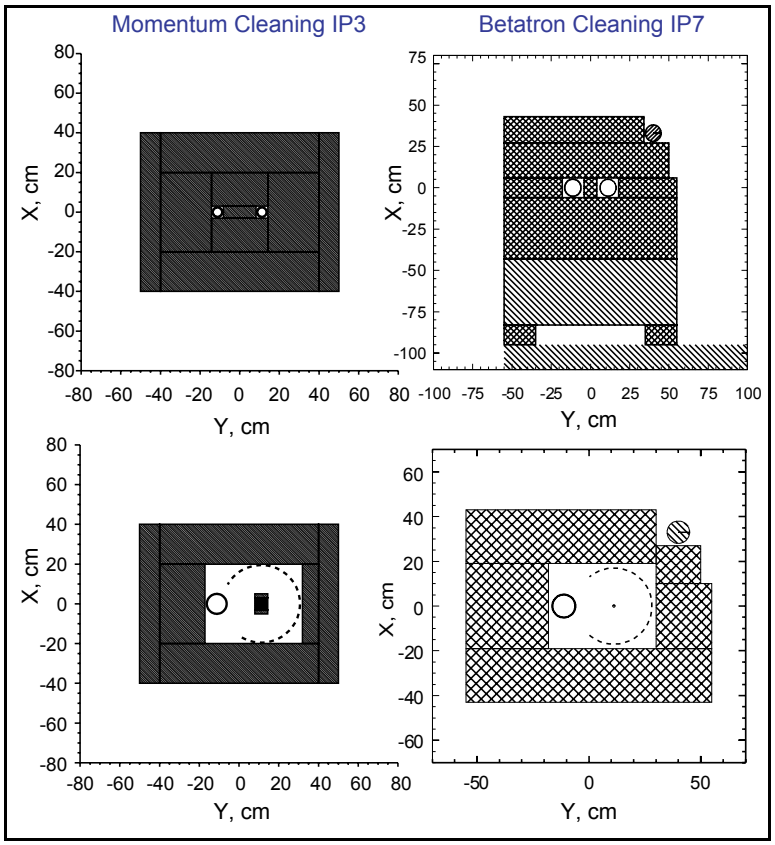

Figure 6.2: Cross-sectional view of the regular shielding around the beam pipes and the collimator vessels as assumed for the MARS simulations for IP3 (left) and IP7 (right), respectively.

The geometry and functionality of the quadrupoles consisting of several modules of warm magnets (MQW) are described in [108], together with the respective dipole magnets for the beam separation (MBW). For all magnets two-dimensional magnetic field maps were implemented as given in [109] in order to simulate the correct transport of charged particles inside the dipoles and the quadrupoles. Next to each quadrupole dipole correctors are situated so that *e.g.,* the vertical corrector of the inner ring coincides with the horizontal corrector of the outer beam pipe. The two millimetre thick copper beam pipes made out of copper have an outer diameter of 48 mm in the short drift spaces between the magnets and 105 mm, respectively, in the long drift spaces.

The latest MARS model of the momentum cleaning insertion is based on the lattice version 6.2 (see Figure 6.1) and consists in each ring only of one primary aluminium and 6 secondary copper collimators, the latter oriented at different angles around the beam axis. As for the betatron collimation the layout as implemented in optics version 5.0 consisting per ring of four primary aluminium and 16 secondary copper collimators oriented in different angles with respect to the horizontal axis.

6.2.2 Remanent Dose Rates

Contact dose rates were only calculated on the surface of the iron shield and magnets in the respective cleaning section. Results were obtained with the classical ω-factor approach (see Section 4.3.2).

IP3

Results are normalized to 1 x 10^9 protons per second and ring interacting in the momentum cleaning insertion. Figure 6.3 shows the contact dose rates as a function of the longitudinal position for both rings.

The contact dose rate reaches a maximum value of 2.5 mSv/h near the first secondary collimator TCS1 and near the bare coil ends of the dipole and orbit corrector magnets. In most of the regions the dose rate exceeds significantly the value of 100 μSv/h. It should be noted that the same study [107] states that without shielding the contact dose rates from induced radioactivity in the collimator jaws, the front bare coils and the beam pipes would exceed values of 100 mSv/h.

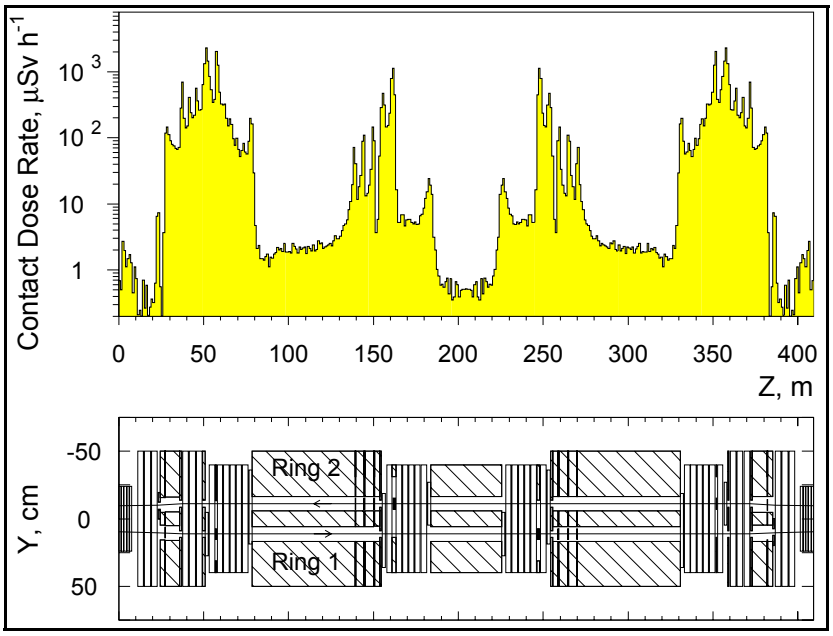

Figure 6.3: Contact dose rates on the surface of the iron shield and magnets in the momentum cleaning section as taken from [107].

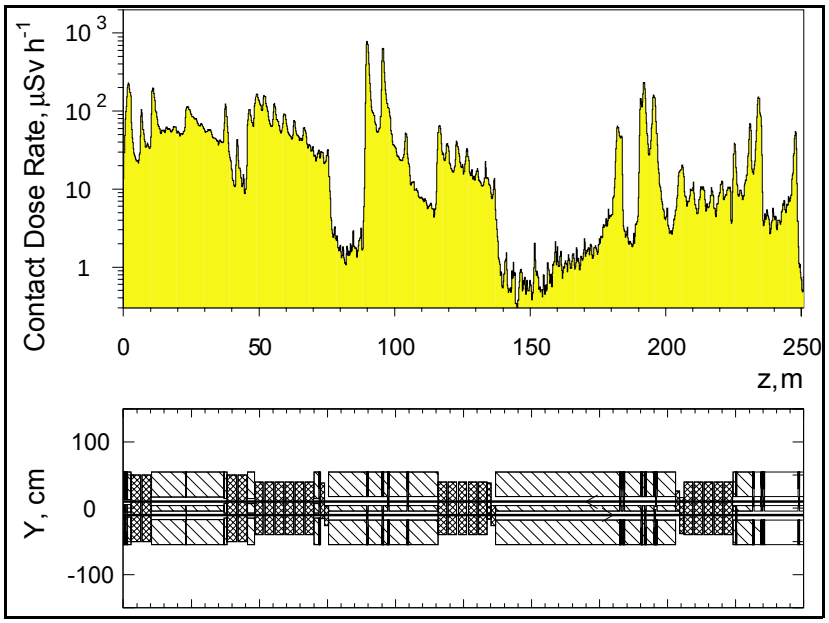

Figure 6.4: Contact dose rates on the surface of the iron shield and magnets in the betatron cleaning section as taken from [110].

IP7

As in the case for Point 3 contact dose rates were only calculated on the surface of the iron shield. For the betatron cleaning insertion (IP7) dose rate estimates exist only for optics Version 5.0 [110] and obsolete loss term calculations for the collimators [111, 112]. Results are normalized to loss rates of 1 x 10^9 protons per second and ring interacting in the betatron cleaning insertion. Figure 6.4 shows the contact dose rates with the contribution from only one ring as a function of the longitudinal position in one half of the cleaning insertion. Contact dose rates reach maximum values of about 1 mSv/h near the first secondary collimators.

Numerous installed equipment in both cleaning insertions certainly will require maintenance. As the above discussed calculations have shown, remanent dose rates are significant, but estimates are so far only based on the ω-factor approach. However, in the late design phase of the new collimation systems, due to high expected dose rates calculations for maintenance interventions became a more stringent, thus the beam cleaning insertions will form an unique testbed for the new approach to calculate remanent dose rates.

6.2.3 Activation of Air

First estimates for airborne radioactivity for both scraping systems are described in [113]. They were based on 18 most abundant radioactive nuclides produced in air with half-lives longer than one minute. As for the studies carried out with the above described MARS simulations an updated set of 39 radionuclides was used in order to determine the radioactive isotope production in the cleaning insertion.

For Point 7 results are available for both the isotope production and the release on the surface as described in [110]. It should be noted that these calculations for IP7 included only air activation outside the shield. For Point 3 only unpublished results [114] were available for the isotope production in the momentum cleaning insertion. Therefore, a recently published report [115] describing the calculation of the effective dose to the public due to air releases coming from LHC facilities, assumes equal losses for both collimation regions and refers to isotope yields as obtained in [110] for Point 7.

The upcoming new collimation layout using different materials, as well the inconsistent optics versions and shielding designs used in the MARS simulations lead to incomplete and partly ambiguous results, therefore motivating the study described in Section 6.5.

6.3 Remanent Dose Rates - Simplified Layout

As compared to the total length of a cleaning insertion of more than 500 m, particle losses at collimators activate only “locally” the surrounding area. This is also supported by Figures 6.3 and 6.4 which show that areas of high dose rate extend only up to about 10 to 20 m downstream of the respective collimator. Hence, for a calculation of remanent dose rates it is not necessary that the layout of the whole cleaning insertion is implemented in full detail but it should be sufficient to consider only a small section with typical configurations. Those configurations can be roughly classified into two cases:

- The collimator is located in a sector without other massive beamline elements (magnets, *etc.*) downstream of it. Thus, particle losses activate the collimator, the downstream vacuum pipe and equipment as well as any local shielding and the concrete of the surrounding tunnel.
- The collimator is installed in the vicinity of a (downstream) magnet. In this case also the front face of the magnet will be significantly activated. However, the “hot” area extends only from the collimator to the magnet.

As will be shown below, the former configurations can be studied with rather simplified models, typically based on cylindrical approximations. The advantage of those geometries is that results with good statistical significance can be reached relatively fast and, therefore, allows the study of many different layouts (collimator materials, shielding scenarios, *etc.*). For the latter more effort has to be put into the description of the beamline section, however, as already mentioned, extending only from the collimator to the downstream magnet.

The FLUKA calculations are based on a 10 m long section of the LHC tunnel, approximated by cylinders, symmetric around the *z*-axis. The following components are considered (from the in- to the outside): a collimator, 6 cm in diameter and of a certain length (described as solid cylinder, *i.e.,* without aperture), a 2 mm thick copper beam pipe, a 20 cm thick iron shielding (optional), the inner shield surface being at a radial distance of 20 cm to the beam axis and a 30 cm thick concrete layer at radial distance of 190 cm.

For the collimator different materials were used according to the proposals discussed in the collimator-design study group: carbon composite, boron nitride, aluminium, copper and tungsten. Aluminium and copper are the collimator materials assumed in all former designs of the beam cleaning insertions (and in all previous radiological studies). Thus, they were kept in this study for reasons of comparison. Recent heat-load and material stress calculations identified low-Z materials as the best choice. Therefore, carbon composite and boron nitride were included in this study. In fact, carbon composite will most likely be chosen as main collimator material in the final design, which is presently under discussion. Finally, simulations were also performed for tungsten collimators in order to address also high-Z materials, although presently unlikely to be used for LHC collimators.

As discussed in Section 4.3, there are essentially two methods to calculate remanent dose rates, one of them based on ω-factors (and therefore giving only contact dose rates) and the second approach (being one of the main subjects of this thesis) in which dose rates are estimated by an explicit calculation of radioactive isotopes, their decay and the Monte Carlo transport of the radiation from the decay. As for the ω-factor method two version exist: a former, “classical” method using an old set of factors, based on 30 days of irradiation and 1 day of cooling and on a threshold of 50 MeV in the definition of a star and a new, revised set of factors for arbitrary irradiation and cooling times and a 20 MeV threshold for stars.

In the following both methods were applied to the simplified layout and results were compared to each other. The explicit approach is then used to show in detail how the various parts of the geometry (collimator, shield, tunnel, *etc.*) contribute to the total dose rate at various cooling times and to demonstrate its versatility in the estimation of doses received during interventions at collimators.

6.3.1 ω-Factor Approach

In all previous calculations remanent dose rates were estimated with the classical ω–factors, based on a 50 MeV threshold in the definition of a star. In order to be able to compare predictions of the new calculations with the old results, the collimator lengths were chosen to be identical to those used in these earlier studies, *i.e.,* 20 cm for aluminium and 50 cm for all other materials.

FLUKA-simulations were performed with these collimators in a geometry including shielding. The latter should be an ideal test bed for ω–factors, at least as far as its size is concerned, since the shield is a rather large object. However, it is not uniformly activated, which is one of the basic assumptions of ω–factors. Star densities were calculated for the collimator and the shield and were folded off-line with the appropriate ω–factors (given for 30 days of irradiation and one day of cooling). Furthermore the results were normalized to a total particle loss of 1×10^{16}

protons per year. Results are given in Table 6.2 for the collimator, as well as the inside and the outside of the shielding. In the latter two cases, the average star density only on the inner/outer 2 cm of the shield was used.

Table 6.2: Maximum remanent dose rates on the outer surface of the collimator as well as at the inside and outside of the iron shield. For a 50 MeV threshold ω-factors are only available for a limited number of ferrous materials, hence, no results can be given in the case of boron nitride and carbon composite.

Collimator Material (Length)	Maximum Contact Dose Rates / mSv/h		
	Collimator	Shielding Inside	Shielding Outside
Aluminium (20 cm)	-	2	0.2
Carbon Composite (50 cm)	-	9	0.7
Boron Nitride (50 cm)	-	8	0.6
Copper (50 cm)	3000	100	9.0
Tungsten (50 cm)	8000	200	20

For the copper collimator the maximum remanent dose rate on the outside of the shield is about 9 mSv/h. The difference when compared to earlier simulations (~2.5 mSv/h, see Section 6.2.2) is due to two reasons. The first being the reduced shielding of only 20 cm of iron and the second that secondary particles escape through the aperture of the collimator thus leading to air activation in the forward direction.

In a next step, in order to adapt the calculations to more realistic parameters the extended set of ω–factors was applied to the FLUKA simulations. Therefore, high-energy omega factors were interpolated (see Table 6.3) for 180 days of irradiation and one day of cooling from the available set as given in [73]. For beryllium no conversion factors were available, thus as a good approximation the ω–factors for carbon were used, as in the case of carbon composites.

Table 6.3: ω–factors for various materials and irradiation times of 1 day and 1 year [73]. In addition, the value as interpolated for a irradiation time of 180 days is given.

Material	Irradiation Time		
	One Day	One Year	180 Days
Carbon Composite	3.20×10^{-12}	3.20×10^{-10}	1.27×10^{-10}
Beryllium	3.20×10^{-12}	3.20×10^{-10}	1.27×10^{-10}
Copper	2.80×10^{-10}	4.00×10^{-09}	2.14×10^{-09}

These ω-factors were then folded with the star density production in the various elements. All results are normalized to the total annual loss at one interaction point for each beam, hence referring to 1.0×10^{9} protons per second. In order to account for the present design change the geometry was slightly modified with respect to the material dependent length of the collimator. The same total hadronic interaction length of the original 50 cm long copper collimator (Cu) was kept, therefore resulting in a 126 cm long carbon composite (CC) and a 135 cm long beryllium collimator (Be). For each collimator material Table 6.4 lists the maximum remanent dose rates

as reached at the various locations of the geometry - the surface of the collimator, the surface of the copper beam pipe as well as the inside and the outside of the iron shield.

Table 6.4: Maximum remanent contact dose rates reached at different locations using a 20 MeV threshold for inelastic interactions.

Collimator Material (Length)	Maximum Contact Dose Rates / mSv/h			
	Collimator	Beam Pipe	Shielding Inside	Shielding Outside
CC (126 cm)	4.6	58	23	2.4
Be (135 cm)	4.6	55	25	2.7
Cu (50 cm)	304	148	51	5.6

In order to illustrate the longitudinal distribution along the collimator section Figure 6.5 shows the remanent dose rate at contact to the beam pipe for the various materials. Please note that this dose rate reflects only the contribution of the pipe but not of other adjacent components (*e.g.,* collimator, shield). When compared to derived limits as described in Section 3.2.1, dose rates for all three materials clearly exceed 20 mSv/h, above which remote handling becomes essential. However, for thin objects as beam pipes the ω-factor approach is known to be too conservative and realistic values can be expected to be significantly lower.

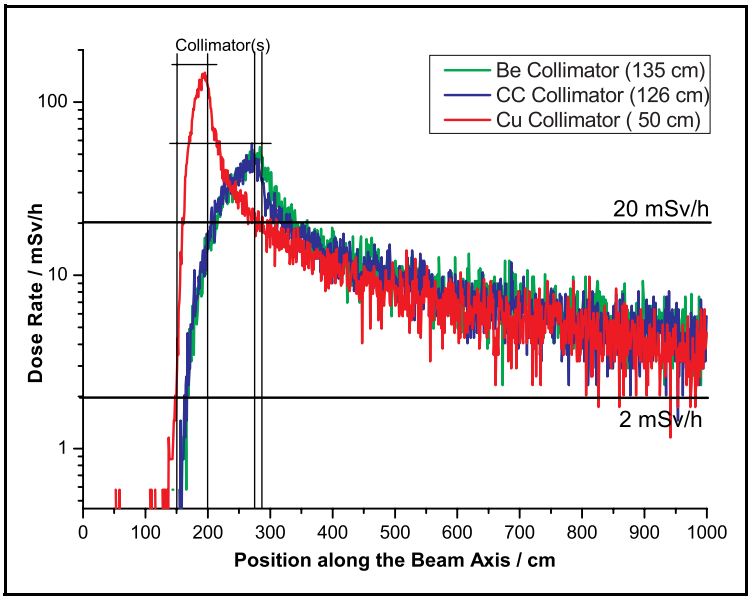

Figure 6.5: Dose rates along the beam axis at the lateral position of the beam pipe for beryllium, carbon composite and copper collimators. Vertical lines indicate the locations of the collimators.

Usually it is assumed, that the massive iron shielding is also a dominant source of remanent activity, since secondaries produced in the collimator cause hadronic cascades in the shield and create a significant activation. This leads to significant remanent contact dose rates as illustrated in Figures 6.6 and 6.7, for the inside and outside of the iron shield. As expected, dose rates are similar in case of carbon composite and beryllium collimators whereas they are significantly higher close to the copper collimator. In all cases values are reached which would not only require dose optimization in design and maintenance of the beam cleaning insertions, but also certain means of remote handling collimators and adjacent beamline components (vacuum equipment, magnets, beam loss monitors, *etc.)*.

However, a thorough assessment of repair or maintenance interventions is unfortunately not possible with the ω-factor approach. The assumption of being in contact with the objects would yield too conservative estimates whereas the neglect of positron emitters may lead to

underestimates (*e.g.,* in case of copper and short cooling times), the net-effect being not always obvious. Therefore, the new, explicit approach to calculate remanent dose rates was applied to the same simplified, cylindrical geometry as described in the following.

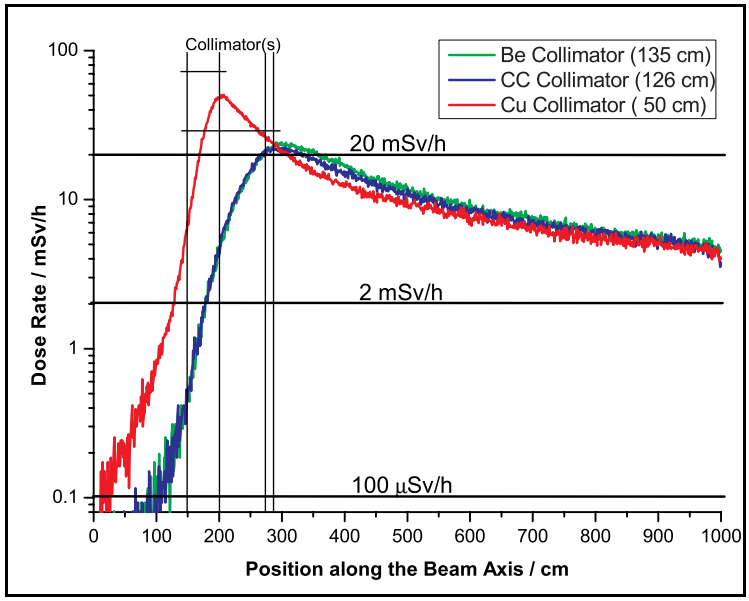

Figure 6.6: Dose rates along the beam axis at the inside of the iron shield. The dose rates are compared for various collimator materials (Be, CC, Cu). Vertical lines indicate the locations of the collimators.

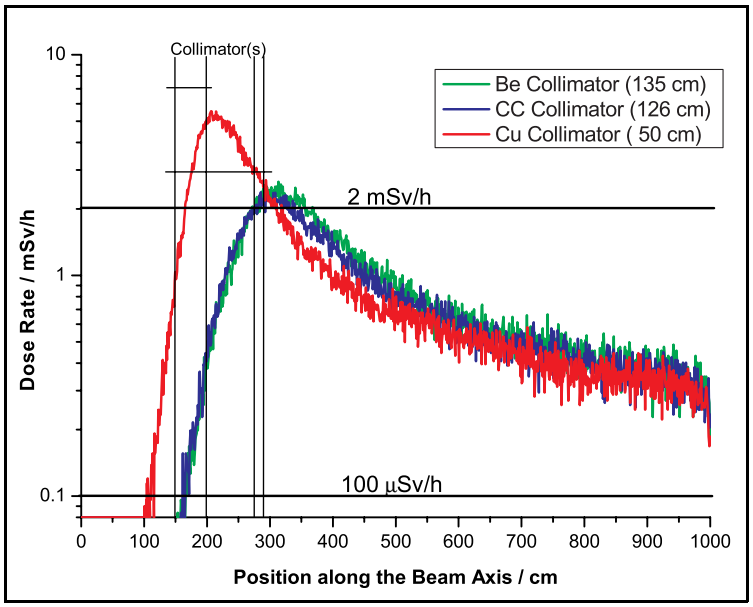

Figure 6.7: Dose rates along the beam axis at the outside of the iron shield. The dose rates are compared for various collimator materials (Be, CC, Cu). Vertical lines indicate the locations of the collimators.

6.3.2 Explicit Approach

For the same simplified collimator layout, as an alternative to the ω-factor method, a full simulation of isotope production and of the transport and interactions of the radioactive decay products was performed. To remind, this two-step approach first calculates the produced isotopes for a certain cooling time and then transports the produced photons, electrons and positrons. This gives results for remanent dose rates scored in a three-dimensional mesh for any location within the 10 m long tunnel section. Please note that all results are again normalized to the total annual loss for each of the two beams in one cleaning insertion, thus

1.0 x 10^{16} protons. As for the collimators the same length as for the ω-factor approach was kept, 50 cm for copper, 126 cm for carbon composite and 135 cm for beryllium.

It should be noted, that in an application of the explicit approach to large geometries small and big volumes may contribute equally to the remanent dose rate. As will be shown later the dose rate in the aisle from the activated tunnel wall might be of the same order of magnitude as the dose rate from a radioactive collimator. Thus, in the simulation it is important to achieve equal statistical uncertainties for both contributions. However, the statistical uncertainty is often directly related to the size of the region, *i.e.,* far more histories (primary particles) have to be calculated to obtain results for small volumes with the same statistical significance than for big volumes.

For this reason, in large geometries the isotope production (first step in the explicit calculation of remanent dose rates) is typically not calculated in a single simulation for all regions, but several simulations are performed, in which the isotope production is calculated separately for small and big regions, averaged over different numbers of primary particles (less for big volumes, more for the smaller ones). The second simulation step (sampling and transport of radioactive decay products) is then also performed separately for the various contributions and results are finally added up to obtain the total dose rate from all components.

a)

b)

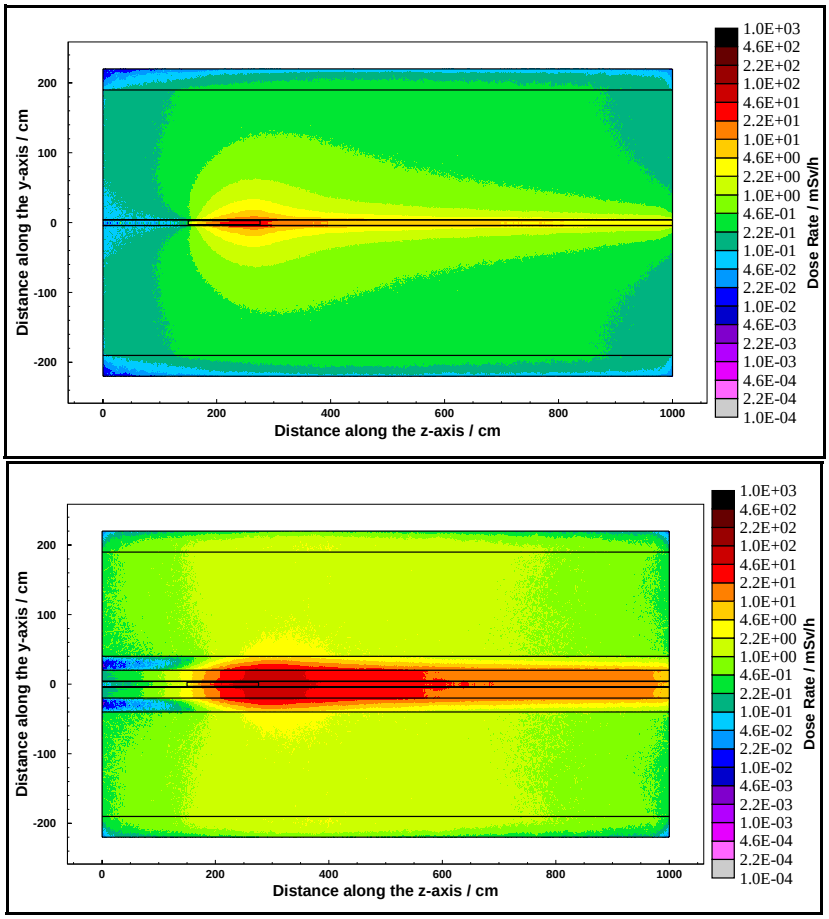

Figure 6.8: Remanent dose rate distribution after 180 days of operation and one day of cooling for the unshielded (a) and the shielded geometry (b).

Therefore, simulations were performed separately for each collimator material, the respective source of interest as well as for a shielded and an unshielded scenario. Carbon was assumed as collimator material leading to a total dose rate distribution as shown in Figure 6.8 for the unshielded and shielded cases. All contour graphs represent a longitudinal cut through the cylindrical geometry with the collimator in the left central part, then, from the inside to the

outside, the beam pipe, the optional shield, the aisle and the tunnel wall. The 7 TeV proton beam pointing in positive *z*-direction interacts on the collimator at z = 150 cm. Please note that all results are shown as remanent dose rates in mSv/h as calculated for a cooling time of one day after 180 days of operation.

a)

b)

c)

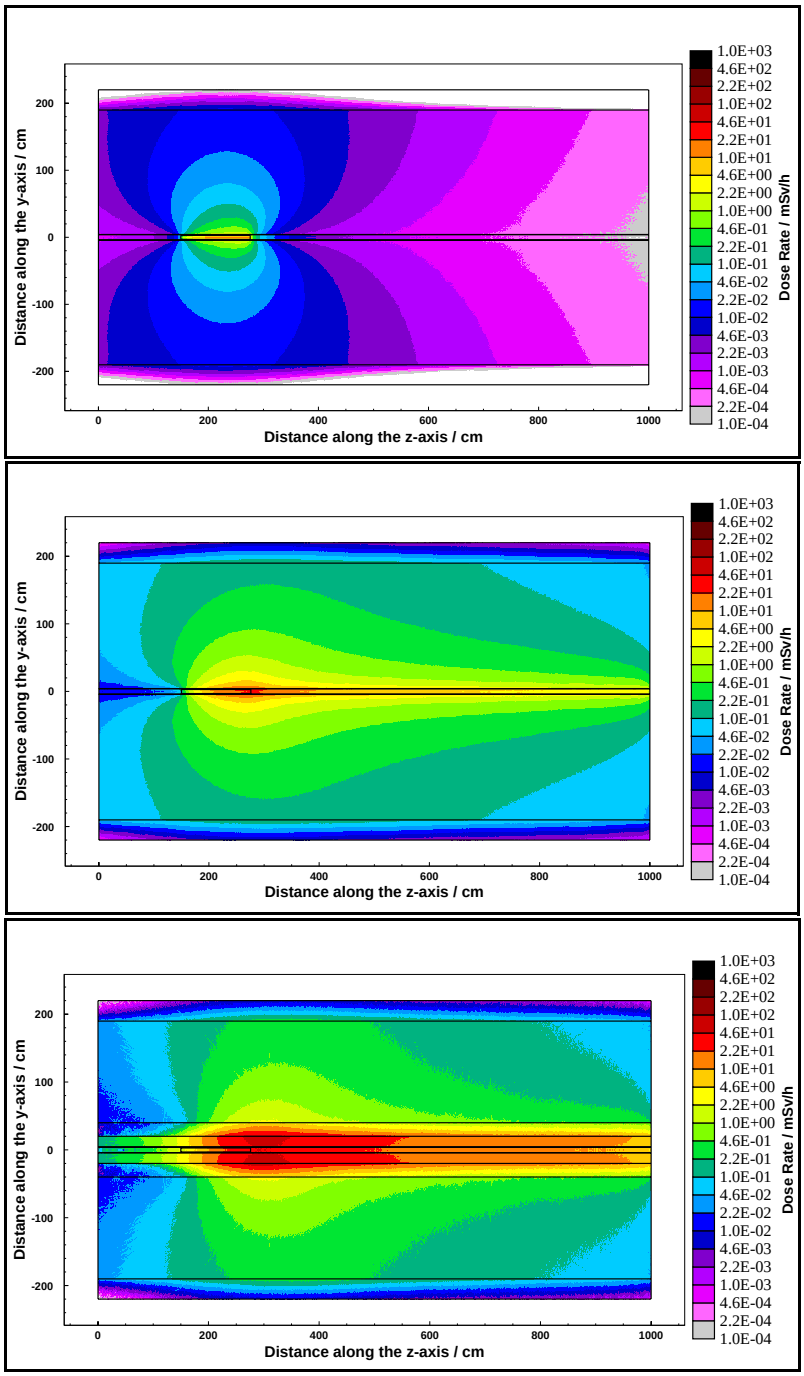

Figure 6.9: Dose rate distributions showing the various contributions coming from the carbon collimator (a) the copper beam pipe (b) and the iron shield (c).

As can be clearly seen the shield significantly contributes to the dose rates in the aisle, explained by the fact that due to secondary high-energy interactions a significant cascade only fully develops inside the iron shield.

Figures 6.9 and 6.10 show separately the different contributions to the total dose rate distribution for the carbon composite collimator, the beam pipe as well as the iron shield and the tunnel wall.

As compared to the collimator the copper beam pipe dominates the dose rates in the unshielded case. The 20 cm iron shielding attenuates the radiation emitted from the activated pipe and the collimator by diminishing the dose rate by roughly an order of magnitude. However, when comparing the contribution of the shield (see Figure 6.9 c) to the one of the concrete wall (see Figure 6.10 b) it becomes evident that the latter is the main source after 1 day of cooling.

a)

b)

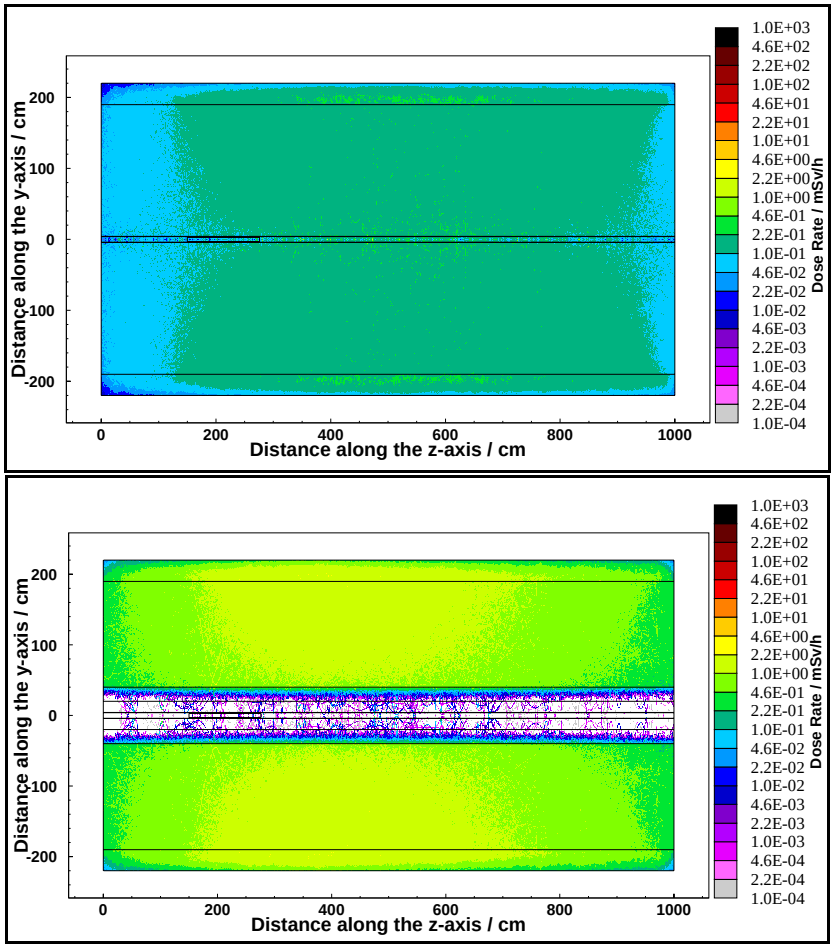

Figure 6.10: Dose rates from the tunnel wall for the unshielded (a) and the shielded case (b).

In fact it appears, that only due to the presence of the shield the tunnel wall becomes significantly activated, which can be explained by the fact that in concrete for cooling times of less than three days, ^{24}Na dominates the activation. This isotope is produced mainly by low-energy neutron capture on ^{23}Na. As the iron shield softens the neutron spectrum the ^{24}Na production in the wall is increasing. Furthermore, not only the total dose rate depends on the cooling time but also the relative contributions from the various activated components. For an example location in the centre of the aisle with values longitudinally averaged along the shower development, this is shown in Figure 6.11. The graph shows remanent dose rates in mSv/h as a function of cooling time for the various dose rate contributors. Values are given separately for

the collimator, the beam pipe, the shield and the tunnel wall, the latter for two cases - shielded and unshielded.

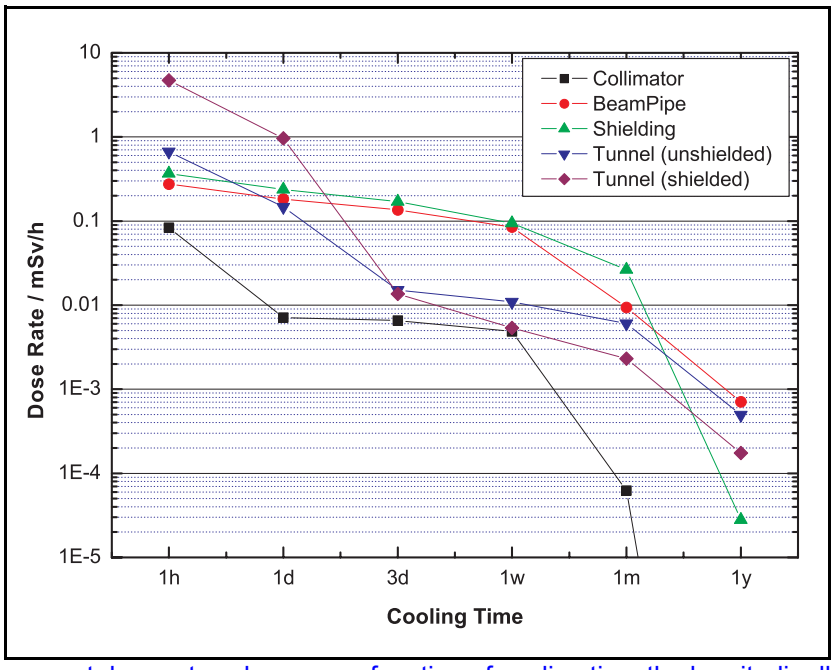

Figure 6.11: Remanent dose rates shown as a function of cooling time the longitudinally averaged dose rate contributors, such as the collimator, the beam pipe, the shield and the tunnel wall. As for the tunnel wall two curves are shown one for the shielded and one for the unshielded case, whereas other contributions were taken from the unshielded scenario.

It can be clearly seen that for short cooling times dose rates in the aisle are dominated by the tunnel or are at least of the same order as the contribution from the shield. It should be noted that the contribution from the tunnel wall is a factor of six to seven larger in the shielded case as compared to the unshielded scenario. For longer cooling times the dose rate is dominated by the ferrous materials, the shielding (iron) and the beam pipe (copper). Please note that in case of copper and cooling times up to 20 hours beta emitters are the dominant source to the remanent dose rate (see also Figure 5.17 in Section 5.3.3), hence contributing most to the calculated dose rate.

6.3.3 Comparison of ω-Factor Method and Explicit Approach

Having discussed in detail the performed dose rate calculations based on the two sets of ω-factors and with the explicit simulation approach it might now be interesting to compare the results to each other. In particular, the modern ω-factor method is chosen as it should give the more reliable results of the two ω-factor based approaches.

Figure 6.12 shows remanent dose rates on contact to the inside of the iron shield. Values are given for the explicit simulation as well as the modern ω-factor approach, whereby significant differences can be observed. Please note that for the detailed simulation of isotope production, as well as for the subsequent sampling of radioactive isotopes and their daughter products only the shielding was considered. In case of the outer surface of the shield the remanent dose rates calculated with the method using ω-factors and the explicit simulation agree within the errors (see Figure 6.13). As discussed in Section 5.3.3 induced activity in iron is dominated by gamma emitters, thus in principle one expects the omega approach to agree rather well with the results from the explicit simulation. Observed differences on the inside of the shield can be explained by the inherently conservative assumptions as referring to a uniformly irradiated plane and also to the lateral activation of the iron shield. However, it should be noted that due to the inhomogenious irradiated shield (*e.g.,* comparing the inside and the outside surfaces) the with

the ω-approach obtained results significantly depend on the lateral bin size used to calculate the star density distribution, also supported by the results as shown in Table 5.15.

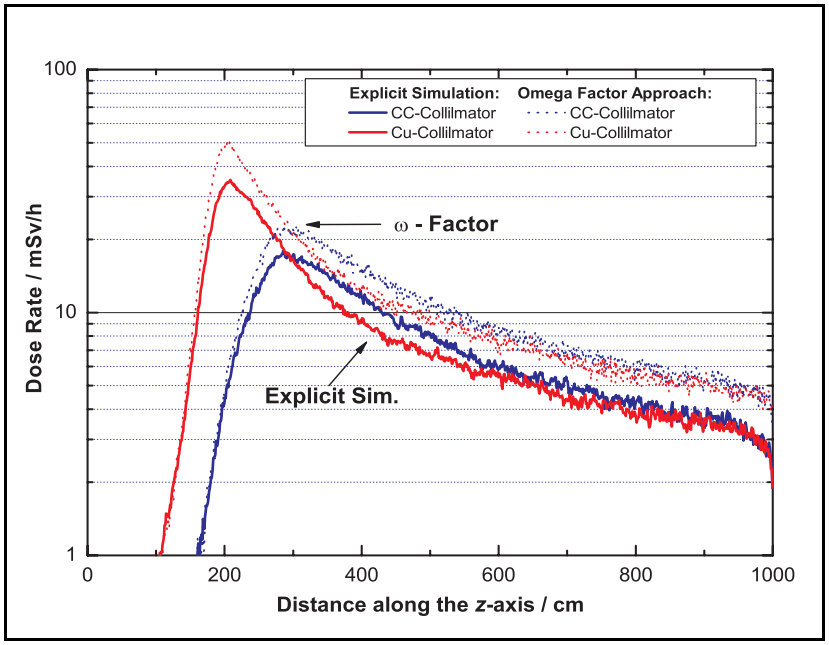

Figure 6.12: Remanent dose rates along the inside of the iron shield as calculated with the ω–factor approach (dotted lines) with the explicit simulation method (solid lines), for carbon composite and copper collimators.

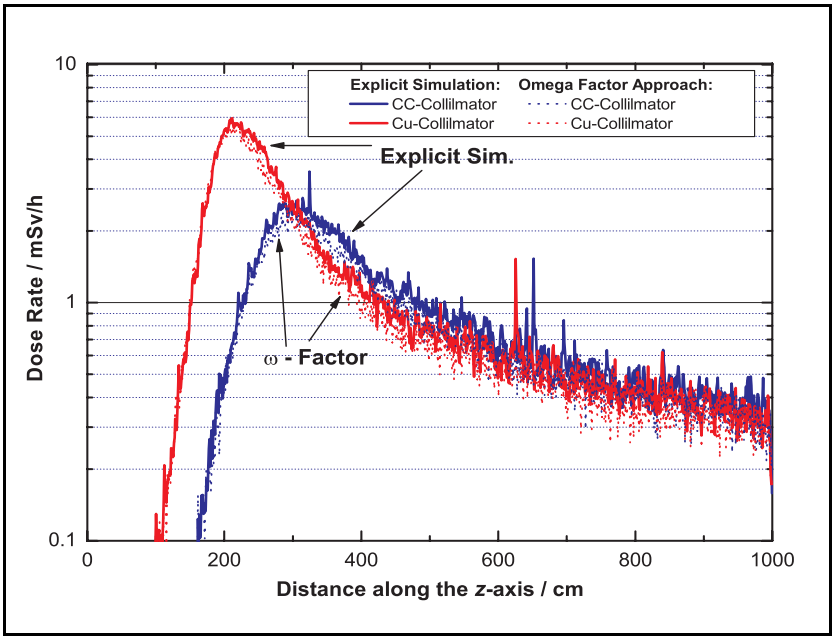

Figure 6.13: Remanent dose rates along the outside of the iron shield as calculated with the ω–factor approach (dotted lines) with the explicit simulation method (solid lines), for carbon composite and copper collimators.

In addition, Figure 6.14 shows contact dose rates alongside the beam pipe calculated with the explicit simulation and compared to the results obtained using the modern ω-factor approach. Here, remanent dose rates show larger differences, as expected due to the much smaller size of the beam pipe. In addition, the results would show even larger differences in case of longer cooling time, since in the case of a cooling time of one day, dose rates caused by positron

emitters are still dominant. These two comparisons clearly show the large uncertainties which are inherent for all ω-factor approaches.

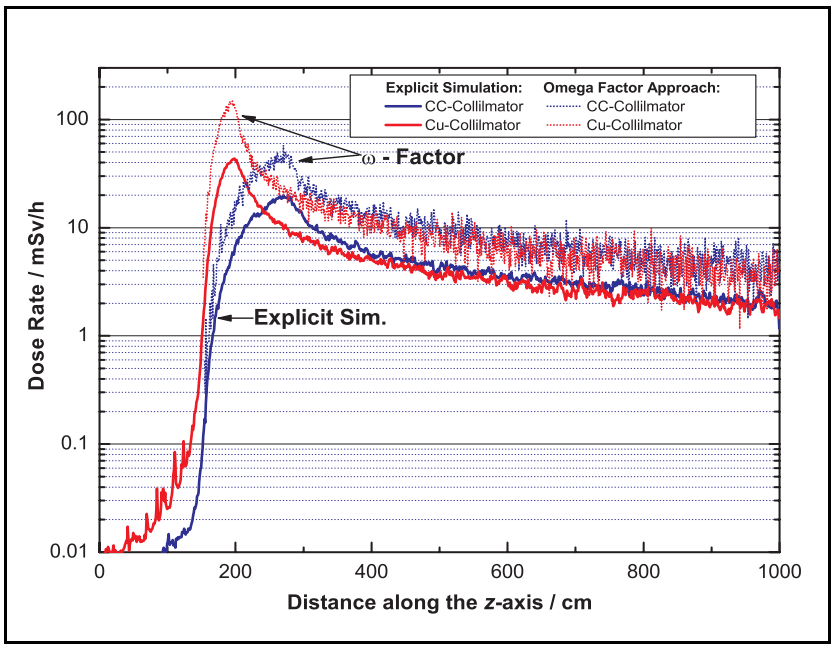

Figure 6.14: Remanent dose rates along the copper beam pipe as calculated with the ω–factor approach (dotted lines) with the explicit simulation method (solid lines), for carbon composite and copper collimators.

As already shown in Figures 6.9 and 6.10 beside the tunnel wall the shield will be an important source for remanent dose rates. Unlike in case of the tunnel, due to different dominant isotopes, remanent dose rates are persistent over a longer time, therefore being an important aspect for the design of the installation. In order to compare the effect of the shield in case of different collimator materials, Figure 6.15 shows remanent dose rates in the aisle of the tunnel, laterally in the centre between the shield and the tunnel wall. Please note that all results refer to 180 days of irradiation and one day of cooling.

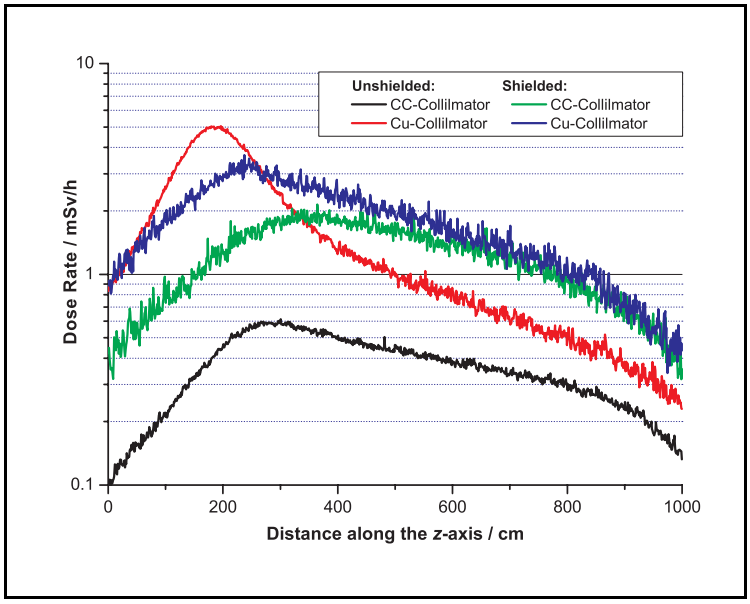

Figure 6.15: Remanent dose rates in the aisle of the tunnel for the shielded and unshielded scenario as well as for two different collimator materials - copper and carbon composite.

As can be seen, in case of copper (red and blue line) at least for the maximum values the remanent dose rate is reduced in the shielded case, whereas the case of a carbon composite

collimator shows an opposite behaviour. However, for various cooling times different isotopes become dominant, thus influencing the respective maximum remanent dose rates as shown in Figure 6.16.

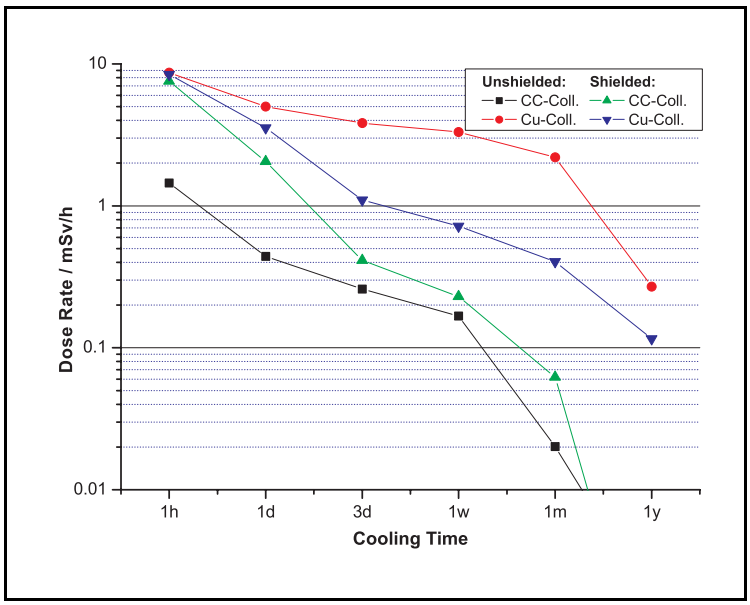

Figure 6.16: Maximum remanent dose rates in the aisle of the tunnel as a function of cooling time. Values are shown separately for the shielded and unshielded scenario as well as for two different collimator materials - copper and carbon composite.

In case of copper the effect of the shield clearly leads to significantly lower dose rates after several days of cooling. However, in case of carbon composite, an inverse behaviour is observed where the shield leads to higher dose rates in the aisle, especially during the first three days after the irradiation.

Summarizing, obtained remanent dose rates using calculated star densities followed by a folding with ω-factors tend to overestimate dose rates to be expected at contact with the respective object. Thorough studies comparing results for various cooling times and arbitrary locations are only possible using the explicit method. During possible interventions, given the fact of complex work patterns, contact dose rates are only of minor importance. During both phases the design of the installation, as well as for later maintenance planning realistic remanent dose rates at various work locations are of utmost importance.

Therefore, in the following, although based on the very simplified collimator layout, an example is given to obtain integrated doses to personnel, received during a possible repair intervention at the collimator.

6.3.4 Example for Intervention Dose Estimate

Based on the remanent dose rates calculated for the simplified layout it is possible to estimate the total dose which might be received by personnel during a repair intervention on a collimator. Obviously, since a prototype collimator has not yet been designed and built, any intervention scenario is merely an educated guess. However, emphasis in this study is put on the demonstration of the method for estimating job-doses rather than on the accuracy of the actual scenario and obtained doses which are thus only of secondary importance.

The intervention was assumed to consist of the following parts:

- **(i)** access to the intervention place (walking speed: 1 m/s) which was assumed to be at the other end of the insertion (*i.e.,* 500 m, worst case for IP3)
- **(ii)** opening of the shield,
- **(iii)** replacement of a collimator,
- **(iv)** closing of the shield, and
- **(v)** walking back to the exit.

The time needed to replace the collimator (dismanteling and mounting of flanges or connectors, handling of additional vacuum flanges, the motor, the cooling circuit and the electricity) was estimated with two hours. The opening and closing of the shield was assumed to take about 15 minutes each.

Note that the FLUKA results are based on the assumption that the annual loss is concentrated at one collimator. Thus, the dose rate which would be received during the passage of the cleaning insertion is equal to the dose which is received “by passing through” the 10 m section at the same speed. Furthermore, it might be reasonable to assume that the part of the shield, which is removed, is stored during the intervention such that it does not contribute to the dose received during the replacement of the collimator.

In a first step, dose rates are determined for the various parts of the intervention. These dose rates are then multiplied in a second step with the respective durations of the intervention parts and with a more realistic annual loss at the collimator. The dose rates for the various parts of the intervention were calculated for the following locations:

- **(i)** total dose rate at the centre of the aisle,
- **(ii)** total dose rate in the aisle at 30.5cm to the outer surface of the shield averaged with the same contribution for the inner shield surface at 19.5 cm (conservative assumption!),
- **(iii)** dose rate from the collimator and pipe at 30.5cm distance plus dose rate from the inside of the shield remaining in place plus dose rate from the wall taken at the centre of the aisle,
- **(iv)** as in (ii),
- **(v)** as in (i)

and are given for the unshielded and shielded scenarios in Table 6.5. Of course in the former case part (ii) and (iv) are not applicable. Please note that calculated remanent dose rates from the shield were divided by a factor of two, assuming that the removed shield is temporarily

stored at a significant distance. However, during the process of opening the shield both parts - inside and outside - are assumed to contribute equally.

Table 6.5: Remanent dose rates in mSv/h for two different cooling times applicable to the various parts of the intervention. Results are shown for two different collimator materials - carbon composite and copper - separately for the shielded and unshielded scenarios.

Contribution	Sources	Cooling Time	Collimator Design			
			CC unsh.	CC sh.	Cu unsh.	Cu sh.
Access (2-ways)	All	1h	1.1	5.1	3.2	4.5
Opening of the Shield	All	1h	-	39.7	-	75.5
Intervention	Collimator	1h	2.2	2.2	44.6	44.6
	Pipe	1h	2.8	2.8	4.6	4.6
	Shield	1h	-	38.7	-	73.7
	Tunnel	1h	0.7	4.7	1.5	4.0
Closing of the Shield	All	1h	-	39.7	-	75.5
Access (2-ways)	All	1d	0.35	1.5	1.1	1.8
Opening of the Shield	All	1d	-	26.3	-	47.3
Intervention	Collimator	1d	0.2	0.2	29.7	29.7
	Pipe	1d	1.9	1.9	2.9	2.9
	Shield	1d	-	25.7	-	46.2
	Tunnel	1d	0.2	1.0	0.5	1.4
Closing of the Shield	All	1d	-	26.3	-	47.3

A realistic estimate for the total annual loss at one collimator is based on the following assumptions. Although around 80 % of the total loss will occur in the primary collimators, at least in case of Point 7 (four primary collimators) due to the alternating skew angels (*i.e.,* their shifted angular positioning) the cascade will not fully develop inside the collimators but further downstream. However, due to the missing final design and respective detailed loss calculations, for the moment it is assumed that the loss distribution will not significantly change. In addition, in case of the betatron cleaning the primary collimators are expected to be close together, hence all of them contribute at the same time to the dose rate at this location. Therefore, for the primary collimators a conservative scaling of 50 % is assumed (later referred to as scaling factor S1). For the secondary collimators given the loss distribution as listed in Table 6.1, for the present calculation an overall scaling factor of twenty (referring to a maximum loss fraction of 5 %) is assumed (later referred to as scaling factor S2). In addition, a comparison between a more realistic layout (see Section 6.4) and the simplified scenario has shown that due to the aperture between the jaws the calculated dose rate is smaller by a factor of two (later referred to as scaling factor S3).

In the following the proposed scaling factors and the given intervention times are applied to two different cases: a replacement of primary (see Table 6.6) or secondary (see Table 6.7)

collimator. In addition, results are separately shown for two different cooling times of one hour and one day, respectively.

Table 6.6: Partial and total ambient dose equivalent as received per person and intervention on a primary collimator. Please note that values are given in mSv and refer to the respective cooling time as stated in column two.

Contribution	Cooling Time	Time per Intervention	Scaling Factors	Collimator Design			
				CC unsh.	CC sh.	Cu unsh.	Cu sh.
Access (2-ways)	1h	500 s	-	0.15	0.71	0.44	0.63
Opening of the Shield	1h	15 min	S1, S3	-	2.42	-	4.61
Intervention	1h	1h	S1, S3	1.90	12.10	16.90	31.70
Closing of the Shield	1h	15 min	S1, S3	-	2.42	-	4.61
Sum				**2.05**	**17.65**	**17.34**	**41.55**
Access (2-ways)	1d	500 s	-	0.05	0.21	0.15	0.25
Opening of the Shield	1d	15 min	S1, S3	-	1.64	-	2.96
Intervention	1d	1h	S1, S3	0.77	7.20	11.03	20.05
Closing of the Shield	1d	15 min	S1, S3	-	1.64	-	2.96
Sum				**0.82**	**10.69**	**11.18**	**26.22**

Table 6.7: Partial and total ambient dose equivalent as received per person and intervention on a secondary collimator. Please note that values are given in mSv and refer to the respective cooling time as stated in column two.

Contribution	Cooling Time	Time per Intervention	Scaling Factors	Collimator Design			
				CC unsh.	CC sh.	Cu unsh.	Cu sh.
Access (2-ways)	1h	500 s	-	0.15	0.71	0.44	0.63
Opening of the Shield	1h	15 min	S2, S3	-	0.24	-	0.46
Intervention	1h	1h	S2, S3	0.19	1.21	1.69	3.17
Closing of the Shield	1h	15 min	S2, S3	-	0.24	-	0.46
Sum				**0.34**	**2.4**	**2.13**	**4.72**
Access (2-ways)	1d	500 s	-	0.05	0.21	0.15	0.25
Opening of the Shield	1d	15 min	S2, S3	-	0.16	-	0.30
Intervention	1d	1h	S2, S3	0.08	0.72	1.10	2.01
Closing of the Shield	1d	15 min	S2, S3	-	0.16	-	0.30
Sum				**0.13**	**1.25**	**1.25**	**2.86**

The results obtained with the simplified scenario already show that interventions at collimators are rather critical, especially in case of primary collimators and after short cooling times.

In addition it should be noted, that such careful studies regarding maintenance are only possible using the explicit simulation approach. With simplified scenarios as described here, estimates can be carried out already during the design phase of the machine, hence pointing out critical regions as fast as possible. However, for a correct assessment of doses to personnel received during an intervention it is absolutely necessary to adapt the degree of simplification to the particular case of interest. This is shown in the following for a particular critical situation at Point 3, where collimators will be installed in a narrow region between two quadrupole modules as well as close to vacuum equipment.

6.4 Remanent Dose Rates - Realistic Layout

For the warm part of the long straight section about 1200 vacuum chambers [118] and in total 1800 bellow modules have to be installed. Furthermore 500 ion pumps will maintain the beam vacuum, many of them being placed close to collimators and quadrupoles. New layout and optics versions so far prevent the completion of the mechanical integration, which hinders or blocks the final design of components that rely on the input from the mechanical integration.

Expected remanent dose rates are only partially known, some of which based on designs having already become obsolete. This is especially the case in critical regions where collimators, quadrupoles and vacuum pumps have to be installed close together. Earlier estimates rely on the ω-factor approach and are thus only valid at contact to and along the surface of the shield. As mentioned above, the calculations were performed with the MARS particle interaction and transport code and are based on two different versions of the LHC machine layout, Version 6.2 for Point 3 and Version 5.0 for Point 7, respectively. They include a detailed description of the beamline components and assume iron shielding over the whole insertions length of 538 m - details can be found in Section 6.2 as well as in Refs. [110] and [119].

So far, generic studies using the explicit approach to determine remanent dose rates have shown that values in the order of several mSv/h may be reached close to the collimators and quadrupoles (see Section 6.3). In case of failures, either in the collimation or the vacuum system, maintenance and repair will have to be performed (*e.g.,* recovery of vacuum or leak detection). In order to estimate the dose to personnel for a typical example of an intervention on the vacuum system a section of the beamline was modelled and simulated in detail with FLUKA.

6.4.1 Description of the Geometry

The geometry was implemented according to the latest available layout for the Q4 quadrupole in IP3 (see Figure 6.1). The FLUKA geometry (created with the ALIFE geometry editor [120]) includes two secondary collimators (TCS2, TCS3), one downstream quadrupole magnet as well as various flanges connecting the beam pipe to beamline components such as vacuum pumps (see Figure 6.17). All elements were implemented in detail, accounting for the exact dimensions as well as their respective materials, carbon composite for the collimator, copper for the beam pipe, stainless steel for flanges and bellow models, as well as additional materials used for the magnet or the pump. The geometry of the 11 meter long section is described in a right-handed orthogonal system with its origin defined to be on the beam axis and 2.5 m

upstream of the front face of the first collimator. The *x*-axis is pointing up and the *z*-axis parallel to the beam axis is centred between the two vacuum chambers.

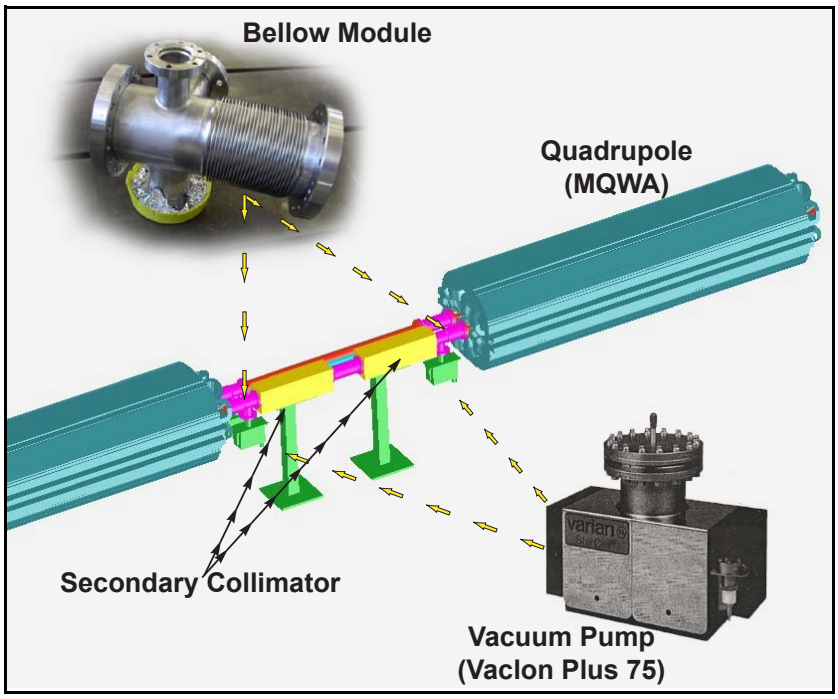

Figure 6.17: Three dimensional descriptive representation of the implemented geometry including quadrupoles, collimators and the vacuum pumps.

The secondary collimators were implemented with a length of 126 cm, based on the collimation design presently under discussion, which assumes carbon composites instead of copper as collimator material. Furthermore, although the expected length for each collimator jaw is 100 cm, in this study the length was chosen to correspond to the same total hadronic interaction length as for the copper collimator used in earlier studies. On both ends of the collimators bellow modules are used as connectors. Those between the collimator vessel and the adjacent magnet connect the vacuum pump to the vacuum chamber. For the vacuum pump the dimensions, the weight as well as the materials correspond to the technical specification of the type “Vaclon Plus 75".

6.4.2 Calculation of Remanent Dose Rates

The geometry includes numerous regions, different in volume material and shape. Especially, between the tunnel wall, the quadrupole and installations close to the collimators huge volume differences exist. During the first part of the simulation, which determines the isotope production, this would result in isotopes being more frequently stored for bigger volumes, as mainly for the tunnel wall and the iron yoke. As already described for the simplified case, this may then lead in the second part of the simulation to an insufficient sampling of isotopes in critical regions of particular interest for this study, *e.g.,* the bellow module or the pump. Thus, for statistical purpose the isotope production was calculated separately for the beamline installations (collimators, bellow modules, beam pipe), the magnet and for the tunnel structure. Likewise, separate calculations were performed for the second pure electromagnetic simulation. Finally, in a post-processing step these results were added to obtain dose equivalent rates in a three dimensional mesh for any location within the 11 m long tunnel section. Please note that all results are normalized to the annual loss at the two secondary collimators (TCS2, TCS3), as calculated for the optics version 6.2 (see Table 6.1). For TCS2 and TCS3 at Point 3 this adds to 13.2 % of the total annual loss of 1.0×10^{16} per collimation region and ring, thus 1.32×10^{15} protons. If not stated differently the cooling time refers to one hour after the end of 180 days of operation.

Dose rates around collimators not only depend strongly on the cooling time but also on the location with respect to the main contributing sources, the collimators within their vessels and possible downstream installations. Figure 6.18 shows a horizontal cut through the geometry. Visible are the two beampipes, the two collimators, various flanges and the quadrupole superimposed on the remanent dose rate distribution. The calculated dose rates vary strongly

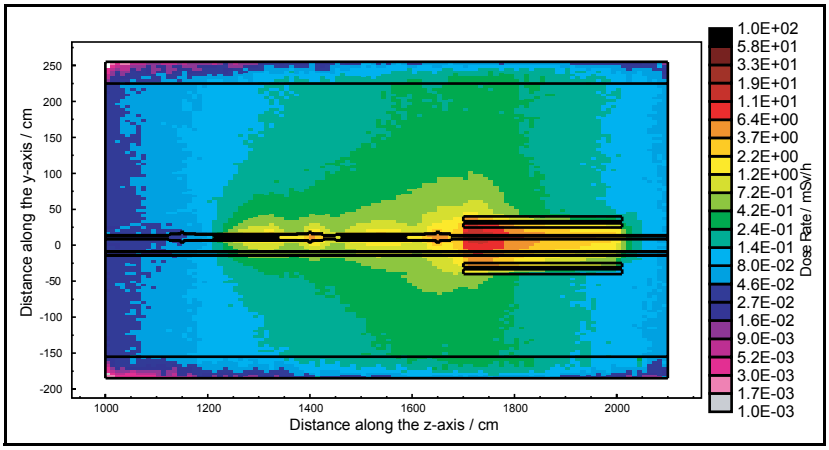

Figure 6.18: Remanent dose rate distribution for a horizontal projection of the geometry along the *z*-axis.

depending on the location ranging from μSv up to several mSv. Figure 6.19 shows a vertical projection of the left beam line with the collimators and pumps.

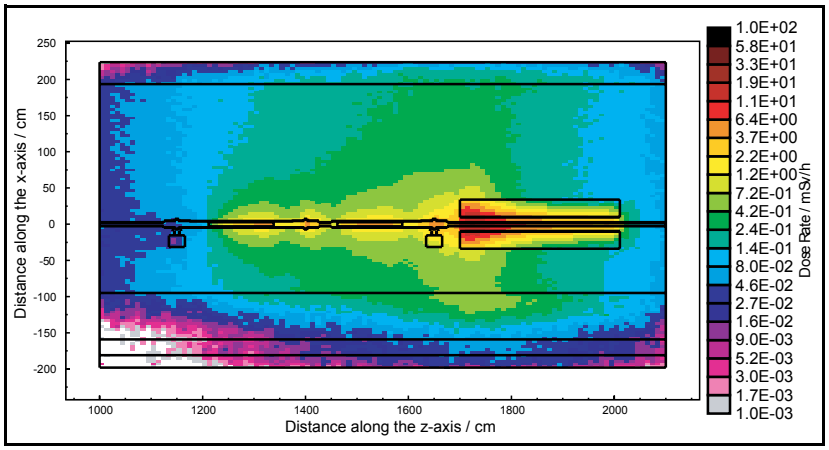

Figure 6.19: Remanent dose rate distribution for vertical projection of the geometry along the *z*-axis.

The two collimators and the magnet clearly dominate the dose rate at this particular cooling time of one hour, leading to peak values on contact to the surface of the quadrupole in the order of 10 mSv/h. The dose rates close to the front face of the quadrupole are shown in Figure 6.20, characterized by a rather uniform distribution with values of several mSv close to the copper coils and the yoke. During maintenance the magnet may not have to be directly touched,

however work, necessary to be carried out adjacent to the magnets will certainly have to be minimised.

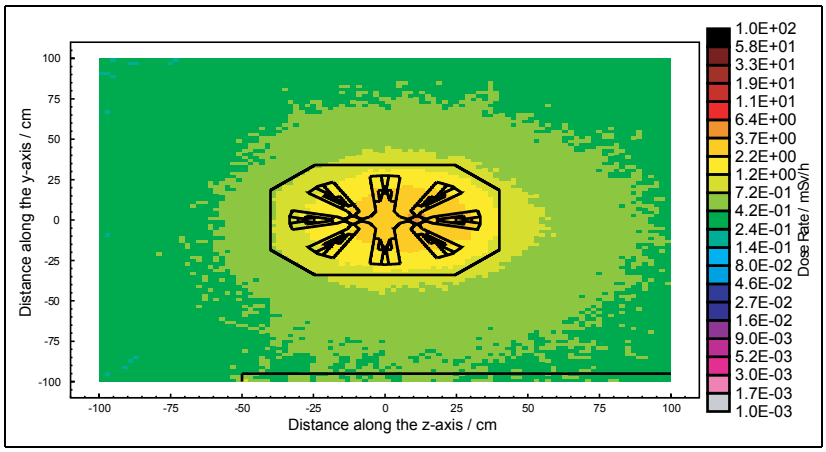

Figure 6.20: Remanent dose rate distribution for a lateral cut through the beam pipes directly in front of the downstream magnet.

In order to assess possible intervention scenarios, in the following graphs of calculated remanent dose rates are shown for locations and cooling times typical for vacuum maintenance work. As for the cooling time, one hour is certainly a conservative assumption for interventions necessary as fast as possible after operation (*e.g.,* due to a failure of the collimator) and one day is assumed to be a reasonable estimate for soon but not immediately needed interventions. Furthermore, one month and four month have been selected for typical intervention scenarios, the latter being at the end of the yearly shutdown when maintenance work should be performed in high radioactive regions. Additionally, results are given for year of cooling to indicate the further behaviour of the decay without additional buildup.

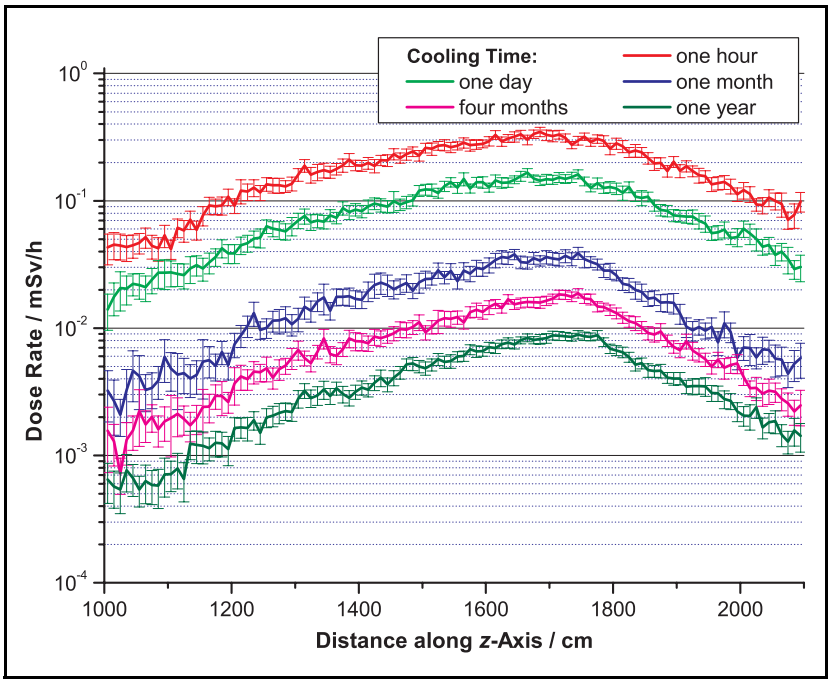

Figure 6.21: Remanent dose rates in the aisle for various cooling times, shown as a function of distance along the beam axis.

Figure 6.21 shows the dose rates in the aisle along the 11 m long section for various cooling times. Values were calculated for a distance of 133 cm from the centre of the two beam pipes, corresponding to approximately 1 m distance from the outer beam pipe carrying the two collimators and pumps (see Figure 6.18, y = 133 cm).

After one hour and one day maximum remanent dose rates can be expected to be of the order of 0.4 and 0.2 mSv/h, respectively. Please note that dose rates are dominated by the ^{24}Na contribution from the tunnel wall (see Section 6.3.2). During maintenance, work has to be carried out close to the beam pipe and nearby installed equipment. For example, at a lateral distance of 33 cm lateral to the centre between the two beam pipes, *i.e.,* approximately 20 cm separated to the outer beam pipe, dose rates of the order of 1 mSv are reached, as shown in the longitudinal distribution in Figure 6.22.

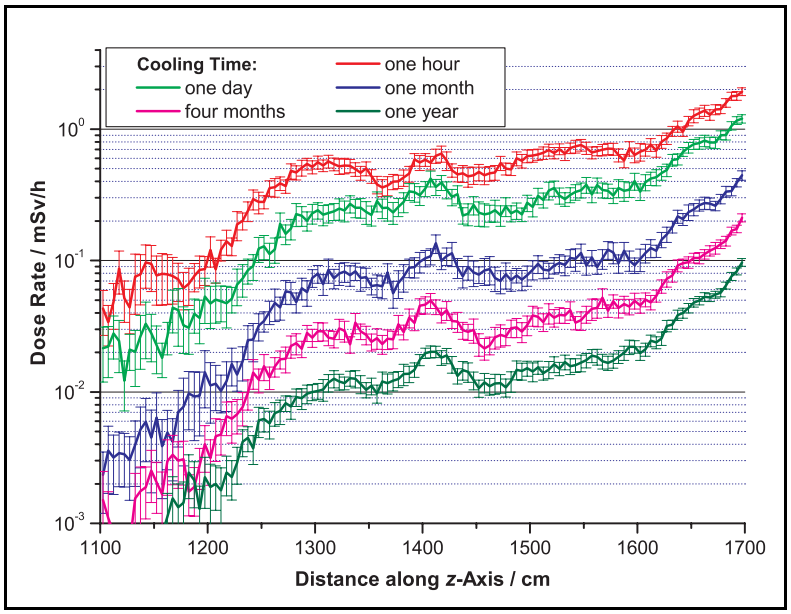

Figure 6.22: Remanent dose rates close to the outer beam pipe for various cooling times, shown as a function of distance along the beam axis.

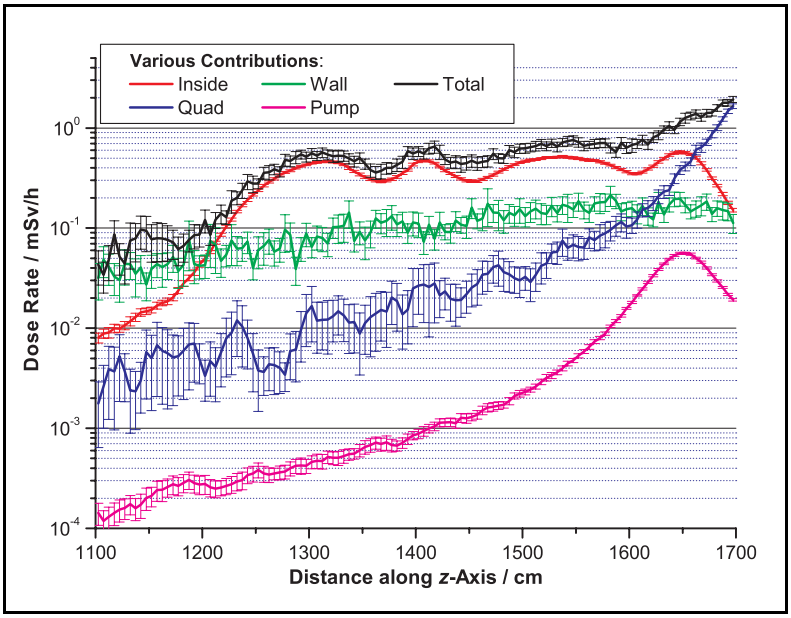

Figure 6.23: Different contributions to the remanent dose rates close to the outer beam pipe (y = 33 cm). Values are shown as a function of distance along the beam axis and for a cooling time of one hour.

In order to illustrate the various dominant sources along the beamline Figure 6.23 shows separately the contributions from the tunnel wall, the quadrupole as well as from the other beamline components (“Inside”) like the collimators, the beam pipe, the flanges and the vacuum pump. Please note that the latter is shown separately, since it is also included in the “Inside” graph.

The opening of flanges close to bellow modules and the vacuum pump might be time-consuming in case of difficult handling due to space restrictions. Close to the bellow module and the pump, remanent dose rates are dominated by the flange and the adjacent quadrupole. Therefore, to illustrate the lateral dependence at this critical location in Figure 6.24 dose rate values for various cooling times are shown as a function of distances to the *z*-axis.

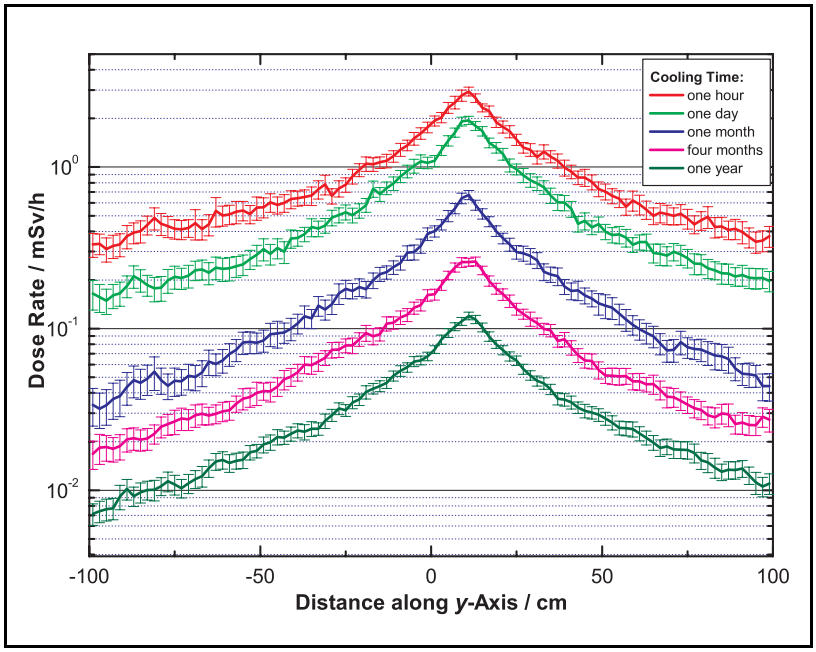

Figure 6.24: Remanent dose rates at the longitudinal location of the downstream bellow module and the vacuum pump (z = 1660 cm). Results are shown as a function of distance along the beam axis and for various cooling times.

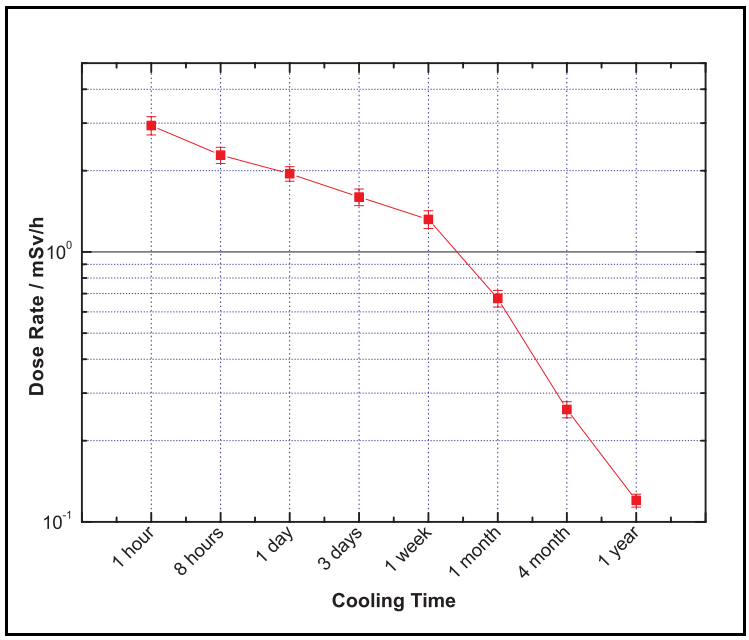

Figure 6.25: Maximum dose rate values at the lateral location of the downstream vacuum pump (see Figure 6.24) as a function of cooling time.

As can be seen, high dose rates of several mSv/h are only reached close to the installations, whereas at a distance of 75 cm remanent dose rates can already be expected to be lower by an order of magnitude. However, due to the materials being used for the equipment (*e.g.,* copper, iron) with respect to the cooling time a comparable decrease is foremost reached 4 months after the end of operation (see Figure 6.25).

To summarize, remanent dose rates are significant but not prohibitive for maintenance work. Based on the results obtained for remanent dose rates in different locations and for various cooling times a thorough estimation of dose to personnel is possible, as given in the following based on an example for an intervention at the vacuum pump.

6.4.3 Planning for an Example Vacuum Intervention

Collective doses accumulated during an intervention on the vacuum system depend on many parameters, thus answers being valid across the board are not possible to give. Affecting parameters are manifold *e.g.,* total intervention time, number of persons involved, type of work and the location with respect to the dominant radiation sources. However, experiences from the SPS can be used in order to select a critical invention, consisting of intensive leak detection and consecutive in situ repair.

For this example dose rates were calculated for several cooling times. The intervention was subdivided into several parts, *e.g.,* the access to the critical region, the leak detection and the repair. For each particular part of the intervention the corresponding dose rates were determined as taken from Figures 6.21 to 6.24, listed together with their respective cooling time in Table 6.8. For the access to the intervention point (TCS2 and TCS3 in Q4) calculated results for the unshielded scenario were taken from Section 6.3.2 and interpolated for additional cooling times.

Table 6.8: Remanent dose rates for various cooling times including the various contributions for the respective part of the intervention.

part of work	Location	Remanent Dose Rate / mSv/h							
		1h	8h	1d	3d	1w	1m	4m	1y
Access (2-ways)	in the aisle	0.40	0.28	0.13	0.07	0.05	0.03	0.01	0.01
Leak Detection	close to the pipe (20cm)	0.54	0.36	0.29	0.22	0.17	0.09	0.04	0.02
	larger distance (35 cm)	0.43	0.29	0.23	0.18	0.14	0.07	0.03	0.02
Removal/Reinstallation	Flanges	1.32	0.92	0.80	0.62	0.50	0.26	0.12	0.06
Repair	*e.g.,* Pump	0.35	0.26	0.20	0.14	0.11	0.06	0.02	0.01

Table 6.9: Total dose equivalent received per person for various cooling times for each part of the intervention.

Part of Work	Time per Intervention	Accumulated Dose per Person and Intervention / mSv							
		1h	8h	1d	3d	1w	1m	4m	1y
Access (2-ways)	0.3 hour	0.11	0.08	0.04	0.02	0.01	0.01	0.00	0.00
Leak Detection	2 hours	1.08	0.73	0.58	0.44	0.34	0.18	0.08	0.04
	2 hours	0.86	0.58	0.46	0.36	0.28	0.14	0.06	0.04
Removal/Reinstallation	1 hour	1.32	0.92	0.80	0.62	0.50	0.26	0.12	0.06
Repair	1 hour	0.35	0.26	0.20	0.14	0.11	0.06	0.02	0.01
Sum:	**6.3 hours**	**3.72**	**2.57**	**2.08**	**1.58**	**1.24**	**0.65**	**0.28**	**0.15**

For the leak detection two distances were selected reflecting the typical search pattern. As can be seen in Table 6.8 workers will be exposed to the highest dose rates during the opening of the flanges and the reinstallation of the equipment. For the in situ repair is was assumed that the broken device can be removed from its installation is repaired in the centre of the aisle. Corresponding intervention times were given by [121] and are shown together with their respective dose values in Table 6.9. Please note that all results are given as total ambient dose in mSv received per person and intervention.
The results clearly indicate that any vacuum intervention in this critical region has to be well planned and optimized with respect to working time and methods. In order to avoid unnecessary exposure of personnel, if possible, periods towards the end of the shutdown, *i.e.,* a cooling time in the order of four months, should be used for time-consuming interventions. It should be noted, that such detailed estimates have only become possible with the new explicit simulation approach. They can be carried out already during the design phase of the machine, hence allowing for proper adaptation of the layout of critical region. In fact, during the current finalisation of the layout and in order to account for the needs for vacuum interventions larger distances are envisaged between the various quadrupole modules. This would diminish the dose rate contribution from the downstream magnet, simplify the opening of the flanges and therefore certainly lower the accumulated doses.

6.5 Air Activation and Ventilation

This section describes the calculations carried out to estimate the release of radioactivity in air produced in the two collimation insertions of the LHC. In particular, air activation was calculated using a simplified geometrical model of the cleaning insertion and various scenarios, which included different collimator materials and lengths. The validity of the approach is demonstrated by comparing the results to those of earlier studies [110, 114] based on more detailed, although now obsolete layouts of the cleaning insertions.

As mentioned in Section 4.2.2, 39 different radionuclides are considered, while their production was estimated from the hadron track-length distributions in the air volumes along the beam cleaning insertions and evaluated isotope production cross-sections. The specific activity released at the surface has been estimated using a laminar flow model.

6.5.1 Description of the Geometry

As already discussed in Section 6.2.3, results for air activation exist for both beam cleaning insertions, however, based on two different versions of the LHC machine layout, Version 6.2 for Point 3 and Version 5.0 for Point 7, respectively. The calculations were performed with the MARS particle interaction and transport code including a detailed description of the beamline components of the whole insertions. Details can be found in Section 6.2 as well as in Refs. [110] and [119]. In the following, the results of the parametric study will be compared to the specific activities predicted by these two simulations.

The simplified geometric model of the beam cleaning insertions is based on the assumption that the activation of air caused by one primary proton lost in a collimator is mainly determined by the collimator itself and by the layout of the nearby shielding and (downstream) beamline elements. Other beamline components, usually located at rather large distance, are typically shadowed by those close to the collimator and therefore give only minimal contributions to the air activation. The simplified approach is also motivated by the fact that detailed simulations for different collimator materials and lengths would have been too time-consuming and not necessary for a study of only relative changes in air activation, *i.e.,* which is not aiming at accurately predicting absolute values.

Thus, the simplified FLUKA geometry (created with the ALIFE geometry editor [120]) for the parametric study includes only one collimator, two downstream quadrupole magnets as well as various flanges connecting the vacuum pipe to beamline components. These elements were assumed to be located at the entrance to the beam cleaning insertion which was otherwise modelled in its actual length (*i.e.*, 269 m corresponding to one half of the insertion) by an accurate representation of the tunnel wall and floor a vacuum pipe and optional longitudinal iron shielding. Further collimators, magnets, etc., located downstream, as well as the second LHC ring were neglected. The origin of the FLUKA coordinate frame was defined to be on the beam axis, 10 m upstream of the collimator, with the *x*-axis pointing up and the *z*-axis coinciding with the beam. A three-dimensional view is shown in Figure 6.26.

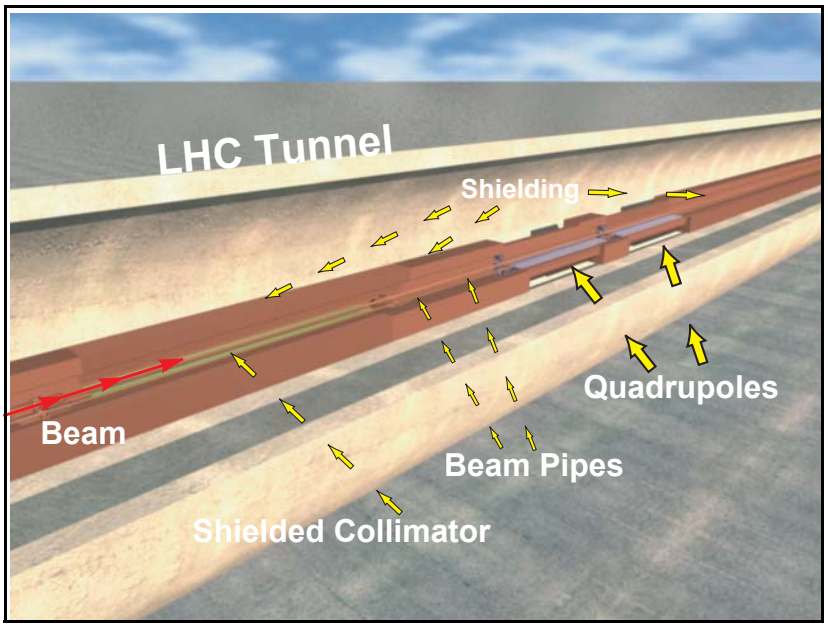

Figure 6.26: Three-dimensional representation of the geometry ('Generic 1').

Two collimator materials were studied, copper and beryllium, as well as two collimator "lengths", in terms of inelastic interaction lengths (λ_I), of 20 λ_I and 10 λ_I, respectively. The former corresponds approximately to the total interaction length of all collimators in the detailed studies for Points 3. The considered configurations are summarised in Table 6.10.

Table 6.10: Different collimator scenarios used for the comparison including the total collimator length expressed also in multiples of the hadronic interaction length (λ_I) for the respective material.

Layout	Optics Version	Material	λ_I / cm	Length / m	Total Length / λ_I
IP3 (MARS)	6.2	Cu	15.1	3.00	~ 20
IP7 (MARS)	5.0	Cu	15.1	8.00	~ 53
Generic 1 (FLUKA)	-	Cu	15.1	3.00	~ 20
Generic 2 (FLUKA)	-	Cu	15.1	1.51	~ 10
Generic 3 (FLUKA)	-	Be	40.7	4.07	~ 10

For each configuration two simulations were performed, with and without a longitudinal iron shield of 20 cm thickness. This reduced shielding thickness - as compared to previous MARS simulations - is motivated by the fact that too complex shielding scenarios may significantly

increase the intervention time in case of maintenance and could, hence lead to unjustified doses to personnel. However, the outer dimensions of the shielding in this study are identical to the ones assumed in the calculations for Point 7.

6.5.2 Calculation of the Isotope Yield

Air activation was calculated according to Equation *(iv)* as defined in Section 4.2.2 by scoring the hadron track-length in all regions of the simplified FLUKA model containing air. In order to be consistent with the cross-section data base [65] used for this analysis a logarithmic energy binning with ten bins per decade was applied with an upper energy limit of 10 TeV. The lower limit for charged hadrons was set to 10 MeV and low-energy neutrons were scored in the 72-group structure of FLUKA. Since the upper bound of the low-energy neutron group structure is 19.6 MeV, 57 logarithmic bins will have a factor width of 1.2593 which is close to $10^{0.1}$ = 1.2589. If region volumes are not specified explicitly, FLUKA returns track-length energy spectra by default. These are added for the various air regions resulting in total track-length spectra for neutrons, protons and charged pions as shown in Figures 6.27, 6.28 and 6.29. For the later comparison the spectra were calculated for the unshielded and shielded layout labelled “Generic 1" as shown in Table 6.10.

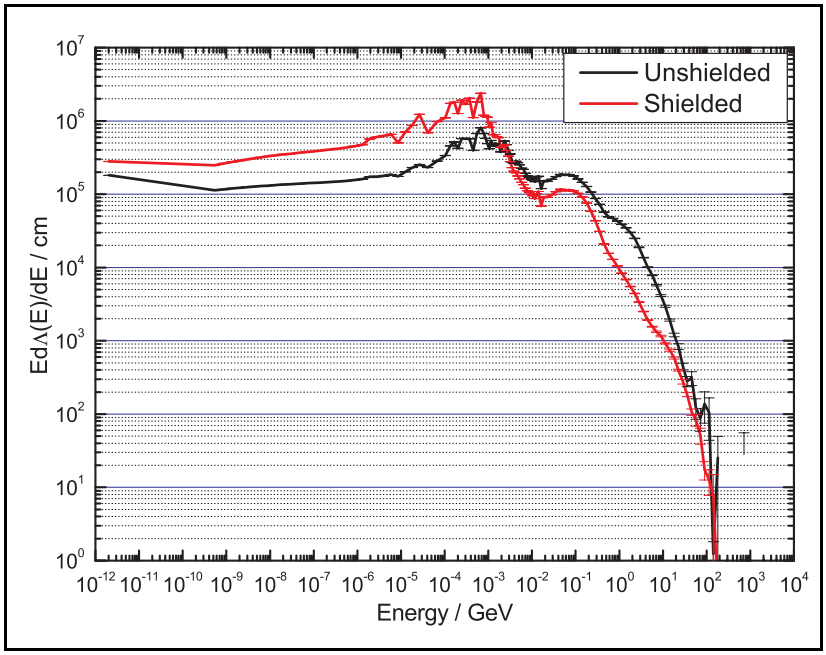

Figure 6.27: Neutron track-length energy spectra for the unshielded and shielded “Generic 1" case.

For neutrons the high-energy part of the spectrum (E > 20 MeV) is lower in the shielded case whereas the low-energy neutron contribution is significantly higher. This can be explained by the fact that in case of shielding high-energy neutrons re-interact in the iron softening significantly the energy spectrum. Isotopes produced by low-energy neutron activation will therefore show a significantly higher yield in the simulation including shielding. On the other

hand, the harder high-energy part of the spectra indicates that for isotopes generated in spallation processes the yield can be expected to be higher in the unshielded case.

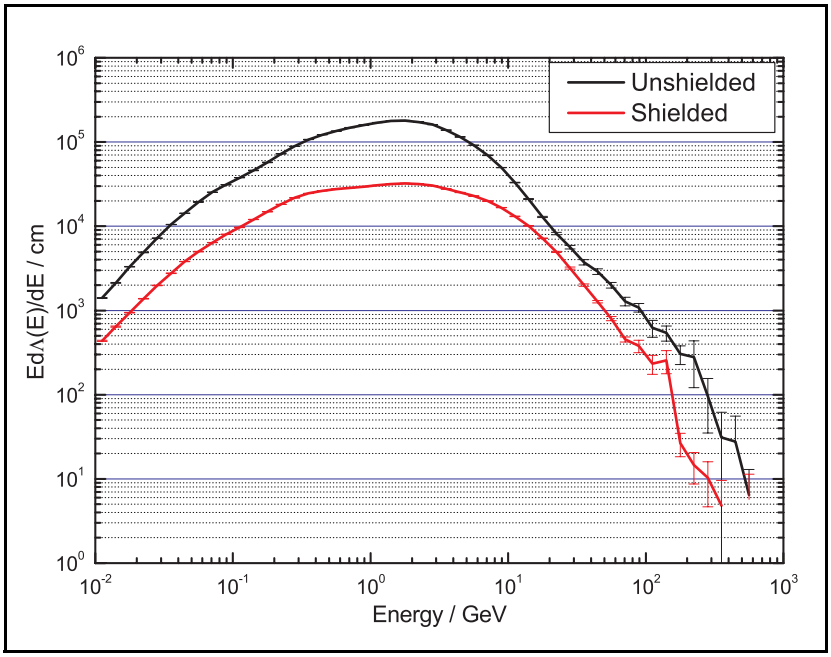

Figure 6.28: Pion track-length energy spectra for the unshielded and shielded "Generic 1" case.

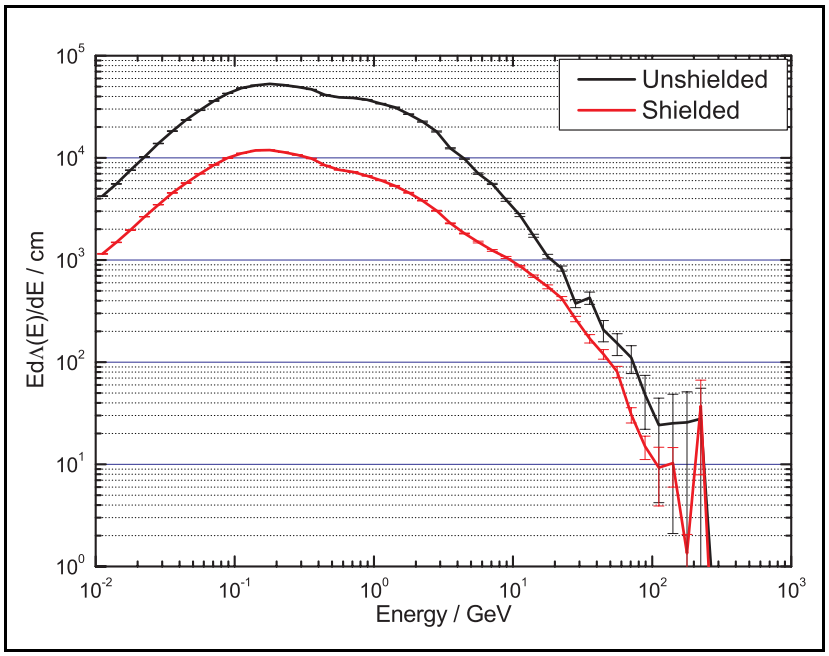

Figure 6.29: Proton track-length energy spectra for the unshielded and shielded “Generic 1" case.

For the calculation of the total production yield per isotope, the integration over energy in Equation *(iv)* in Chapter 4 was replaced by a summation over the energy bins which were used in the track-length scoring.

As a first step, results of the simplified study should be compared to the earlier predictions by detailed MARS simulations for Points 3 and 7 in order to investigate the quality of the approximation. Since in both MARS calculations the beamline was assumed to be surrounded by think iron shielding and the simulations were based on secondary copper collimators they can only be compared to the shielded case of scenario 'Generic 1' (see Table 6.10). It should be noted that the calculations for IP7 included only air activation outside the shield [110] and

can thus only be compared to the activation of equivalent air volumes of the study for IP3 and the 'Generic 1' case. Results for all three cases and the 39 most important isotopes are given in Table 6.11.

Table 6.11: Production of radionuclides in the air of the collimation insertions for three different scenarios. The number of nuclei produced outside the shield per primary proton is compared between the two earlier studies for IP3 and IP7. In addition, results of the new simplified study ('Generic 1') using an equal total collimator length as for IP3 are compared to the latest results for the momentum cleaning insertion and shown in the last column.

Isotopes	Half-life	IP3 (outside)	IP7	Ratio	Generic 1 (outside)		Ratio
		No. of nuc.	No. of nuc.	IP3 / IP7	No. of nuc.	Err. / %	G1 / IP3
^{3}H	12.35 y	$8.05 \cdot 10^{-02}$	$7.10 \cdot 10^{-02}$	1.13	$1.34 \cdot 10^{-01}$	0.17	1.66
^{7}Be	53.3 d	$1.80 \cdot 10^{-02}$	$1.63 \cdot 10^{-02}$	1.11	$2.87 \cdot 10^{-02}$	0.14	1.59
^{10}Be	1.60×10^{6} y	$4.24 \cdot 10^{-02}$	$3.33 \cdot 10^{-02}$	1.27	$7.57 \cdot 10^{-02}$	0.20	1.79
^{11}C	20.38 m	$3.97 \cdot 10^{-02}$	$3.31 \cdot 10^{-02}$	1.20	$6.36 \cdot 10^{-02}$	0.14	1.60
^{14}C	5730.0 y	$1.71 \cdot 10^{+02}$	$1.70 \cdot 10^{+02}$	1.00	$1.85 \cdot 10^{+02}$	0.23	1.09
^{13}N	9.965 m	$8.20 \cdot 10^{-02}$	$6.45 \cdot 10^{-02}$	1.27	$1.39 \cdot 10^{-01}$	0.18	1.70
^{14}O	71.0 s	$2.40 \cdot 10^{-03}$	$1.93 \cdot 10^{-03}$	1.24	$3.62 \cdot 10^{-03}$	0.24	1.51
^{15}O	122.24 s	$3.99 \cdot 10^{-02}$	$3.16 \cdot 10^{-02}$	1.26	$6.69 \cdot 10^{-02}$	0.18	1.68
^{19}O	27.1 s	$1.23 \cdot 10^{-06}$	$1.59 \cdot 10^{-06}$	0.77	$1.14 \cdot 10^{-06}$	0.26	0.93
^{18}F	109.77 m	$3.22 \cdot 10^{-05}$	$3.41 \cdot 10^{-05}$	0.94	$3.58 \cdot 10^{-05}$	0.22	1.11
^{23}Ne	28.0 s	$3.40 \cdot 10^{-06}$	$3.86 \cdot 10^{-06}$	0.88	$3.62 \cdot 10^{-06}$	0.22	1.06
^{24}Ne	3.38 m	$6.65 \cdot 10^{-07}$	$8.30 \cdot 10^{-07}$	0.80	$6.48 \cdot 10^{-07}$	0.25	0.97
^{22}Na	2.602 y	$1.25 \cdot 10^{-05}$	$1.29 \cdot 10^{-05}$	0.97	$1.58 \cdot 10^{-05}$	0.20	1.26
^{24}Na	15.0 h	$1.96 \cdot 10^{-05}$	$1.89 \cdot 10^{-05}$	1.04	$2.57 \cdot 10^{-05}$	0.19	1.31
^{25}Na	60.0 s	$6.65 \cdot 10^{-06}$	$7.00 \cdot 10^{-06}$	0.95	$7.63 \cdot 10^{-06}$	0.21	1.15
^{27}Mg	9.5 m	$1.04 \cdot 10^{-05}$	$9.40 \cdot 10^{-06}$	1.11	$1.34 \cdot 10^{-05}$	0.20	1.29
^{28}Mg	20.91 h	$4.71 \cdot 10^{-06}$	$4.03 \cdot 10^{-06}$	1.17	$6.91 \cdot 10^{-06}$	0.19	1.47
^{26}Al	7.16×10^{5} y	$1.77 \cdot 10^{-05}$	$1.83 \cdot 10^{-05}$	0.97	$2.25 \cdot 10^{-05}$	0.18	1.27
^{28}Al	2.24 m	$5.45 \cdot 10^{-05}$	$5.15 \cdot 10^{-05}$	1.06	$7.61 \cdot 10^{-05}$	0.18	1.40
^{29}Al	6.6 m	$2.37 \cdot 10^{-05}$	$2.05 \cdot 10^{-05}$	1.16	$3.32 \cdot 10^{-05}$	0.19	1.40
^{31}Si	157.3 m	$3.50 \cdot 10^{-05}$	$3.24 \cdot 10^{-05}$	1.08	$5.28 \cdot 10^{-05}$	0.18	1.51
^{32}Si	450.0 y	$2.28 \cdot 10^{-05}$	$2.03 \cdot 10^{-05}$	1.12	$3.51 \cdot 10^{-05}$	0.18	1.54
^{30}P	2.499 m	$1.43 \cdot 10^{-05}$	$1.41 \cdot 10^{-05}$	1.01	$1.96 \cdot 10^{-05}$	0.19	1.38
^{32}P	14.29 d	$2.04 \cdot 10^{-04}$	$1.80 \cdot 10^{-04}$	1.13	$3.15 \cdot 10^{-04}$	0.17	1.55
^{33}P	25.4 d	$3.70 \cdot 10^{-04}$	$3.13 \cdot 10^{-04}$	1.18	$6.12 \cdot 10^{-04}$	0.18	1.66
^{35}P	47.4 s	$3.59 \cdot 10^{-05}$	$2.92 \cdot 10^{-05}$	1.23	$6.11 \cdot 10^{-05}$	0.19	1.70
^{35}S	87.44 d	$4.67 \cdot 10^{-04}$	$3.77 \cdot 10^{-04}$	1.24	$8.09 \cdot 10^{-04}$	0.19	1.73
^{37}S	5.06 m	$1.92 \cdot 10^{-04}$	$1.46 \cdot 10^{-04}$	1.32	$2.99 \cdot 10^{-04}$	0.15	1.56
^{38}S	2.87 h	$8.25 \cdot 10^{-05}$	$6.50 \cdot 10^{-05}$	1.27	$1.46 \cdot 10^{-04}$	0.20	1.77
^{34m}Cl	32.0 m	$1.04 \cdot 10^{-05}$	$8.95 \cdot 10^{-06}$	1.16	$1.68 \cdot 10^{-05}$	0.17	1.62
^{36}Cl	3.01×10^{5} y	$1.17 \cdot 10^{-03}$	$9.30 \cdot 10^{-04}$	1.25	$2.07 \cdot 10^{-03}$	0.18	1.78
^{38}Cl	37.21 m	$1.05 \cdot 10^{-03}$	$8.25 \cdot 10^{-04}$	1.27	$1.88 \cdot 10^{-03}$	0.20	1.80
^{39}Cl	55.6 m	$1.71 \cdot 10^{-03}$	$1.36 \cdot 10^{-03}$	1.25	$3.03 \cdot 10^{-03}$	0.20	1.78
^{40}Cl	1.4 m	$3.56 \cdot 10^{-04}$	$2.76 \cdot 10^{-04}$	1.29	$6.28 \cdot 10^{-04}$	0.18	1.76
^{37}Ar	35.02 d	$1.07 \cdot 10^{-02}$	$1.04 \cdot 10^{-02}$	1.02	$1.22 \cdot 10^{-02}$	0.20	1.15
^{39}Ar	269.0 y	$9.25 \cdot 10^{-03}$	$7.25 \cdot 10^{-03}$	1.28	$1.47 \cdot 10^{-02}$	0.15	1.59
^{41}Ar	1.827 h	$3.77 \cdot 10^{-01}$	$3.78 \cdot 10^{-01}$	1.00	$4.09 \cdot 10^{-01}$	0.23	1.08
^{38}K	7.636 m	$5.75 \cdot 10^{-06}$	$5.05 \cdot 10^{-06}$	1.14	$8.41 \cdot 10^{-06}$	0.39	1.46
^{40}K	1.28×10^{9} y	$3.52 \cdot 10^{-05}$	$2.91 \cdot 10^{-05}$	1.21	$4.87 \cdot 10^{-05}$	0.72	1.38

Differences between the nuclide production predicted by the two MARS simulations for Points 3 and 7 can be attributed to the total collimator lengths and the shielding design, both of which are different for the two insertions. In particular, in the calculations for Point 7 shielding was assumed to be thicker, thus diminishing the isotope production. As can be seen in the last column of Table 6.11 the new generic study gives a larger total activity than the calculations for Point 3, reasons being discussed in the following.

For the characterization of the production and release of airborne radioactivity it has been common to group isotopes corresponding to whether they have a half-life of less or more than

one day. Isotopes of environmental significance belonging to the former group are ^{11}C, ^{13}N and ^{15}O. In addition, the two isotopes which dominate at long decay times, ^{3}H and ^{7}Be, are typically given explicitly. Separately, for the unshielded and shielded case, Table 6.12 lists the most important isotopes together with their production mechanisms - sorted according to their total activity after one year of LHC operation.

Table 6.12: Most dominant isotopes for air activation in the beam cleaning insertions. Their common production mechanism is shown, isotopes are grouped according to their half-lives and listed with decreasing total activity.

	Unshielded			Shielded		
	Production	**Isotope**	**Half-life**	**Production**	**Isotope**	**Half-life**
Tritium	Spallation	^{3}H	12.35 y	Spallation	^{3}H	12.35 y
Beryllium	Spallation	^{7}Be	53.3 d	Spallation	^{7}Be	53.3 d
$T_{1/2}$ < 1 day	Spallation Spallation Spallation (n,γ)	^{13}N ^{11}C ^{15}O ^{41}Ar	9.965 m 20.38 m 122.24 s 1.827 h	(n,γ) Spallation Spallation Spallation Spallation	^{41}Ar ^{13}N ^{11}C ^{15}O ^{14}O	1.827 h 9.965 m 20.38 m 122.24 s 71.0 s
Other isotopes with $T_{1/2}$ > 1 day	(n,p) Spallation Spallation Spallation Spallation	^{14}C ^{10}Be ^{39}Ar ^{37}Ar ^{36}Cl	5730.0 y $1.60 \cdot 10^{6}$ y 269.0 y 35.02 d $3.01 \cdot 10^{5}$ y	(n,p) Spallation Spallation Spallation	^{14}C ^{10}Be ^{39}Ar ^{37}Ar	5730.0 y $1.60 \cdot 10^{6}$ y 269.0 y 35.02 d

Except for ^{14}C and ^{41}Ar, which are products of low-energy neutron interactions, spallation is the dominant reaction. ^{10}Be, ^{39}Ar as well as ^{36}Cl are typical products of reactions in the 10-100 MeV region. It should be noted that photoproduction of ^{13}N and ^{15}O is usually neglected at hadron accelerators. The comparisons discussed below follow the same subdivision.

Table 6.13: Ratios for isotope production for the “Generic 1" and the “IP3” simulations.

Generic versus IP3	**Isotope**	**Total**	**Inside**	**Outside**
Tritium	^{3}H	2.07	2.53	1.66
Beryllium	^{7}Be	2.62	3.65	1.59
$T_{1/2}$ < 1 day	^{41}Ar ^{13}N ^{11}C ^{15}O ^{14}O	0.94 1.70 2.36 2.00 2.33	0.03 1.70 3.15 2.36 3.15	1.08 1.70 1.60 1.68 1.51
Other isotopes with $T_{1/2}$ > 1 day	^{14}C ^{10}Be ^{39}Ar ^{37}Ar ^{36}Cl	0.94 1.53 1.38 1.04 1.83	0.06 1.20 1.13 0.56 1.90	1.09 1.79 1.59 1.15 1.78

A more detailed comparison between the results for the simplified case 'Generic 1' and for Point 3 is possible as values for the latter are available separately, for air volumes inside and outside the shield. It should again be emphasized that the simulations for Point 3 included dense shielding surrounding both beam pipes whereas only a 20 cm thick shield at a distance of 15 cm was assumed in this study. Table 6.13 gives the ratios of the total activities of the most important isotopes between the simplified case and the detailed MARS calculations. In addition to the two contributions, *i.e.,* activities produced inside and outside the shield, the ratio is also shown for the total activity.

As can be seen, the activities agree within a factor of two outside the shield. In particular, the almost identical results for the two isotopes created in low-energy neutron activation process, ^{14}C and ^{41}Ar, indicate consistency and support the validity of the simplified approach. Considerable differences exist for the activation inside the shield which can be explained by the different shielding design. In the simplified case the inside air volume is much larger allowing a much stronger activation by spallation reactions than is the case in the heavily shielded scenario for Point 3. On the other hand, low-energy neutron activation is reduced in the former case due to the significantly harder neutron energy spectrum.

Having demonstrated that the simplified approach allows relatively accurate estimates one may now use it for studying the influence of different collimator lengths and materials on air activation. Table 6.14 shows the ratios of the total activities for simplified scenarios with 3 m long and 1.5 m long collimators (cases "Generic 1" and "Generic 2" in Table 6.10), again with and without shielding.

Table 6.14: Ratios for isotope production for the "Generic 1" and "Generic 2" simulations, comparing different length of collimators.

Generic 1 versus 2	**Isotope**	**Unshielded**	**Shielded**
Tritium	^{3}H	0.90	1.12
Beryllium	^{7}Be	0.99	1.16
$T_{1/2}$ < 1 day	^{41}Ar ^{13}N ^{11}C ^{15}O ^{14}O	0.96 0.94 1.00 1.00 1.02	1.00 1.10 1.14 1.12 1.13
Other isotopes with $T_{1/2}$ > 1 day	^{14}C ^{10}Be ^{39}Ar ^{37}Ar ^{36}Cl	0.96 0.92 0.89 0.95 0.94	1.00 1.11 1.09 1.02 1.08

Ratios vary only slightly from unity except for tritium and beryllium where the 20 % increase in the shielded "Generic 1" scenario can be explained by the higher particle multiplicity in the interactions with the larger collimator and thus stronger re-interactions and scattering with the shielding. Otherwise, activities for ^{41}Ar and ^{14}C agree remarkably well in the shielded case. It can be concluded that the total collimator length has negligible influence on the air activation, however, as a matter of course this holds only true in case of a minimal collimator length of several hadronic interaction lengths.

Similarly, the influence of different collimator materials, in particular of copper and beryllium, was studied by replacing the 3 m long copper collimator by a beryllium collimator of the same hadronic interaction length (*i.e.,* 4 m total length; case "Generic 3") as shown in Table 6.15. The material effects air activation within about 20-30% being lower in case of beryllium, most likely due to less re-interactions in the collimator itself. Activities of isotopes produced by low-energy neutron interactions show the largest differences because of a higher low-energy neutron yield in case of copper.

In order to evaluate the effect of shielding, for all three generic scenarios, the simulation results for isotope production were compared for the unshielded and the shielded case (see Table 6.16).

Table 6.15: Ratios for isotope production for the "Generic 3" and "Generic 2" simulations, comparing beryllium and copper as possible different materials for the collimator jaws.

Generic 3 versus 2	Isotope	Unshielded	Shielded
Tritium	^{3}H	0.91	0.94
Beryllium	^{7}Be	0.96	0.98
$T_{1/2}$ < 1 day	^{41}Ar ^{13}N ^{11}C ^{15}O ^{14}O	0.64 0.85 0.93 0.90 0.93	0.82 0.90 0.96 0.93 0.96
Other isotopes with $T_{1/2}$ > 1 day	^{14}C ^{10}Be ^{39}Ar ^{37}Ar ^{36}Cl	0.64 0.79 0.76 0.74 0.86	0.82 0.87 0.86 0.83 0.90

Table 6.16: Ratios are shown for isotope production comparing unshielded and shielded configurations for all three generic studies.

unshielded versus shielded	Isotope	3 m Copper	1.5 m Copper	4 m Beryllium
Tritium	^{3}H	2.93	3.65	3.54
Beryllium	^{7}Be	3.78	4.40	4.30
$T_{1/2}$ < 1 day	^{41}Ar ^{13}N ^{11}C ^{15}O ^{14}O	0.63 2.65 3.77 3.28 3.94	0.66 3.10 4.28 3.70 4.39	0.51 2.94 4.15 3.60 4.25
Other isotopes with $T_{1/2}$ > 1 day	^{14}C ^{10}Be ^{39}Ar ^{37}Ar ^{36}Cl	0.63 2.03 2.01 1.05 2.71	0.66 2.46 2.46 1.13 3.11	0.51 2.22 2.17 1.01 2.97

Isotopes produced in spallation reactions are suppressed with shielding by a factor three to four. On the other hand, isotope production by low-energy neutron activation are increased by a factor of two in the shielded scenario.

In summary, the shielding has the largest effect on air activation of all studied parameters and might be critical when comparing releases at the surface to radiological limits for airborne radioactivity.

6.5.3 Release

For a correct assessment of the environmental impact of the various scenarios it is necessary to calculate the isotope concentration at the release point, choosing an appropriate model for the air movement during activation and in transit to the release point. In particular it is assumed that the air passes at a uniform speed through the irradiation region without turbulence (laminar flow model [122]) and from then onwards moves directly to the release point.

In a simplified calculation, let the number of beam particles (protons) intercepted per second in the collimation region be n_p which is a function of time and L be the length of the respective section of the accelerator tunnel. If the total volume of the air circuit is V_{irr} (cm^3) and the flow rate through the circuit is Q ($cm^3\ s^{-1}$), the linear velocity of the air in the tunnel or pipe, v, is:

$$v\ \left[\frac{cm}{s}\right] = \frac{QL}{V_{irr}}. \qquad \text{(xii)}$$

The number of nuclei of a given radionuclide produced during a time dt in an elemental length of the activation region dx at a distance x from the end of the activating region then is,

$$\frac{n_p P dt dx}{L} \qquad \text{(xiii)}$$

where P is the total number of nuclei of the radionuclide produced in the air by the loss of one proton and L is the length of the activation region. The transit time for the air in this elemental volume to reach the end of the activating region is x/v, and so the number of radioactive nuclei reaching the end of the activation region is,

$$\frac{n_p P dt dx \exp\left(\frac{-x}{v\tau}\right)}{L} \qquad \text{(xiv)}$$

where τ is the mean lifetime of the radionuclide. The total activity, A, produced in the time dt in the whole activation region and which reaches the end of this region is obtained by integrating Equation *(xiv)* over the whole length L and is given by:

$$A = \frac{n_p P dt}{t_{irr}} \cdot \left[1 - \exp\left(\frac{-t_{irr}}{\tau}\right)\right] \qquad \text{(xv)}$$

where $t_{irr} = L/v$ is the transit time for the air to traverse the activation region. If it takes a time t_d for the air to reach the release point, the amount of radioactivity, $\tilde{A}$, produced in the time dt and which escapes to the environment is given by:

$$\tilde{A} = \frac{n_p P dt}{t_{irr}} \cdot \left[1 - \exp\left(\frac{-t_{irr}}{\tau}\right)\right] \cdot \exp\left(\frac{-t_d}{\tau}\right). \qquad \text{(xvi)}$$

The total amount of radioactivity released during one operating period, A_{tot}, is then simply:

$$A_{tot} = N_p \cdot \frac{P}{t_{irr}} \cdot \left[1 - \exp\left(\frac{-t_{irr}}{\tau}\right)\right] \cdot \exp\left(\frac{-t_d}{\tau}\right) \qquad \text{(xvii)}$$

where N_p is the total number of protons intercepted by the target during a certain operating period.

The release to the environment of the radioactivity produced in the betatron and momentum cleaning insertions is calculated according to Equation *(xvii)* by taking into account the ventilation parameters as given in Table 6.17. Also listed are the respective lengths and diameters for the additional extraction tunnels, as well as for the shaft, all influencing the period of cooling time are hence, the total release. Assuming that both insertions equally share the total annual proton loss, the number of intercepted protons, N_p, in each insertion amounts to

5 x 10^{16} (see Section 6.1). Furthermore, the total yield of a certain radionuclide produced by one lost proton, *P*, is obtained directly from the Monte Carlo simulation.

Table 6.17: Geometry parameters as used in the calculations of the activity being produced in the cleaning insertions and released at the ventilation points of IP3 and IP7.

Ventilation Parameters		Point 3	Point 7
Ventilation Speed / m^3/h		45000	36000
Beam Cleaning Insertion	Length / m	269.0	269.0
	Diameter / m	3.80	3.80
Additional Tunnel Section R33 (IP3), none (IP7)	Length / m	500.0	-
	Diameter / m	4.20	-
Release Tunnel (IP3) Duct (IP7) TZ32 (IP3), TZ76 (IP7)	Length / m	870.0	370.0
	Diameter / m	3.10	1.35
Release Pit PM32 (IP3), PM76 (IP7)	Length / m	68.0	90.0
	Diameter / m	7.1	1.60

Similar to the comparison of the production yields inside the LHC tunnel the values are now calculated for the release points and predictions for different scenarios are compared to each other. Thus, by applying Equation *(xvii)* to both the results from the MARS simulations for Points 3 and 7 and the simplified model the generic approach can again be checked for consistency and validity. As previously mentioned, the ventilation parameters (ventilation speed, air volume, *etc.*) are different for the two insertions such that the results of the simplified approach have to be processed with the two sets of parameters for realistic predictions for the release points. Table 6.18 shows the results for each case, *i.e.,* the total activities obtained with the simplified model ("Generic 1") and the detailed MARS-simulations as well as the ratios between both.

Table 6.18: Annual release of radioactivity for the two cleaning insertions. Layout parameters have been included as stated in Table 6.17 with corresponding ventilation speeds of 45000 m^3/h for IP3 and 36000 m^3/h for IP7.

New versus Old	**IP7 (36000 m^3/h)**			**IP3 (45000 m^3/h)**		
	New (total)	**Old (outside)**	**Ratio**	**New (total)**	**Old (total)**	**Ratio**
Tritium	$2.80 \cdot 10^{07}$	$6.32 \cdot 10^{06}$	4.44	$2.80 \cdot 10^{07}$	$1.35 \cdot 10^{07}$	2.07
Beryllium	$7.12 \cdot 10^{08}$	$1.22 \cdot 10^{08}$	5.82	$7.12 \cdot 10^{08}$	$2.71 \cdot 10^{08}$	2.62
$T_{1/2}$ < 1 day	$3.51 \cdot 10^{13}$	$9.16 \cdot 10^{12}$	3.83	$1.40 \cdot 10^{13}$	$5.41 \cdot 10^{12}$	2.58
Other isotopes with $T_{1/2}$ > 1 day	$2.56 \cdot 10^{08}$	$1.63 \cdot 10^{08}$	1.56	$2.56 \cdot 10^{08}$	$2.15 \cdot 10^{08}$	1.19

In the generic case, calculated total activities differ only between IP3 and IP7 for isotopes with half-lives smaller than one day where a difference in the length of the activation and cooling region affects the buildup of the isotopes and their decay respectively. In case of the old calculations for IP7 it should again be stressed, that any air volumes inside the shield were neglected and the activities refer to the contribution from air activation outside the shield only. Therefore, the values from this study are about a factor of 5-6 higher than those of the earlier MARS study for tritium and beryllium and a factor of about 3 higher for short-lived isotopes.

Since in reality there will most likely be significant air volumes inside the shielding (if there will be shielding at all) of which activated air will mix with air outside the shield, the estimate for Point 7 obtained with MARS is considered to be too low. On the other hand, the earlier results for Point 3 which included also air activation inside the shield are much closer to the values of this study, *i.e.,* a factor of 2-3 for tritium and beryllium and an average factor of about 1.5 for the short-lived isotopes Table 6.18.

As previously demonstrated, the total length of the collimators as well as their material has only minor influence on air activation. This is also confirmed for the release values and ratios between the scenarios with 3 m and 1.5 m long collimators and between scenarios with beryllium and copper collimators of equal interaction length are given in Table 6.19.

Table 6.19: Ratios for the annual release comparing different total lengths for the collimators, as well as beryllium and copper as possible materials.

	3 m versus 1.5 m Copper		***Beryllium versus Copper***	
	unshielded	**shielded**	**unshielded**	**shielded**
Tritium	0.90	1.12	0.91	0.94
Beryllium	0.99	1.16	0.96	0.98
$T_{1/2}$ < 1 day	0.97	1.10	0.88	0.90
Other isotopes with $T_{1/2}$ > 1 day	0.98	1.05	0.85	0.86

Table 6.20: Ratios for the annual release comparing unshielded and shielded configurations for all three generic studies.

unshielded versus shielded	**3 m Copper**	**1.5 m Copper**	**4 m Beryllium**
Tritium	2.93	3.65	3.54
Beryllium	3.78	4.40	4.30
$T_{1/2}$ < 1 day	2.68	3.04	2.95
Other isotopes with $T_{1/2}$ > 1 day	1.65	1.76	1.73

On the other hand, the amount of local shielding around the beam cleaning insertions should have a significant influence on the released activity. The more shielding is placed close to the loss points the more hadronic activity is transferred to the shield rather than to the air, thus, less airborne radioactivity is produced. This is confirmed by the ratios between the activities for the unshielded and the shielded scenarios for the various collimator lengths and materials and given in Table 6.20.

Due to heat production of additionally electrical installations in the tunnel an increase of the ventilation speed from 36000 m^3/h to 45000 m^3/h became necessary. Therefore, in order to assess the influence of the shorter cooling time until the air reaches the release point, the

"Generic 1" simulation was used to asses the annual release as a function of different ventilation speeds as shown in Figure 6.29.

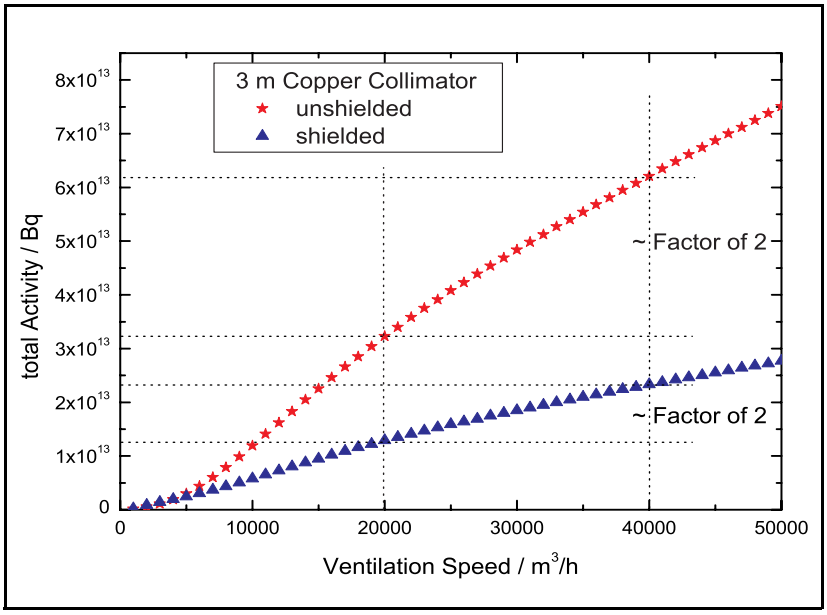

Figure 6.30: Annual release of radioactivity from isotopes with a half-life smaller than one day for various ventilation speeds for the "Generic 1" case.

Evidently, due to effects of buildup and decay only isotopes with half-lives smaller than one day are affected. In both, the shielded and the unshielded case, a duplication in the ventilation speed results in a factor of two in the amount of radioactivity at the release point.

As described in Section 3.3.3 for the eventual determination of the total dose to the critical group in the vicinity to the respective release points a radio-ecological study and a comparison to release limits will have to be performed as described in Section 3.3.3., possibly based on the results for the different simplified scenarios.

For the moment conclusions can only be drawn on relative changes. In case of Point 7 the values calculated with MARS will increase by about a factor of two due to the higher ventilation speed of 36000 m^3/h as compared to 22500 m^3/h used in the earlier simulations [110]. Furthermore, the consideration also of air activation inside the shielding as well as the latest collimator layout may triple the released activity as would the complete omission of shielding. Therefore, under most conservative considerations this issues a maximal increase of radioactivity released by a factor of 18 compared to former studies for Point 7 [110]. The same factor holds also true for IP3, since up to know the only available release calculation assumed equal production yields at the release points of each of the two cleaning insertions [115].

7 Summary and Conclusions

This thesis contributes to radiological assessments of the LHC design and operation. In particular, the scope of this thesis was to examine the beam cleaning insertions - two of the main loss regions of the LHC where accelerated beam particles which would otherwise cause unwanted losses at different places of the machine are purposely intercepted. Two critical issues with regard to the protection of personnel and environment were studied: remanent dose rates due to induced radioactivity and airborne radioactivity. A detailed estimate of remanent dose rates is important for an optimization of later maintenance and repair interventions by adapting the design of the components correspondingly. Only very limited information on remanent dose rates to be expected around the collimators was available so far. This thesis is an attempt to extend the knowledge considerably, especially by applying a new calculation method. Since this new approach was used for the first time in the design of LHC components a careful benchmarking with experimental data was needed. Therefore, a corresponding experiment was performed as part of this work. A revision of existing assessments of airborne radioactivity became necessary after various changes in the design of the collimation system as well as modifications in the ventilation scheme of the LHC.

Benchmark Measurements

Various samples of different materials typically used at accelerators were irradiated at the CERF facility in the stray radiation field downstream of a copper target. At this location particle spectra exhibit a significant high-energy component resembling the situation which can be expected for loss regions at high-energy accelerators, *e.g.*, at the LHC. Specific activity as well as remanent dose rates were measured at different cooling times after the irradiation and results were compared to predictions from detailed FLUKA simulations.

Good agreement was found between the measured and calculated specific activities of most of the identified isotopes. They are reproduced by FLUKA within the uncertainties of the measurement. Discrepancies were observed for intermediate and small-mass isotopes which can most likely be attributed to deficiencies in the FLUKA simulation models. In case of copper the calculated activities are systematically lower than the measured values. Possible reasons for this behaviour, *e.g.,* uncertainties in the elemental composition of the sample assumed in the calculations or a possible misalignment of the sample with respect to the beam axis, are still under investigation. An option to understand better observed discrepancies is to fold calculated particle fluence with experimental cross-sections for the production of a particular isotope. In case of ^{24}Na in aluminium the folding indeed confirms that the partial cross-section is underestimated by FLUKA by about 30% as it yields a specific activity in agreement with the measured value.

However, for the calculation of integral quantities such as total activity or dose rates, observed deficiencies in the production of particular isotopes should have only small influence, since over- and underestimates for single elements tend to compensate each other. This was shown with the calculations for remanent dose which were successfully benchmarked with the experimental results. The detailed comparison of measured and calculated dose equivalent rates showed generally good agreement to within 20 - 40 % for the small samples, as well as for extended objects such as the CERF target. In situations where only a few isotopes dominate the dose rate, such as ^{24}Na in case of aluminium, the predictions significantly depend on the accuracy of the models for isotope production. If such deficiencies are known (*e.g.,* from activation studies), it can be compensated for by applying correction factor in the dose rate calculations. This explicit method can therefore be applied to arbitrary situations, *e.g.,* the prediction of the remanent dose rates in the LHC beam cleaning insertions.

Remanent Dose Rates in the Beam Cleaning Insertions

It was shown that as compared to the total length of a cleaning insertion of more than 500 m, particle losses at collimators activate only “locally” the surrounding area. Areas of high dose rate extend only up to about 10 to 20 m downstream of the respective collimator. Hence, for a calculation of remanent dose rates it was not necessary that the layout of the whole cleaning insertion was implemented in full detail but it was sufficient to consider only a small section with typical configurations.

Therefore, only two representative configurations were studied. In the first case the collimator is located in a sector without other massive beamline elements (magnets, *etc.*) downstream of it. Here, particle losses activate the collimator, the downstream vacuum pipe and equipment as well as any local shielding and the concrete of the surrounding tunnel. In the second configuration the collimator is installed immediately upstream of a magnet. In this case also the front face of the magnet will be significantly activated.

The former configuration approximated with a cylindrical geometry allows fast first estimates. It therefore allows for an efficient study and intercomparison of different layouts (collimator materials, shielding scenarios, *etc.*). In the present study collimator materials currently discussed in the collimator-design study group were investigated: carbon composite, boron nitride, aluminium, copper and tungsten. Since recent heat-load and material stress calculations identified low-Z materials as the best choice, carbon composite will most likely be chosen as collimator material in the final design.

Different methods to calculate remanent dose rates were applied to the simplified layout and results were compared to each other. Calculations based on ω-factors (contact dose rates) were compared to preceding MARS calculations as well to the explicit simulation method. In addition, maximal remanent dose rates were set against derived limits. In case of the “classical” ω-factor method, for the copper collimator the maximum remanent dose rate on the outside of the shield is about 9 mSv/h. The difference when compared to earlier simulations (~2.5 mSv/h) is due to two reasons. The first being the reduced shielding of only 20 cm of iron and the second that secondary particles escape through the aperture of the collimator.

Since a thorough assessment of repair or maintenance interventions is difficult to perform with the ω-factor approach, for the same simplified collimator layout a full simulation of isotope production and of the transport and interactions of the radioactive decay products was performed and its results were compared to those obtained with the ω-factor method. The comparison showed that due to its underlying assumptions the latter method tends to overestimate true contact dose rates. This is mainly due to the assumption of the ω-factor method which is based on an infinitely large and homogeneously irradiated object and also supported by the fact that smaller differences in the predicted values could be observed in case

of large object like the iron shield. In case of the carbon collimator, the shield significantly contributes to the dose rates in the aisle, explained by the fact that due to secondary high-energy interactions a significant cascade only fully develops inside the iron shield. It was shown that the tunnel wall and floor dominate the dose rate for cooling times of less than three days. This is due to the sodium content in the concrete which leads to a significant yields of ^{24}Na, mainly produced by low-energy neutron capture on ^{23}Na.

Dose Estimates for Maintenance Interventions

In order to estimate the dose to personnel for a typical example of an intervention on the vacuum system a section of the beamline was modelled and simulated in detail with FLUKA. Dose rates around collimators not only depend strongly on the cooling time but also on the location with respect to the main contributing sources, the collimators within their vessels and possible downstream installations. Therefore, for this study of remanent dose rate distributions all elements were implemented in detail, accounting for the exact dimensions as well as their respective materials, carbon composite for the collimator, copper for the beam pipe, stainless steel for flanges and bellow models, as well as additional materials used for the magnet or the vacuum pump.

As was shown, the two collimators and the magnet clearly dominate the dose rate at short cooling times, leading to peak values on contact to the surface of the quadrupole of the order of 10 mSv/h. During maintenance the magnet may not have to be directly touched, however work, necessary to be carried out adjacent to the magnets will certainly have to be minimised. In general, high dose rates of several mSv/h are only reached close to the installations, whereas at a distance of 50 cm remanent dose rates are lower by an order of magnitude. Due to the materials being used for the equipment (*e.g.,* copper, iron) a comparable decrease is foremost reached 4 months after the end of operation.

It was shown that remanent dose rates are significant (several mSv/h) but not prohibitive for maintenance work when compared to derived limits. Based on the results obtained for different locations and various cooling times a thorough estimation of dose to personnel was performed for an exemplary intervention at a vacuum pump installed close to the collimator. The results clearly indicate that any vacuum intervention in this critical region will have to be well planned and optimized with respect to working time and methods. In order to avoid unnecessary exposure of personnel, if possible, periods towards the end of a shutdown, *i.e.,* a cooling time in the order of four months, should be envisaged for time-consuming interventions.

Air Activation and Ventilation

Calculations were carried out in order to estimate the release of radioactivity in air produced in the two collimation insertions of the LHC. In particular, air activation was calculated using a simplified geometrical model of the cleaning insertion and various scenarios, which included different collimator materials and lengths. The validity of the approach was demonstrated by comparing the results to those of earlier studies based on more detailed, although now obsolete layouts of the cleaning insertions.

The study considered 39 different radionuclides, while their production was estimated from the hadron track-length distributions in the air volumes along the beam cleaning insertions and evaluated isotope production cross-sections. The specific activity released at the surface was been estimated using a laminar flow model. It was shown that a simplified geometric model of the beam cleaning insertions can be used, since the activation of air caused by one primary proton lost in a collimator is mainly determined by the collimator itself and by the layout of the nearby shielding and (downstream) beamline elements. Other beamline components, usually located at rather large distance, are shadowed by those close to the collimator and therefore

give only minimal contributions to the air activation. In total two collimator materials were studied, copper and beryllium, as well as two different total lengths. For each configuration two simulations were performed, with and without a longitudinal iron shield of 20 cm thickness. In addition, all scenarios were studied for different ventilation rates.

Differences between the specific activities obtained in this study and earlier simulations could be attributed to different total collimator lengths and shielding designs. For the moment conclusions can only be drawn on relative changes of the isotope production and the total activity released. Values calculated with precedent MARS simulations will increase by about a factor of two due to the higher ventilation rate. Furthermore, the latest collimator layout as well as the implementation of a reduced but more realistic shielding would increase the produced radioactivity by a factor of three. In addition, the complete omission of shielding would triple the released activity. Therefore, under most conservative considerations this would result in a maximal increase of released radioactivity by a factor of 18 as compared to former studies.

To summarize, this thesis successfully benchmarked the new explicit simulation approach in order to calculate remanent dose rates. It was applied to the beam cleaning insertions and it was shown that it is superior to the ω-factor approach in many cases. In particular detailed studies for maintenance became only possible due to the capability of the new approach to calculate remanent dose rates at any arbitrary location. The advantages of the new method were clearly demonstrated so that it can be used for future simulations. In addition, the calculations concerning airborne radioactivity and their dependence on changes in the layout of the beam cleaning insertion will serve as basis for further calculations. In particular the different release scenarios will have to be taken as possible source terms for accurate calculations of annual dose equivalents to the critical group in the vicinity of the respective release point.

In both studies results were achieved which give important input to the design of the collimators and the beam cleaning insertions. However, as the layout has not been finalised yet and no prototype collimator exists at this moment the studies will have to be extended in the future. For example, it will soon have to be assessed to which extend local shielding should be foreseen next to the collimators and beamline elements. Shielding may certainly play an important role in reducing the amount of airborne radioactivity released to the environment by capturing secondary particles. On the other hand, shielding will significantly complicate any maintenance intervention as it contributes to the overall dose received by the personnel performing the intervention. An evaluation of advantages and disadvantages of shielding might be directly based on the results of this thesis. Furthermore, the study on air activation will have to be extended by a detailed calculation of the effective dose to the critical group next to the release point. Only then it will be possible to assess the impact of various design parameters, such as collimator material and length, shielding and ventilation rate. Finally, further experiments benchmarking the new approach of calculating remanent dose rates are required. So far, the new method has been primarily tested with relatively small samples. In reality, however, objects can be much larger (magnets, collimators, etc.) and the approach should also be tested for these cases.

Bibliography

[1] **The LHC Study Group,** *The Large Hadron Collider, Conceptual Design,* CERN/AC/05-05 (1995).

[2] **F. Zimmermann,** *Accelerator Physics Issues at the LHC and Beyond,* CERN SL/20020003 (2002).

[3] **O. Brüning *et al.,*** *LHC Luminosity and Energy Upgrade: A Feasibility Study,* CERN LHC Project Report 626 (2002).

[4] **R. Aßmann,** Proc. Chamonix 2003, CERN-AB-2003-008 ADM (2003).

[5] **J.B. Jeanneret, D. Leroy, L. Oberli, T. Trenkler,** *Quench levels and transient beam losses in LHC magnets,* LHC Project Report 44 (1996).

[6] **R. Aßmann, F. Schmidt, F. Zimmermann, M.P. Zorzano,** *Equilibrium Beam Distribution and Halo in the LHC,* LHC Project Report 592, EPAC02 (2002).

[7] **L. Burnod, J.B. Jeanneret,** *Beam losses and collimation in the LHC,* CERN-SL-91-39-EA, LHC Note 167 (1991).

[8] **J.B. Jeanneret,** *Optics of a two-stage collimation system,* CERN-LHC-Project Report 243 (1998).

[9] **N. Catalan-Lasheras, G. Ferioli, J.B. Jeanneret, R. Jung, D. Kaltchev, T. Trenkler,** *Proton Collimation in TeV Colliders,* LHC Project Report 156 (1997).

[10] **R. Aßmann *et al.*,** *Designing and Building a Collimation System for the High-Intensity LHC Beam,* CERN LHC Project Report 640 (2003).

[11] **R. Aßmann, C. Fischer, J.B. Jeanneret, R. Schmidt,** *Summary of the CERN Meeting on Absorbers and Collimators for the LHC,* LHC PROJECT NOTE 282 (2002).

[12] **R. Aßmann *et al.*,** *Requirements for the LHC collimation system,* CERN LHC Project Report 599 (2002).

[13] **R. Aßmann *et al.*,** *Proposal to the AB LHC Technical Committee (LTC),* on June 25th (2003).

[14] **R. Aßmann *et al.*,** *Beam Cleaning and Collimation System,* to be published in the updated LHC Design Report, chapter 18 (2003).

[15] **R. Principe, M. Wilhelmsson,** *Cooling and Ventilation for LHC,* in Proceedings of the Workshop on LHC Performance - Chamonix XI, Chamonix (2002).

Bibliography

[16] **C. Martel *et al.,*** *Air handling of the LHC tunnel and its underground areas,* CERN Engineering Specification, LHC/UA/ES/0001 (2003).

[17] **SAPOCO 42,** *Safety Policy at CERN,* Revision 2001.

[18] *Convention entre l'Organisation européenne pour la Recherche nucléaire (CERN) et le Gouvernement de la République française relative à la sûreté des installations liées au grand collisionneur de hadrons (LHC) et au supersynchrotron à protons (SPS).*

[19] **International Commission on Radiological Protection,** *1990 Recommendations of the International Commission on Radiological Protection,* ICRP Publication 60, Annals of the ICRP 21, 1–3, Pergamon Press (1991).

[20] **M. Brugger, D. Forkel-Wirth, S. Roesler, G. R. Stevenson,** *Constraints from induced radioactivity on design and maintenance,* in Proceedings of the Workshop on LHC Performance - Chamonix XII, Chamonix, March 3-8 (2003).

[21] *Ordonnance sur la radioprotection,* Switzerland, 22 June (1994).

[22] **Radiation Protection Group,** *Radiation Safety Manual 1996,* CERN (1996).

[23] *Arrêté du 12 mai 1998 modifiant l'arêté du 8 octobre 1990 modifié fixant la liste des travaux pour lesquels il ne peutêtre fait appel aux salariés sous contrat de travail à durée d´eterminée ou aux salariés des entreprises de travail temporaire,* Journal Officiel Numéro 118 du 23 Mai (1998).

[24] *Relatif á la protection des travailleurs contre les dangers des rayonnements ionisants,* Décret No. 86-1103 du 2 octobre 1986, Journal Officiel du 12 octobre (1986).

[25] **International Commission on Radiological Protection,** *Limits for intakes of radionuclides by workers,* ICRP Publication 30 plus Supplements and Addenda, Pergamon Press, Oxford, New York and Frankfurt (1980).

[26] **International Commission on Radiological Protection,** *Recommendations of the International Commission on Radiological Protection,* ICRP Publication 26, Pergamon Press, Oxford, New York and Frankfurt (1977).

[27] **International Commission on Radiological Protection,** *Annual limits on intake of radionuclides by workers based on the 1990 recommendations,* ICRP Publication 61, Pergamon Press, Oxford, New York and Frankfurt (1991).

[28] **L. Moritz,** *New Derived Release Limits for the CERN Meyrin Site,* CERN/TIS-RP/IR/96-07 (1996).

[29] **P. Vojtyla,** *Calculation of the Effective Dose to the Public due to Releases from the CERN Meyrin Site implementing the Swiss Directive HSK-R-41,* CERN/TIS-TE/98-20 (1998).

[30] **P. Vojtyla,** *Models for Assessment of the Environmental Impact of radioactive Releases from CERN Facilities,* CERN-TIS-2002-013-TE (2002).

[31] **J. Ranft,** *Monte Carlo calculation of energy deposition by the nucleon-meson cascade and total-absorption nuclear cascade (TANC) counters,* Nucl. Instrum. Meth. 81, p. 29 (1970).

[32] **J. Ranft,** *Estimation of radiation problems around high-energy accelerators using calculations of the hadronic cascade in matter,* Particle Accelerators 3, p. 129 (1972).

[33] **R. Hagedorn, J. Ranft,** Suppl. Nuovo Cimento 6, p. 169 (1966).

[34] **A. Fassò, A. Ferrari, P. R. Sala,** *Electron Photon Transport in FLUKA: Status, Proc. of the International Conference Monte-Carlo 2000,* Lisbon, Portugal, October 23-26, 2000, p. 159, Springer-Verlag Berlin Heidelberg (2001).

[35] **A. Fassò, A. Ferrari, J. Ranft, P. R. Sala,** *Fluka: Status and Prospective for Hadronic Applications, Proc. of the International Conference Monte-Carlo 2000,* Lisbon, Portugal, October 23-26, 2000, p. 955, Springer-Verlag Berlin Heidelberg (2001).

[36] **A. Ferrari, P. R. Sala,** *Physics of Showers induced by Accelerator Beams,* Lecture given at the 1995 "Frederic Joliot" Summer School in Reactor Physics, Cadarache, France (1995).

[37] **T. A. Gabriel, J. E. Brau, B. J. Bishop,** Report ORNL/TM-11060 (1989).

[38] **P. Cloth *et al*.,** Report KFA/Jül-2203 (1988).

[39] **R. E. Prael, H. Lichtenstein,** LA-UR-89-3014 (1989).

[40] **L.S. Waters, ed.,** *MCNPX Users Manual - Version 2.1.5,* Los Alamos National Laboratory, Los Alamos, NM, TPO-E83-G-UG-X-00001 (1999).

[41] **J.F. Breismeister, ed.,** *MCNP-A General Monte Carlo N-Particle Transport Code Version 4A,* Los Alamos National Laboratory, Los Alamos, NM, LA-12625-M (1993).

[42] **K. C. Chandler, T. W. Armstrong,** ORNL-4744 (1972), and Nucl. Sci. and Eng. 49 (1972), p. 110; **R. G. Alsmiller, F. S. Alsmiller, O. W. Hermann,** Nucl. Instr. Meth. A295, p. 337 (1990).

[43] **L. Dresner,** ORNL/TM-196 (1961), **M. P. Guthrie,** ORNL-4379 (1969) and ORNL/TM-3119 (1970).

[44] **A. Capella, U. Sukhatme, J. Tran Thanh Van,** Z. Phys. C3, p. 329 (1980);**A. Capella, J. Tran Thanh Van,** Phys. Lett. B93, p. 149 (1980).

[45] **A. Capella *et al*.,** Phys. Rep. 236, p. 225 (1994).

[46] **H. M. Chan, J. E. Paton, S. T. Tsou,** *Diffractive scattering in the dual model,* Nucl. Phys. B86, p. 479 (1975).

[47] **G. F. Chew, C. Rosenzweig,** *Asymptotic planarity: an S-matrix basis for the Okubo Zweig-lizuka rule,* Nucl. Phys. B104, p. 290 (1976).

Bibliography

[48] **G. F. Chew, C. Rosenzweig,** *Dual topological unitarization: an ordered approach to hadron theory,* Phys. Rep. 41, p. 263 (1978).

[49] **V. N. Gribov,** *A reggeon diagram technique,* Sov. Phys. JETP 26, p. 414 (1968).

[50] **M. Baker, K. A. Ter-Martirosyan,** *Gribov's Reggeon calculus: its physical basis and implications,* Phys. Rep. 28C, p. 1 (1976).

[51] **R. J. Glauber,** Phys. Rev. 100, p. 242 (1955).

[52] **V. N. Gribov,** *Interaction of gamma quanta and electrons with nuclei at high energies,* Sov. Phys. JETP 30, p. 709 (1970).

[53] **L. Bertochi,** Il Nuovo Cimento, 11A, p. 45 (1972).

[54] **K. Hänßgen, J. Ranft,** *The Monte Carlo code HADRIN to simulate inelastic hadron nucleon interactions at laboratory energies below 5 GeV,* Comp. Phys. Commun. 39, p. 37 (1986).

[55] **H. W. Bertini,** *Low-energy intranuclear cascade calculation,* Phys. Rev. 131, p. 1801 (1963).

[56] **N. Metropolis *et al.*,** *MonteCarlo calculations on Intranuclear Cascades, I. Low-Energy Studies,* Phys. Rev. 110, p. 185 (1958).

[57] **N. Metropolis *et al.*,** *MonteCarlo calculations on Intranuclear Cascades, II. High-Energy Studies and Pion Processes,* Phys. Rev. 110, p. 204 (1958).

[58] **P. R. Sala, A. Ferrari,** *A new model for hadronic interacctions at intermediate energies for the FLUKA code,* in Proceedings of the International Conference on Monte Carlo Simluation in High-Energy and Nuclear Physics, MC'93, Tallahassee, U.S.A., 1993, ed. by P. Dragovitsch, S. L. Linn and M. Burbank, World Scientific, Singapore, p. 277 (1994).

[59] **M. E. Grypeos *et al.*,** *The 'cosh' or symmetrized woods-saxon nuclear potential,* Journal of Physics G: Nuclear and Particle Physics, vol. G 17, p. 1093 (1991).

[60] **A. Ferrari, J. Ranft, S. Roesler, P. R. Sala,** *Cascade particles, nuclear evaporation and residual nuclei in high-energy hadron-nucleus interactions,* Z. Phys. C70, p. 413 (1996).

[61] **V. F. Weisskopf,** Phys. Rev. 52, p. 295 (1937).

[62] **N. Bohr, J. A. Wheeler,** Phys. Rev. 56, p. 426 (1939).

[63] **E. Fermi,** Prog. Theor. Phys. 5, p. 1570 (1950).

[64] **M. Epherre, E. Gradsztajn,** J. Physique 18, p. 48 (1967).

[65] **M. Huhtinen,** *Determination of Cross Sections for Assessments of Air Activation at LHC,* CERN/TIS-RP/TM/96-29 (1997).

[66] **A. Ferrari,** *Fortran-Routine,* USRSUW.

[67] **J. Hüfner,** *Heavy fragments produced in proton-nucleus and nucleus-nucleus collisions at relativistic energies,* Phys. Rep. 125, p. 129 (1985).

[68] **ICRU (1989),** *Tissue Substitutes in Radiation Dosimetry and Measurement,* Report 44 of the International Commission on Radiation Units and Measurements (Bethesda, MD) (1989).

[69] **R. H. Thomas, G. R. Stevenson,** *Radiological safety aspects of the operation of proton accelerators,* Technical Report Series No. 283, IAEA Vienna (1988).

[70] **A. Sullivan, T. Overton,** Health Physics 11, p. 1101 (1965).

[71] **M. Höfert, M. Bonifas,** *Measurement of Radiation Parameters for the Prediction of Dose Rates from Induced Radioactivity,* Rep. HP-75-148, CERN (1975).

[72] **M. Huhtinen, P. A. Aarnio,** *Production of long-lived radionuclides in CMS,* CERN CMS NOTE-1998/044 (1998).

[73] **M. Huhtinen,** *Advanced Method of Estimating Residual Dose Rates in a Hadron Environment,* CMS Note 2002/019 (2002).

[74] **M. Huhtinen,** *Method for estimating dose rates from induced radioactivity in complicated hadron accelerator geoometries,* CERN/TIS-RP/IR/98-28 (1998).

[75] **S. Roesler, M. Brugger, Y. Donjoux, A. Mitaroff,** *Simulation of Remanent Dose Rates and Benchmark Measurements at the CERN-EU High Energy Reference Field Facility,* to be published in proceedings of the 2003 ANS Annual Meeting - Nuclear Applications of Accelerator Technology (2003).

[76] **K. F. Eckerman, R. J. Westfall, J. C. Ryman, M. Cristy,** *Nuclear Decay Data Files of the Dosimetry Research Group,* ORNL/TM-12350, RSICC Data Library Collection, Program NUCDECAY (1993).

[77] **S. Y. F. Chu, L. P. Ekstrøm, R. B. Firestone,** *The Lund/LBNL Nuclear Data Search (*1999).

[78] **A. H. Sullivan,** *A guide to radiation and radioactivity levels near high-energy particle accelerators,* Nuclear Technology Publishing (1992).

[79] **S. H. Rokni *et al.*,** *Induced radioactivity of materials by stray radiation fields at an electron accelerator,* Nucl. Instrum. Meth. A 484, p. 680-689 (2002).

[80] **M. Silari, L. Ulrici S. Ye,** *On the estimation of low levels of induced radioactivity in LEP,* CERN Internal Report TIS-RP/IR/99-13 (1999).

[81] **K. A. Van Riper, S. G. Mashnik, W. B. Wilson,** *Computer Study of Isotope Production in High Power Accelerators,* LANL Report LA-UR-99-360 (1999).

[82] **S. G. Mashnik *et al.*,** *Production and Validation of Isotope Production Cross Section Libraries for Neutrons and Protons to 1.7 GeV,* LANL Report LA-UR-98-6000 (1998)

Bibliography

[83] **H. Vincke, I. Brunner, M. Huhtinen,** *Production of radioactive isotopes in Al, Fe and Cu-samples by stray radiation fields at a proton accelerator,* CERN-TIS-2002-007-RP-CF (2002).

[84] **I. Rakhno *et al.*,** *Benchmarking Residual Dose Rates in a NuMI-like Environment,* FERMILAB-Conf-01/304-E (2001).

[85] **P. A. Aarnio, T. T. Hakulinen, M. Huhtinen,** *Gamma-spectrometry and residual nuclide analysis of pion irradiated PbWO4 crystals,* Journal of Radioanalytical and Nuclear Chemistry, Vol. 248, No. 2, p. 385 (2001).

[86] **Y. E. Titarenko *et al.*,** *Experimental and computer simulation study of radioactivity of materials irradiated by intermediate energy protons,* arXiv:nucl-ex/9908015 v1 (1999).

[87] **Y. E. Titarenko *et al.*,** *Experimental and computer simulation study of radioactivity in heavy materials irradiated by intermediate energy protons,* arXiv:nucl-ex/9908012 v1 (1999).

[88] **M. Brugger, Y. Donjoux, A. Mitaroff, S. Roesler,** *Measurements and Simulation of Induced Activity at the CERN-EU High Energy Reference Field Facility,* to be published in proceedings of the 2003 ANS Annual Meeting - Nuclear Applications of Accelerator Technology (2003).

[89] **A. Mitaroff, M. Silari,** *The CERN-EU High Energy Reference Field (CERF) Facility for Dosimetry at Commercial Flight Altitudes and in Space,* Rad. Prot. Dosim., 102, p. 7 (2002).

[90] **E. Gschwendtner, A. Mitaroff, L. Ulrici,** *A New Calibration of the PIC Monitor in H6,* TIS-RP/IR/2000-09 (2000).

[91] **PerkinElmer Life Science,** Imperiastraat 8, B-1930 Zaventem, Belgium.

[92] **L. A. Currie,** *Limits for Qualitative Detection and Quantitative Determination,* Anal. Chem. 40, p. 568 (1968).

[93] **M. Huhtinen,** *Recommendations for irradiations of CMS components in the IRRAD2 facility at PS,* CMS Internal Note, CMS/IN/2001/012 (2001).

[94] **A. S. Iljinov *et al.*,** *Landolt-Börnstein: Zahlenwerte und Funktionen aus Naturwissenschaften und Technik - Band 13 Radionuklidprodution bei mittleren Energien,* Springer-Verlag (1991).

[95] **M. Pelliccioni,** *Overview of fluence-to-effective dose and fluence-to-ambient dose equivalent conversion coefficients for high-energy radiation calculated using the FLUKA code,* Rad. Prot. Dosim. 88, p. 279 (2000).

[96] **M. Höfert, K. Potter, G. R. Stevenson,** *Summary of Design Values, Dose Limits, Interaction Rates etc. for use in estimating Radiological Quantities associated with LHC Operation,* CERN/TIS-RP/IR/95-19.1 (1995).

[97] **G. R. Stevenson,** private communication.

[98] **Y. Baconnier, G. Brianti, Ph. Lebrun, A. Mathewson, R. Perin (eds.),** *LHC: The Large Hadron Collider Project,* CERN/AC/93-03(LHC) (1993).

[99] **K. Potter, G. R. Stevenson,** *Source intensities for use in the radiological assessment of the effect of proton losses at the scrapers and around the main ring of the LHC,* CERN TIS-RP/IR/95-16, AC/95-04(DI), LHC Note 322 (1995).

[100] **T.Trenkler,J.B.Jeanneret,** CERN SL/Note94-105(AP) (1994).

[101] **I. Baichev, D. Kaltchev,** *Implementation in Dimad of a new Collimator Element (STRUCT module),* TRIUMF Report (inpreparation).

[102] **R. Aßmann, M. Brugger, M. Hayes, J. B. Jeanneret, F. Schmidt, I. Baichev, D. Kaltchev,** *Tools for predicting cleaning efficiencies in the LHC,* CERN-LHC-Project-Report-639 (2003).

[103] **J. B. Jeanneret, I. A. Kourotchkine,** *private communication (2003).*

[104] **I. L. Azhgirey, I. A. Kourotchkine, V. V. Talanov,** *MARS program complex development for radiation aspects of electro-nucleoar devices design,* XV Workshop on Charged Particle Accelerators, Protvino, Vol. 2, p. 270 (1996).

[105] **V. V. Talanov,** *Universal Geometrical module for MARS Program,* Preprint IHEP 92-99, Protvino (1992).

[106] **I. Azhgirey, I. Baishev, N. Catalan Lasheras, J. B. Jeanneret,** *Cascade simulations for the betatron cleaning insertion,* CERN LHC Project Report 184 (1998).

[107] **I. L. Azhgirey, I. S. Baishev, M. Brugger, J. B. Jeanneret, I. A. Kourotchkine, G. R. Stevenson,** *Towards a shielding design for the momentum cleaning insertion of the LHC,* CERN, LHC Project Note 297 (2002).

[108] **M. Giesch,** *Twin aperture quadrupoles for the LHC cleaning insertions,* CERN AT/95-03, CERN LHC Note 323 (1995).

[109] **G. DeRijk,** *Magnetic Field Quality For MQW Cleaning Insertion Quadrupole With Unequal Excitation in the Two Apertures,* CERN LHC Project Note 100 (1997).

[110] **I. L. Azhgirey, I. S. Baishev,** *Radiation Studies of the LHC betatron scraping region at point 7,* CERN TIS-RP/99-01 (1999).

[111] **N. Catalan, Lasheras *et al.*,** *Proton Collimation in TeV Colliders,* LHC Project Report 156 (1997).

[112] **T. Trenkler, J. B. Jeanneret,** *K2: A software package evaluating collimation systems in circular colliders (Mannual),* Internal Report SL/Note 94-105 (AP) (1994).

[113] **G. R. Stevenson, A. Fassò, J. M. Zazula,** *The estimation of parameters of radiological interest for the scraper system of the LHC,* CERN/TIS-RP/IR/9-25 (1992).

[114] **I. A. Kourotchkine,** *private communication* (2002).

Bibliography

[115] **I. A. Kourotchkine,** *The calculation of the effective dose to the public due to the air releases from the LHC facilities,* CERN TIS/RP/TN/02/001 (2002).

[116] **R. Aßmann *et al.*,** *Minutes of the Beam Cleaning Study Group,* (2003).

[117] **O. Aberle,** *private communication (2003).*

[118] **C. Rathjen,** *Beam vacuum system in the long straight sections,* in proceedings of LHC Days 2003, 2-4 June 2003, p. 77 (2003).

[119] **I. L. Azhgirey, I. S. Baishev, M. Brugger, J. B. Jeanneret, I. A. Kourotchkine, G. R. Stevenson, P. Vojtyla,** *Radiological studies of the LHC momentum cleaning insertion, Part 1: Radioactivity in cooling water and in the molasse surrounding the tunnel,* CERN TIS–RP/TN/2002–024 (2002).

[120] **A. Morsch,** *ALIFE: A geometry editor and parser for FLUKA,* (1997).

[121] **C. Rathjen,** *private communication* (2003).

[122] **G. R. Stevenson,** *Induced activity in accelerator structures, air and water,* Rad. Prot. Dosim. 96, p. 373 (2001).

Acknowledgements

First of all I would like to take the opportunity to thank all the people who crossed my life at CERN during the last years, made it so much possible for me to enjoy my spell in the Geneva area and influenced my thesis work the one way or the other. Things I have learned not only in physics but for life in general exceed by far the contents of this thesis and will be preserved in my memories and keep me smiling. It was a wonderful time and I am thankful to everyone of you, too numerous to be all listed separately.

Especially I would like to thank Graham Roger Stevenson for his constant support and for giving me the chance to learn so many new things during the work on my thesis. In addition I am thankful to Prof. Ewald Schachinger who first made it possible to work on my thesis at CERN and then was always helpful and supportive in many ways. Notably his criticism helped me a lot, at least to try, to become more critical with my work but also more confident in my ideas.

A lot of my work would not have been possible without the intensive help of so many people in the radioprotection group, who I am all grateful to, whose support has always encouraged me and whose discussions created so much curiosity. In addition, especially during the start of my thesis I have very much enjoyed the vivid collaboration with the NA60 experiment, followed later on by the collimation working group.

As life would not be complete without exceptional friends, so would not have been my life during the thesis without the company of my best friends: Luisa, Silvia, Chris and Stefan. You share so many experiences it is hard to say how much you mean to me. Without your help and your encouragement this thesis would never have been written and maybe nobody knows better than Stefan whom I am very glad and proud to call a friend.

When winds changed, and my life became dark and difficult all of you helped me in one way or the other. However, certain things cannot be cured at once, they need time to pass by and occasionally somebody special, to enlighten thoughts believed to be lost and to create again curiosity about everything. This experience means very much to me and I am fortunate to say ’moi ca va bien’.

Finally, since it is always hard to finish the last sentence of a work like this I have kept it for those people of my life who have always been with me and who have supported me through all my steps so far, my parents. There was no part in my life where I did not learn from them or I could not rely on their help, hence as a symbol of the last step in my "official" education I would like to dedicate this thesis to you my parents. I will never stop learning from you and will always keep you enclosed in my heart.

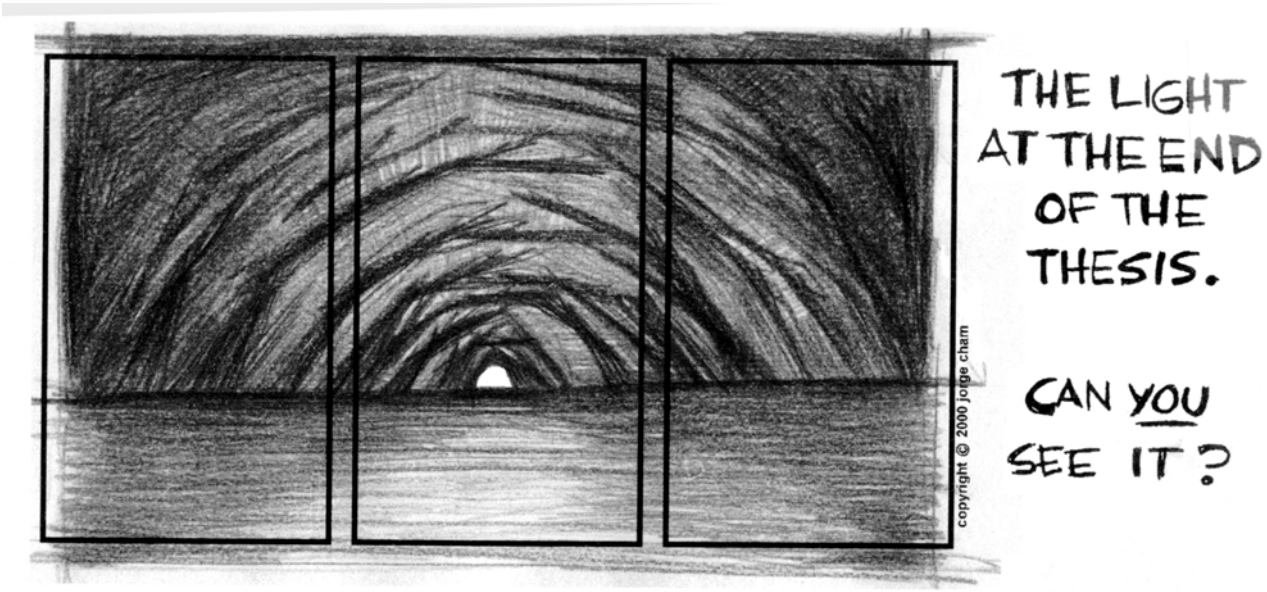
THE LIGHT AT THE END OF THE THESIS.
CAN YOU SEE IT?
copyright © 2000 jorge cham